The Production of ^{139}Pr and ^{139}Ce in Proton-induced Reactions

Christiaan Vermeulen

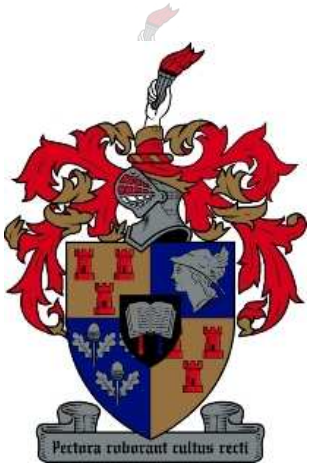

Thesis presented in partial fulfilment of the requirements for the degree of Master of Science at Stellenbosch University.

Supervisor: Dr. G.F. Steyn

Co-Supervisors: Dr. T.N. van der Walt, Prof. H.G. Raubenheimer

December 2007

Contents

List of Figures

List of Tables

Abstract

Excitation functions and production rates are presented for various Ce and Pr radionuclides formed in the bombardment of ^{141}Pr, ^{nat}La and ^{nat}Ce with protons. Extensive measurements were performed for ^{141}Pr + p up to 100 MeV and for ^{nat}La + p up to 20 MeV. The possibility is investigated to utilize tandem targetry for the production of no-carrier-added ^{139}Ce of high radionuclidic purity, having a Pr target in the higher energy slot followed by a La target in a lower energy slot. ^{141}Pr(p,3n)^{139m}Nd$\rightarrow$^{139}Pr is investigated as an alternative to the direct production route ^{140}Ce(p,2n)^{139}Pr for producing no-carrier-added ^{139}Pr of high radionuclidic purity. The advantages and disadvantages of both production routes are discussed. The simultaneous production of ^{139}Pr and ^{140}Nd using Pr as target is also investigated. Experimental thick-target production rates are presented for Pr radionuclides formed in the bombardment of ^{nat}Ce with protons at incident energies of 20, 26 and 32 MeV. All the experimental excitation functions obtained in this work are compared with theoretical predictions by means of the geometry-dependent hybrid (GDH) model as implemented in the code ALICE-IPPE. The results of this work are also compared with previous literature experimental data, if available.

Chapter 1

Introduction

1.1 General

Radionuclides can be produced by various routes, with the most common of these being the bombardment of a starting material, or target, by either neutrons or protons. Neutron bombardments are usually performed in the intense neutron flux inside the core of a nuclear reactor, utilizing the neutrons set free during the nuclear chain reactions that drive the reactor. Proton bombardments are usually performed by accelerating protons in either a linear accelerator or a cyclotron and directing the beam of protons onto a suitable target.

The great advantage of accelerator produced radionuclides is the fact that the primary radionuclide of interest is usually a different element from that of the target, thus allowing for its chemical separation from the target material. This separation leads to a product of very high specific activity.

iThemba LABS operates a separated sector cyclotron (SSC) that supports medical radiation for the treatment of cancer, experimental nuclear physics and radionuclide production programmes. The Radionuclide Production Group produces radiopharmaceuticals for the South African nuclear medicine community (*e.g.* ^{18}F, ^{67}Ga, ^{81}Rb and ^{123}I) as well as some medical radionuclides that are exported to the USA and Europe (*e.g.* ^{82}Sr/^{82m}Rb). In addition, the group also produces some radionuclides that are used in industry and physics applications, most notably ^{22}Na which is used in the manufacturing of positron emission sources for use in positron beam facilities.

The separated sector cyclotron of iThemba LABS delivers a 66 MeV proton beam for the routine production of radionuclides. The energy of 66 MeV is in fact dictated by the neutron therapy programme at iThemba LABS as well as an operational requirement to keep the number of energy changes to a minimum (as an energy change typically takes about 5 hours to complete and sometimes even longer.) The system allows for the rapid switching

of the beam (typically in less than 1 minute) between the neutron therapy vault and the radionuclide production vaults, in between patient treatments, taking advantage of the idle treatment time when the patient is being set up. This leads to very efficient use of the available beam time.

During the last decade the use of radiopharmaceuticals for diagnostic imaging has grown quite considerably, with the two major applications using radionuclides being PET (Positron Emission Tomography) and SPET (Single Photon Emission Tomography). Both these modalities are very important in nuclear medicine and even though PET has seen the largest growth recently, a significant number of diagnostic procedures can still only be performed by means of SPET, because of the availability of ^{99m}Tc form the ^{99}Mo/^{99m}Tc generator.

The recent revival of interest in radionuclide therapy and specifically in targeted radiotherapy, is a consequence of advances in the production of tissue specific biomolecules *e.g.* monoclonal antibodies, bone seeking biophosphanates and peptides [1]. Labeling these molecules with a specific radionuclide allows for delivery of that isotope and its diagnostic or therapeutic action straight to the affected area within the body of a patient. In conjunction with this effort, two kinds of investigation deserves special mention: Firstly, the use of so-called diagnostic/therapeutic pairs of radionuclides (*e.g.* ^{68}Ga/^{67}Ga, ^{123}/^{131}I, etc.) where the combination of diagnostic and therapeutic regimens in a single product aims to accurately monitor the uptake of the therapeutic agent in the treatment volume or tumour [2, 3]. The second is a continuing search for new PET radiotracers [4]. Currently, the work-horse of PET is ^{18}F[FDG] (^{18}F labeled 2-fluoro-2-deoxy-D-glucose) and this may continue for quite some time. However, there are many available positron emitters close to the line of stability which can be produced with a small accelerator, covering a large range of half-lives. In conjunction with continuing improvement in PET instrumentation, the development and scope of new PET radiotracers is huge and revolutionary.

This thesis is primarily concerned with the production of two radionuclides in the mass $A = 139$ region, namely ^{139}Pr and ^{139}Ce. Radionuclidically pure ^{139}Pr has potential as a PET radiotracer and ^{139}Ce has potential as a calibration source for SPET. The investigation into the production of these two radionuclides was prompted by requests from clients (or potential clients) as well as by a concurrently expressed interest from researchers at other laboratories with whom researchers from iThemba LABS collaborate. While most of the experimental investigations were performed at iThemba LABS, some of the experimental bombardments were done at the cyclotron facility of the Institute of Nuclear Chemistry (INC) at the Forschungszentrum Jülich GmbH, Jülich, Germany. Although the two radionuclides ^{139}Pr and ^{139}Ce constituted the main interest of this work, some information

on other co-produced radionuclides has also been extracted and is presented where appropriate (*e.g.* when those radionuclides may be important radiocontaminants).

The first objective of this study was to obtain the relevant nuclear data (*i.e.* excitation functions and integral yields of the radionuclides of interest) and to measure these when not available or if the available data proved to be inadequate or incomplete. The second objective was to utilize the nuclear data to optimize the production yields, which often entails finding a compromise between two conflicting requirements: (1) minimizing the level of radionuclidic contamination, and (2) maximizing the production rate. The third objective was to find appropriate radiochemical methods to separate the radionuclides of interest from the relevant target matrices as well as from each other.

1.2 The Radionuclide ^{139}Pr

The main interest in ^{139}Pr ($T_{1/2}$ = 4.41 h) stems from the fact that the lanthanides can be readily bound to conjugate biomolecules of human serum albumin (HSA) [5, 6]. In addition to this, ^{139}Pr is a positron emitter and thus a potential PET diagnostic agent.

Several recent studies also demonstrated the usefulness of therapeutic/diagnostic pairs of radionuclides. Rösch *et al.* [7], for example, discussed how the pair ^{140}Nd/^{140}Pr can be used to combine internal radiotherapy and PET, since the longer-lived parent ^{140}Nd ($T_{1/2}$ = 3.37 d) is a pure Auger electron emitter while the short-lived daughter ^{140}Pr ($T_{1/2}$ = 3.4 min) is a positron emitter. At almost the same time, Zeisler *et al.* [6] reported a strong accumulation of HSA-DTPA labeled with the ^{140}Nd/^{140}Pr *in vivo* generator in Morris hepatomas in rats. Using PET, the protein metabolism of the tumors could be followed for several days.

The relatively long half-life of ^{139}Pr (4.41 h, *i.e.* more than twice that of ^{18}F) makes it a suitable candidate to study metabolic processes with an uptake time of several hours, even though β^+ emission occurs only in $\sim$ 8% of decays. It may also be useful as the diagnostic partner of the therapeutic radionuclide ^{142g}Pr.

Two routes seem particularly feasible for the production of no-carrier-added ^{139}Pr with protons in the energy region below 100 MeV, namely via the nuclear reactions ^{140}Ce(p,2n)^{139}Pr and ^{141}Pr(p,3n)^{139m}Nd$\rightarrow$^{139}Pr. At a first glance, it may seem that the direct production via the (p,2n) reaction should be far superior and also simpler. Cerium, however, has four stable isotopes: ^{142}Ce (11.08%), ^{140}Ce (88.48%), ^{138}Ce (0.25%) and ^{136}Ce (0.19%), as shown in the relevant section of the chart of the nuclides reproduced in Fig. 1.1. The co-produced contaminant ^{142}Pr ($T_{1/2}$ = 19.13 h) formed via the (p,n) reaction on ^{142}Ce has to be taken into consideration when using natural Ce as target material. Praseodymium, in

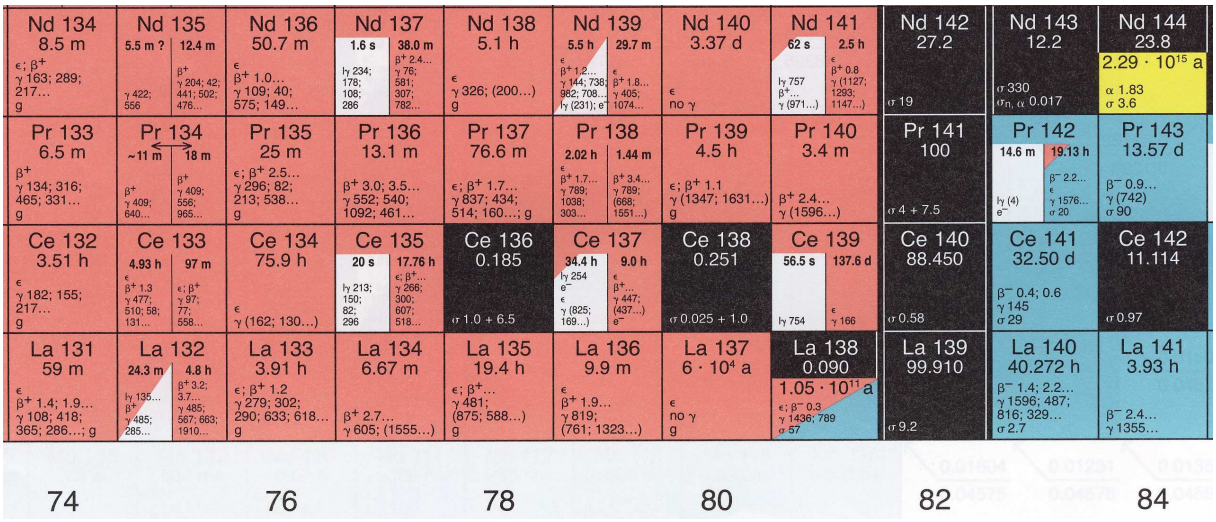

Figure 1.1: Relevant part of the "Karlsruher nuklidkarte" of 2006. Note that some of the nuclear data used in this work may differ slightly from the older information given in this chart of the nuclides. The reader is advised to consult this important figure regularly when reading the remainder of this thesis.

contrast, only has one stable isotope namely ^{141}Pr (100%), with no reaction path leading to ^{142}Pr. Another potentially serious radio-contaminant which may adversely affect the radionuclidic purity is ^{138m}Pr ($T_{1/2}$ = 2.12 h). It is produced via the (p,3n) reaction on ^{140}Ce. Significantly, no ^{138m}Pr is formed in the ^{141}Pr + p indirect production route as the decay of both ^{138m}Nd and ^{138g}Nd only populates the ground state, ^{138g}Pr ($T_{1/2}$ = 1.45 min), which rapidly decays away.

Metallic Ce is also one of the most reactive of the rare-earth elements (considerably more so than Pr) and is likely to ignite when only scratched [8], which makes its machining difficult and dangerous. For targetry purposes, therefore, a compound containing Ce such as CeO_2 may be preferable. In contrast, metallic Pr reacts only very slowly with oxygen if it is exposed to the atmosphere. Furthermore, Pr target disks can easily be manufactured by means of powder compaction in a hydraulic press. Previous experience at iThemba LABS has shown that properly cooled, aluminium-encapsulated Pr disks make excellent targets, quite capable of withstanding extensive bombardment with high-intensity proton beams.

In order to determine which route is the most suitable for routine ^{139}Pr production, one needs to calculate the yields of all the relevant Pr radionuclides (*i.e.* for both the desired radioisotope as well as the undesired contaminants), taking into account the bombardment, processing and waiting times as well as the decay and growth (via precursor decay) where applicable. For this purpose, accurate excitation function data are required. The properties of the available target materials and the ability to perform a separation of these materials and the produced radionuclides should also be a strong consideration.

For the purpose of yield calculations for ^{140}Ce + p, the existing excitation function data published by Zeisler and Becker [9] were found to be sufficient. A few thick-target yields were measured as part of the present study, however, in order to compare with the calculated values as a consistency check. In the case of ^{141}Pr + p, very limited data existed in the literature at the beginning of this project and the available data sets also revealed some discrepancies. A recent study by Hilgers *et al.* [10] has provided more extensive data on the formation of ^{139}Nd, ^{140}Nd and ^{141}Nd up to 45 MeV. For the purposes of the present study, however, reliable data for these radionuclides were also required above 45 MeV as well as data for several of the other radiolanthanides for which excitation functions could not be found in the literature. Extensive excitation function measurements were therefore performed for ^{141}Pr + p from threshold up to 100 MeV, utilizing the stacked-foil activation technique.

One aspect which we wanted to investigate in particular was whether it would be possible, at least in principle, to produce practical quantities of both ^{140}Nd and ^{139}Pr simultaneously during the same production run. In order to produce ^{139}Pr via the decay of ^{139m}Nd, a first chemical separation of the produced Nd from the Pr target material would have to be performed immediately after the end of bombardment (EOB). A second separation to isolate the ^{139}Pr daughter product from the Nd should then be performed later, after an optimum waiting period (or growing-in period for ^{139}Pr from the decay of its Nd precursors). Thus the possibility to extract two useful radioisotope products from the same irradiated target could perhaps be exploited.

Because of the difficulty of separating the lanthanides [77], it might well have been impossible to separate these two radionuclides completely from each other without significant losses. Recent work on novel separation techniques [81], however, precipitated an attempt in this work to achieve an efficient separation of Nd and Pr.

Theoretical calculations based on the geometry-dependent hybrid (GDH) model, performed using the ALICE-IPPE code (c.f. Dityuk *et al.* [13], and references therein) were also compared with the experimental excitation functions. These calculations were essential in the case of ^{140}Nd for purposes of yield estimation as the existing experimental data of good quality only extended up to 45 MeV for this radionuclide [5, 6, 10]. (Note that in the present experimental investigation, no new data for ^{140}Nd were obtained as it is not a γ-emitter.) We initially also used an ALICE-IPPE prediction to estimate the contaminant ^{142}Pr in ^{nat}Ce + p as no relevant measured excitation function data could be found. It was later decided important to validate these calculations by measuring the thick-target production rate at a few selected energies.

In this thesis, a detailed account of our experimental work on the nuclear data relevant

for the production of ^{139}Pr via the ^{141}Pr(p,3n)^{139m}Nd$\rightarrow^{139}$Pr reaction is presented. This includes excitation functions for all the observed Nd and Pr radionuclides up to 100 MeV, several of which constitute potential radiocontaminants. A comparison is also made with the alternative production route which employs the ^{140}Ce(p,2n)^{139}Pr reaction, including new thick-target production rate measurements at incident energies of 20, 26 and 32 MeV. The optimum production energy windows are deduced from the nuclear data, the main concern being not to compromise on the radionuclidic purity of the final product.

Preliminary results of this work have been presented at the International Conference on Nuclear Data for Science and Technology [14] held in Santa Fe, New Mexico, in September 2004. The final results have been presented in a paper on the production of ^{139}Pr via precursor decay in the bombardment of ^{nat}Pr with protons, which has recently appeared in Nuclear Instruments and Methods in Physics Research B [15].

1.3 The Radionuclide ^{139}Ce

The relatively long-lived radionuclide ^{139}Ce ($T_{1/2}$ = 137.6 d) is useful as a standard for the calibration of γ-ray detectors. In recent years, the Radionuclide Production Group of iThemba LABS has received several requests for both ^{139}Ce point and line sources. This radioisotope has only one strong γ-line at 165.857 keV, which is within the optimum energy range for detection with a gamma camera. Image degradation during single photon emission tomography (SPET) due to attenuation and Compton scattering of photons can cause clinical image artifacts. Du Raan *et al.* [16] have shown that a ^{139}Ce line source can be used to determine attenuation maps for SPET. The 165.857 keV γ-line has sufficiently higher energy than that of ^{99m}Tc (140.51 keV) to allow for simultaneous transmission-emission imaging using a fixed dual-detector camera, thereby eliminating the necessity of correction of the scatter component from the emission image. This method also overcomes the problem of the primary photopeaks overlapping as is the case when ^{123m}Te or ^{99m}Tc line sources are used with ^{99m}Tc as the imaging agent.

Two routes are feasible for the production of no-carrier-added ^{139}Ce with protons in the energy region below 100 MeV, namely via the nuclear reactions ^{141}Pr(p,x)^{139}Ce and ^{139}La(p,n)^{139}Ce. Conveniently, ^{141}Pr and ^{139}La have natural abundances of 100% and 99.91%, respectively, thus natural targets are suitable. Compared to the long half-life of ^{139}Ce, all its pre-cursors (^{139m}Nd, ^{139g}Nd and ^{139}Pr) are short-lived and their decay lead to the bulk of the ^{139}Ce yield in the case of ^{141}Pr + p. The cross sections presented in this study for the Ce radionuclides are therefore for their cumulative formation in the case of ^{141}Pr + p but for their direct formation in the case of ^{nat}La + p.

A detailed account of new experimental work on the relevant nuclear data for the production of ^{139}Ce in the proton bombardment of natural Pr and La is presented in this thesis. In addition, excitation functions are presented for all the other observed Ce radionuclides. New data have been measured up to 100 MeV for ^{141}Pr + p and up to 20 MeV for ^{nat}La + p. The feasibility of a Pr/La tandem target for optimizing the ^{139}Ce production yield has also been investigated. As before, the measured excitation functions are compared with theoretical predictions by means of the ALICE-IPPE code.

Preliminary results of this study have also been presented at the International Conference on Nuclear Data for Science and Technology [14] held in Santa Fe, New Mexico, in September 2004. The final results have been presented in a paper on the production of ^{139}Ce by means of proton-induced reactions, which has been published in Nuclear Instruments and Methods in Physics Research B [17].

A detailed method was developed at iThemba LABS for the separation of ^{139}Ce from Pr target material. This work was presented at the 4th Conference and Workshop on Cyclotrons and Applications [18] held in Cairo, Egypt in February 2001. One aim of the present study was to simplify that method as well as to determine the percentage recovery from a bombarded Pr/La tandem target. As such, the method was extended to include the separation of ^{139}Ce from a La target.

1.4 Thesis Outline

1.4.1 Chapter 2 – Nuclear Data: Experimental Methods

This chapter is dedicated to the experimental methods used for the nuclear data measurements. These methods include the activation of Pr, La and Ce targets and explains the experimental setup for each of the investigated materials as well as the irradiation parameters used for each experiment. The chapter also deals with the radionuclide assay methods and the analysis performed on the data that was generated in each experiment.

1.4.2 Chapter 3 – Nuclear Data: Theoretical Calculations

Chapter 3 contains an overview of the ALICE-IPPE code and the calculations performed to arrive at the theoretical excitation function curves presented with the measured data. A brief discussion is included on the Geometry Dependant Hybrid (GDH) model and certain aspects of the calculations.

1.4.3 Chapter 4 – Nuclear Data: Results and Discussion

In this chapter, the results of the different nuclear data measurements are presented in the form of excitation functions as well as the thick target yields for the different radionuclides that were investigated. Optimum production energy windows are deduced.

1.4.4 Chapter 5 – Nuclear Data: Conclusions

The conclusions of the nuclear data investigation are presented, including a final discussion on the viability for the production of the two main radionuclides of interest, namely ^{139}Pr and ^{139}Ce.

1.4.5 Chapter 6 – Chemistry and Separation: Overview

Chapter 6 consists of a description of the chemistry of the main elements of interest in this study. The chapter also contains a description of the fundamentals of ion-exchange and high performance liquid chromatography, as well as descriptions of the separation media and analytical techniques used during the course of experimentation.

1.4.6 Chapter 7 – Separation: Methods and Results

Chapter 7 deals with the methods of chemical separation of the radionuclides of interest from the target material as well as the radionuclidic impurities formed during the bombardment process. Existing methods are evaluated and improved where possible and the results are presented for the separation methods that were investigated.

1.4.7 Chapter 8 – Comments in Conclusion

The final chapter concludes the thesis with a discussion of the viability of the investigated processes for routine commercial productions. A short discussion on possible future investigations is also given.

Chapter 2

Nuclear Data: Experimental Methods

2.1 Activation of Pr Targets

2.1.1 Experimental Set-up and Irradiations

The activation method is the most commonly used way to determine excitation functions of radionuclides produced in charged-particle induced reactions. This method usually involves the irradiation of thin samples (or foils) of a target material. After irradiation, a quantitative assay of the radionuclides formed in each sample is performed. The method of activation can be employed in several ways. The first involves the individual irradiation of samples with beams of different energies. Obviously, to achieve this the accelerator has to be tuned to a different energy for each irradiation. At several linear accelerators around the world, energy changes can be done rapidly and this method is therefore appropriate. Since an energy change on the separated sector cyclotron of iThemba LABS takes about five hours, irradiations at a large number of different energies becomes quite impractical.

The second method of activation is called the stacked-foil technique. With this technique a number of samples, usually foils, are irradiated as a stack and counted individually afterwards. The strength of this method lies in the fact that the charged-particle beam loses energy progressively as it traverses through the stack so that a different energy is applicable to each foil, albeit at the cost of an increasing energy uncertainty with increasing depth of penetration. Since cross-section data at various energies can be obtained from a single irradiation, the demand for experimental beam time on the accelerator can be reduced considerably.

As already mentioned, the stacked-foil technique does have drawbacks. Uncertainties in the monitor cross sections (to be discussed later), energy straggling in the stack as well

as uncertainties in foil thickness and stopping powers of the irradiated materials, give rise to both an energy spread and increasing uncertainty in the energy of particles moving through a specific part of the stack. Great care must therefore be taken to minimize errors, especially in the beam energy determination and in the composition of the stack. The additional energy uncertainty can be limited, though, by keeping the stacks relatively short and employing a few primary beam energies to cover the energy region of interest.

In this specific activation study, the irradiations were performed at three primary energies to reduce these errors. Six composite foil stacks were irradiated, two at each primary proton-beam energy of 97.8±0.5, 65.5±0.4 and 39.6±0.3 MeV, delivered by the separated-sector cyclotron facility of iThemba LABS. The stacks consisted of high-purity Pr foils of 100 μm thickness (99.9%, Goodfellow, U.K.), high-purity Al monitor foils of 250 μm thickness (99.999%, Goodfellow, U.K.) and groups of 125 μm thick Cu degrader foils (99.9%, Goodfellow, U.K.) as required to obtain well spaced proton energies across the entire energy region of interest. All the foils had a diameter of 19 mm and their individual thicknesses were determined by weighing. The beam was focussed to a spot of typically 4 mm in diameter on a BeO_2 viewer prior to the experimental irradiations. All the irradiations were carried out in a simple stack holder mounted on the end of an external beamline (shown in Fig. 2.1) and in each case the beam was stopped in a thick Cu disk immediately behind the stack. The beam currents varied between 50 and 100 nA and the irradiation times between 1 and 1.5 h.

2.1.2 Radionuclide Assays

After bombardment, the activated foils were individually assayed by means of standard off-line γ-ray spectrometry in three consecutive counting sessions. An accurately calibrated HPGe detector (see Fig. 2.2) with a relative efficiency of 13% and a resolution of 1.8 keV at 1.33 MeV was used for this purpose. The photo-peak areas were determined by means of the quantitative software supplied with the Silena EMCAPLUS multi-channel analyser employed in this work.

2.1.3 Data Analysis

The cross sections of the observed activation products were calculated from their measured γ-ray emissions using disintegration data from the catalogue of Firestone and Eckström [19]. Some relevant nuclear data as well as the γ-lines used to identify the nuclides of interest are listed in Table 2.1. The relevant equations are summarized in Appendices A and B.

Corrections were made for decay losses during and after bombardment, as well as during counting. Although the accumulated charge was measured directly by means of a calibrated

Table 2.1: Investigated Nd, Pr and Ce radionuclides, their decay properties and γ-rays used for their identification and activity measurement[a]

Nuclide	Half-life	Decay mode	γ-rays (keV)	Intensity (%)
^{135g}Nd	12.4 m	$\epsilon + \beta^+$: 100%	204.02	52.0
^{136}Nd	50.65 m	$\epsilon + \beta^+$: 100%	108.9	32.0
^{137g}Nd	38.5 m	$\epsilon + \beta^+$: 100%	580.6	13.0
^{138}Nd	5.04 h	ϵ: 100%	325.76	2.93
^{139g}Nd	29.7 m	$\epsilon + \beta^+$: 100%	405.12	7.0
^{139m}Nd	5.50 h	$\epsilon + \beta^+$: 88.2%	113.94	40.0
		IT: 11.8%	737.96	35.0
^{140}Nd	3.37 d	ϵ: 100%	no γ-rays	
^{141g}Nd	2.49 h	$\epsilon + \beta^+$: 100%	1126.8	0.8
			1292.6	0.46
^{136}Pr	13.1 m	$\epsilon + \beta^+$: 100%	552.16	76
^{137}Pr	1.28 h	$\epsilon + \beta^+$: 100%	836.7	1.8
^{138m}Pr	2.12 h	$\epsilon + \beta^+$: 100%	788.74	100
^{132}Ce	3.51 h	$\epsilon + \beta^+$: 100%	182.11	77.0
^{133m}Ce	4.9 h	$\epsilon + \beta^+$: 100%	130.80	17.9
^{135}Ce	17.7 h	$\epsilon + \beta^+$: 100%	265.56	41.8
^{137m}Ce	34.4 h	$\epsilon + \beta^+$: 0.78%	254.29	11.0
		IT: 99.22%		
^{139}Ce	137.64 d	ϵ: 100%	165.86	80.0

[a]Taken from [19]

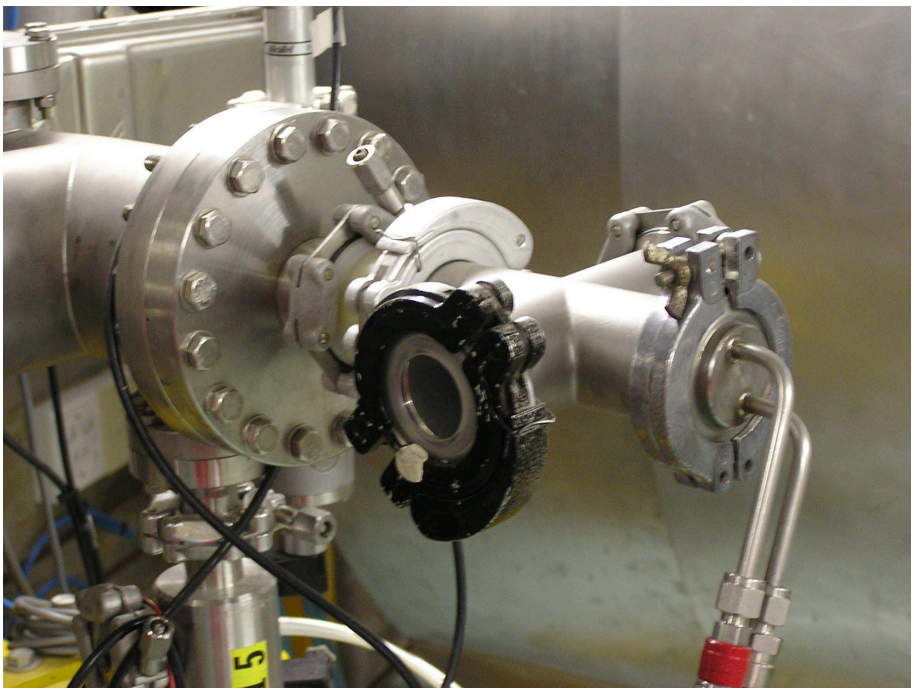

Figure 2.1: The target holder used to irradiate foil stacks at iThemba LABS, mounted on the end of an external beamline. The perspex window, on the left side of the holder (black flange connector), was for aligning the beam on a BeO_2 screen, viewed with a closed-circuit TV camera. Cooling water lines are visible on the front end of the target holder.

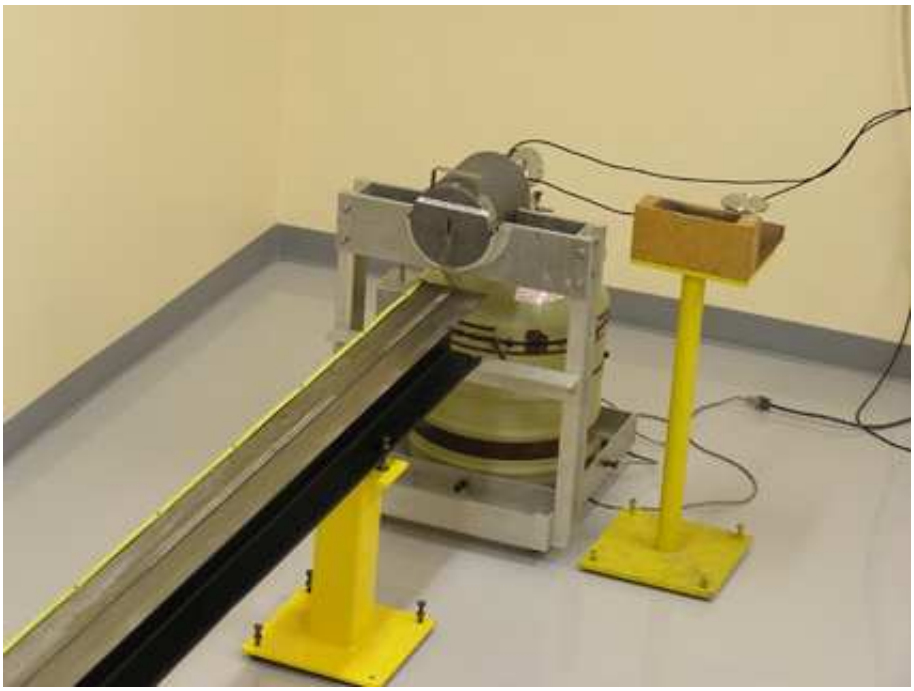

Figure 2.2: The HPGe detector counting facility used at iThemba LABS for the off-line measurement of γ-ray spectra of activated foils and/or other samples. The detector has a horizontal geometry and is surrounded by an inner Cu and outer Pb shield. A rail provides for variable source-detector distances in the range 6 cm to 4 m.

Brookhaven Instruments Corporation Model 1000C current integrator, the excitation function of ^{22}Na extracted from the Al monitor foils served as a consistency check. For this purpose, the standard ^{22}Na excitation function data recommended by the IAEA [20] was used. For all the stacks, the beam flux measured by direct integration did not differ by more than 5% with the values determined from the monitor foil sets. Corrections for beam current losses due to nonelastic nuclear interactions were made according to the prescription and tables of Janni [21]. The average proton energy in each foil was calculated based on the stopping power formulae of Anderson and Ziegler [22] as well as from a newer compilation [23], which gave similar values.

The total uncertainties in the measured cross sections were obtained by summing all the contributing uncertainties in quadrature and are expressed with a 1σ (68%) confidence level. A variable component includes the uncertainty due to counting statistics and photopeak integration as well as the uncertainty associated with the beam-loss corrections. The latter did not exceed 1.6%. The systematic uncertainty was estimated to be about 7%, including the uncertainty in beam current integration (3%), detector efficiency (5%), counting geometry (1%), decay corrections (2%) and foil thickness (3%). The uncertainty in energy of each measured data point was estimated from the uncertainty in incident beam energy, foil thickness and depth of penetration in the stack.

2.2 Activation of La Targets

2.2.1 Experimental Set-up and Irradiations

Usually, excitation functions are measured using the stacked-foil technique; the foils being sufficiently thin to ensure that the measured cross sections constitute microscopic data. From these microscopic data, production rates or yields are deduced by means of a *numerical integration procedure* [24]. This is indeed the method used in the ^{141}Pr + p case discussed in the previous section.

Occasionally, however, it is difficult to use the standard stacked-foil technique to measure excitation functions due to difficulties in preparing thin foils or thin disks of a given material. It is difficult, for example, to prepare and use metallic foils of La because of its high reactivity and rapid rate of oxidation on contact with air. Compounds can be used, such as La_2O_3, but this material is very brittle, precluding self-supporting thin foils. Although methods exist for preparing thin samples of such a substance on metallic backing foils, for example the well-known sedimentation method [25], we decided to investigate a different approach. Instead, thick-target yields of ^{139}Ce were measured in a range of different energy windows in order to establish a thick-target production rate curve. The corresponding ^{139}Ce excitation function was then extracted by means of a *differentiation procedure*, in order to obtain microscopic data and for comparison with other measured cross sections in the literature. An important criterion of this approach is that the spacing of the measured points on the energy axis should be similar to what would have been appropriate in a conventional stacked-foil experiment.

A schematic diagram of the experimental set-up used to measure the thick-target production rate curve for ^{nat}La + p is shown in Fig. 2.3. A brass target holder contained an aluminium degrader, a Ti monitor foil and a La_2O_3 target for each measurement. The targets were thick enough to stop the beam. Measurements were performed using degraders of various thicknesses to cover the energy region from threshold up to 20 MeV. The energy of the cyclotron beam was determined using a method of measuring the relative phase shift of successive beam bunches, developed by Z. Kormány [26].

The La_2O_3 disks were pressed from high-purity powder (99.98%, Fluka, Switzerland) and had a nominal thickness of 1.2 g/cm^2. The monitor foils were high purity Ti (99.99%, Goodfellow, U.K.) with a thickness of 59.8 mg/cm^2, for the accurate determination of the incident proton flux. Protons of nominally 20 MeV were extracted from the Cyclotron Corporation CV28 cyclotron of the Institute for Nuclear Chemistry (INC) at the Forschungszentrum Jülich GmbH. The target assembly was located outside the cyclotron and beamline vacuum (See Fig. 2.5); the proton beam first passed through a beamline exit

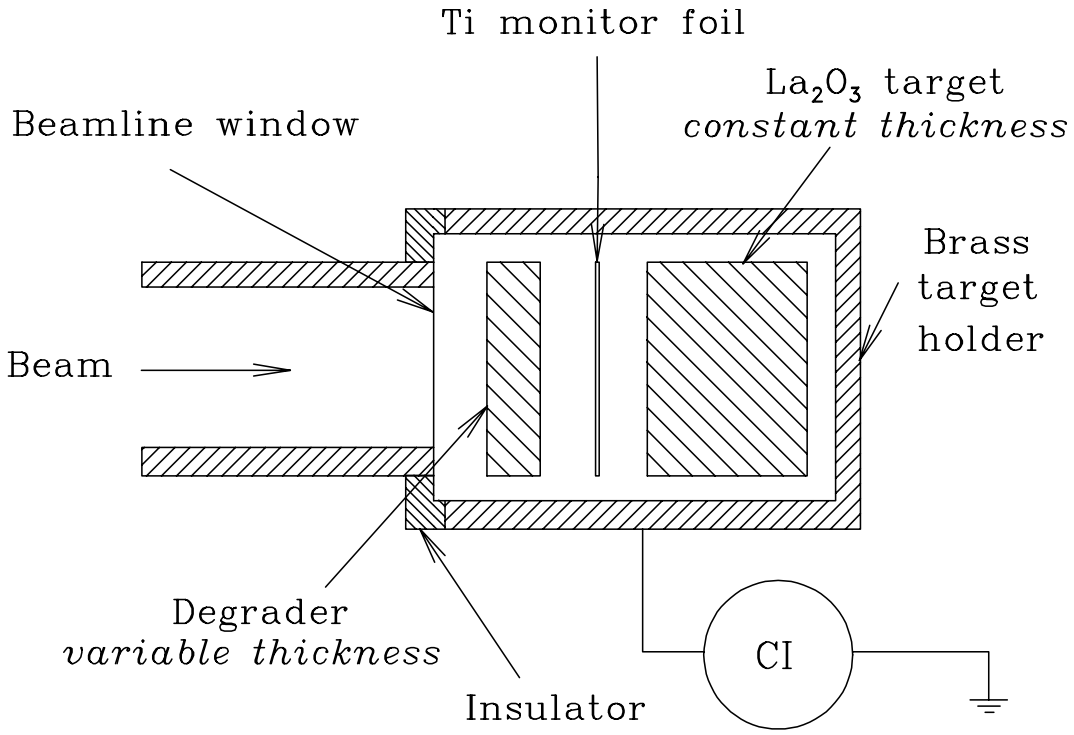

Figure 2.3: Experimental set-up used at the CV28 cyclotron facility of the Forschungszentrum Jülich to activate La_2O_3 targets and Ti monitor foils for purposes of measuring the ^{139}Ce thick-target production rate curve. Degraders of various thicknesses could be accommodated to adjust the energy, while the targets of constant thickness were thick enough to stop the beam. CI indicates current integrator.

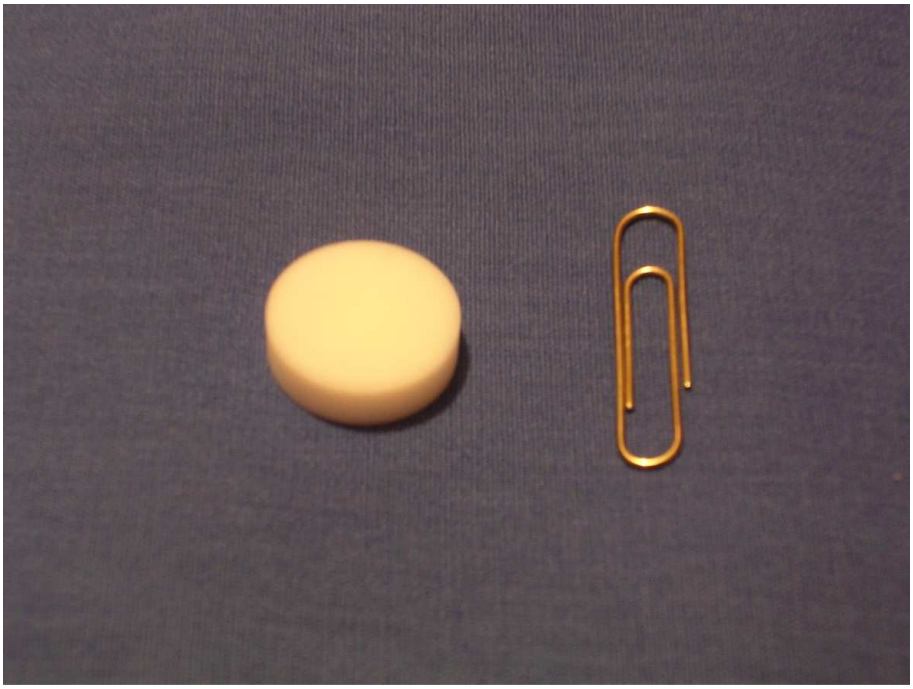

Figure 2.4: A compressed and sintered La_2O_3 target (with a paper clip for scale).

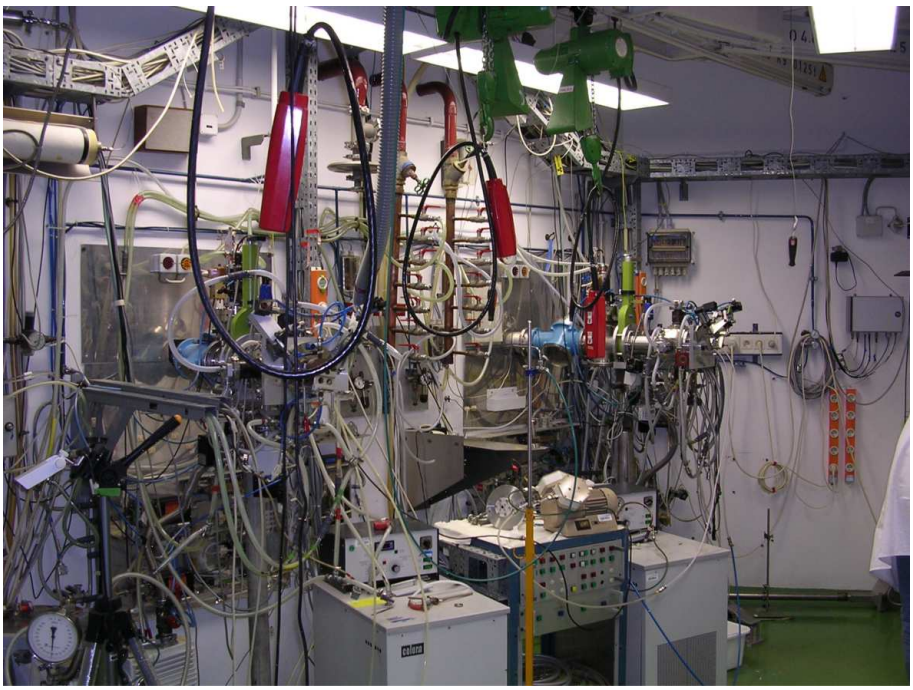

Figure 2.5: The bombardment vault of the CV28 cyclotron facility at the Forschungszentrum Jülich, showing two external beamlines. The experiment was performed on the beamline on the right.

window made from Havar, before reaching the experimental set-up. This made rapid target and degrader exchanges possible. Each bombardment lasted approximately 30 minutes at an average reported beam current of 50 nA. After bombardment, each La_2O_3 target was dissolved in 5 ml of a 1 M HCl solution in a standard Packard vial. Once filled and sealed, these vials constituted appropriate counting sources. The reason why liquid sources were prepared in this way instead of counting the activated La_2O_3 disks directly, was because they were considered to be too thick to constitute bona fide point sources. Also, the depth of penetration of the beam in these disks differed, depending on the degraded energy. The liquid sources ensured a consistent counting geometry as well as allowing calibration sources of the same geometry to be easily prepared.

2.2.2 Radionuclide Assays

After bombardment, the activated monitor foils and liquid sources in Packard vials were individually counted by means of standard off-line γ-ray spectrometry. The set-up used for this purpose at the Forschungszentrum Jülich employed an accurately calibrated HPGe detector with a vertical geometry and a relative efficiency of 20%. Photographs of the counting sources and detector set-up are shown in Figs. 2.6 and 2.7, respectively. Point sources traceable to the BIPM, Sèvres, France were used to calibrate the detector. Correction factors were determined experimentally to account for the difference in the source-detector geometry of the liquid sources. In order to achieve this, ^{139}Ce point and liquid

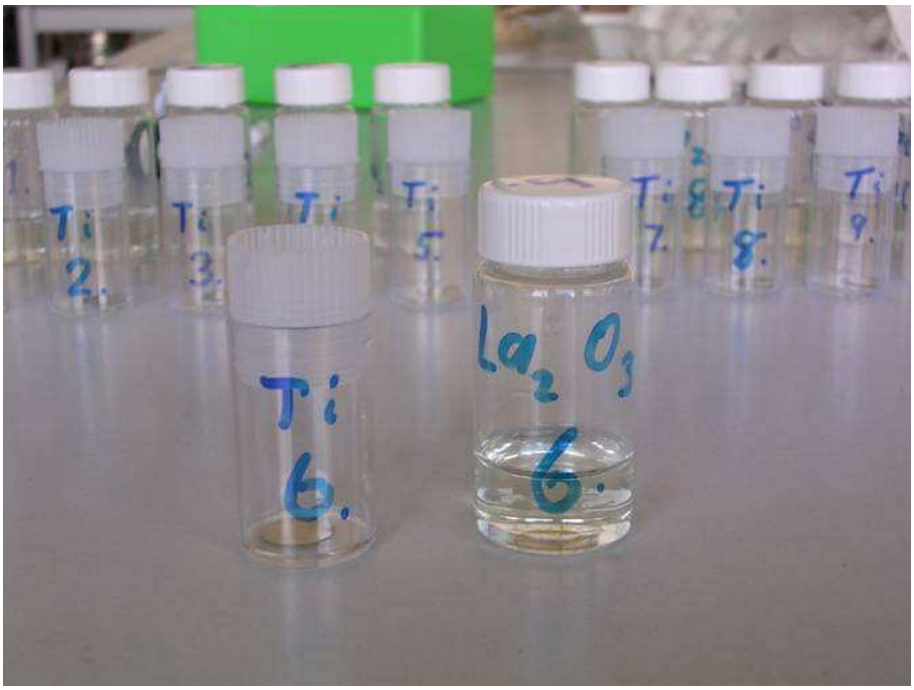

Figure 2.6: Counting sources prepared at the Forschungszentrum Jülich. The Ti monitor foils were placed in thin-walled polyethelene vials, while glass Packard vials served to contain the La_2O_3 solutions and the induced ^{139}Ce.

Figure 2.7: The HPGe counting facility used at the Forschungszentrum Jülich. Note the vertical geometry of the detector.

sources of identical strengths were specially prepared in order to obtain detector efficiency calibration curves for the liquid sources. By using sources of equal strength, the difference in detector response between the point-source and liquid-source counting geometries could be accurately quantified by direct comparison, without the need for these specially prepared sources to be calibrated sources.

2.2.3 Data Analysis

The first step of the data analysis was to determine the charge collected on target during each irradiation (*i.e.* the integrated beam current). The reason for this is that the values measured directly with the electronic current integrator (connected to the experimental assembly) could not be considered accurate. It is well known that charge can escape via secondary emissions (*e.g.* delta rays) as well as by conduction along cooling lines if the water is not very thoroughly de-ionized. The experimental assembly was not provided with charge escape suppression which is, for example, standard on any well-designed Faraday cup. Instead, the integrated current values were determined from the Ti monitor foils, using the ^{nat}Ti(p,x)^{48}V monitor reaction.

A standard procedure was followed, namely to initially adopt the values obtained from the electronic current integrator and to extract the ^{48}V monitor excitation function using these values. This measured excitation function was then compared with the reference excitation function (*i.e.* the recommended values). An IAEA recommended excitation function was used for this purpose [20]. By renormalizing the newly extracted excitation function to the reference excitation function, a correction factor could be extracted and applied throughout to correct the measured integrated current values. Note that only a *single factor* was determined from the combined monitor data set, not a different factor for each irradiation. This was done because the experimental conditions were the same for all the irradiations, therefore it was assumed that differences in charge collection from one experimental bombardment to the next would be unlikely.

When the measured monitor reaction cross-section values were plotted together with the recommended excitation function, however, an unexpected and rather depressing result was obtained. Shown in Fig. 2.8, it is clear that in addition to an expected vertical shift between the two excitation functions, there is also a horizontal shift, thus a discrepancy between the proton energies. Such a large energy shift was not expected as the measured beam energy was supposed to be quite accurate and the foil and target thicknesses were known to good accuracy. We expected to have to do only a vertical adjustment or renormalization. The monitor foils were not included to determine the beam energy but only the accumulated charge. The particular recommended excitation function used was also not under suspicion

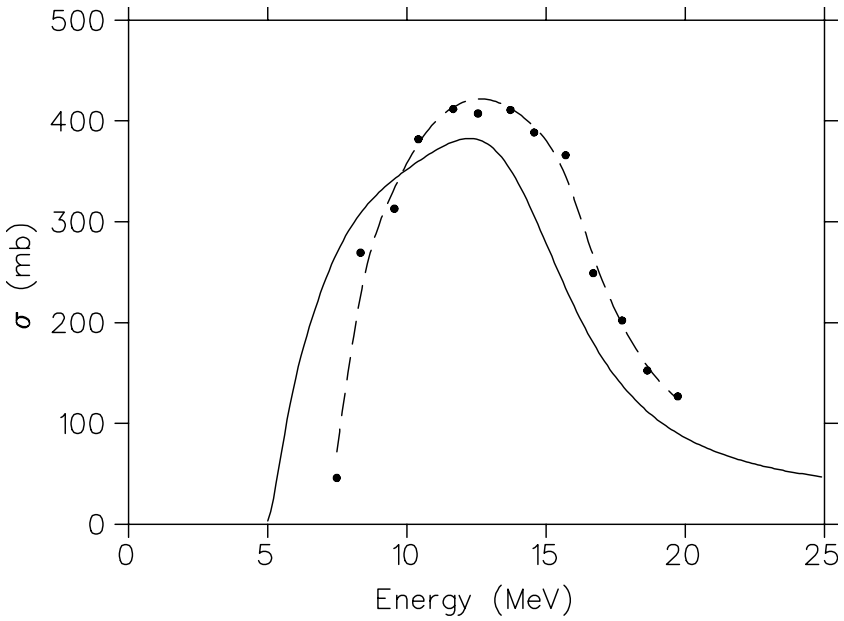

Figure 2.8: A plot of the recommended excitation function (Solid Line) and the cross-section values extracted from the monitor foil measurement.

as it had been used many times at iThemba LABS in the past, and has not shown such an energy shift before.

An opportunity to redo the experiment or to perform a few more measurements did not exist. In fact, this experiment was one of the very last ones on that beamline as the CV28 cyclotron was soon to be decommissioned. Thus, it was important for us to do the best analysis we could under the circumstances and to establish how serious the experimental problem really was. Thus, the analysis presented in the following paragraphs is more complicated than it normally would be.

First, we expected that the beam energy measurement provided by the CV28 cyclotron operators was not correct but we did not want to simply assume this. We somehow wanted to test this statement in a more scientific way. According to Dr. Kormány [27], a change in calibration of the apparatus or an incorrect spacing between the two capacitive probes, amongst other possibilities, could lead to such an error. This method measures a relative phase shift between successive beam bunches using two capacitive probes mounted on a section of the high-energy beamline. The apparatus was set up for the relative phase difference to disappear at a known beam energy, close to the maximum that the cyclotron could deliver. However, one of the probes was adjustable and could perhaps have been set at an incorrect position. This, however, is all speculation. We decided that it would be more useful to find out whether we had good reason to assume that the beam energy measurement was wrong and not what exactly caused it to be wrong.

A FORTRAN code was developed to enable us to adjust the value of the beam energy,

recalculate all the proton energies associated with the monitor foils, calculate the Chi-square [28] of the two cross-section sets (*i.e.* measured and recommended) as a function of incident energy and determine at which incident energy it reaches a minimum. In addition, we also calculated the Pearson product moment correlation coefficient [28] from the two cross-section sets. This parameter has a value between 0 and 1; the closer it is to 1 the better the fit. When shifting the measured monitor excitation function horizontally (*i.e.* on the energy axis; see Fig. 2.8) we searched for a minimum Chi-square value. In contrast, when shifting the measured monitor excitation function vertically (*i.e.* along the cross-section axis) in order to find the normalization factor (*i.e.* the correction factor for the integrated beam current), we searched for a minimum Sum-of-Squares value. The reason for the difference in treatment of the horizontal shift and vertical shift will be explained later. Furthermore, we used a form of the Chi-square called McNemar's Chi-square [29], rather than the normal Chi-square, which will also be explained later.

Thus, we searched for the values of two parameters, N and F, defined as follows:

$$E^{beam}_{actual} = E^{beam}_{measured} \times F, \tag{2.1}$$

and

$$Q^{beam}_{actual} = Q^{beam}_{measured} \times N^{-1}, \tag{2.2}$$

where E^{beam} denotes the beam energy and Q^{beam} denotes the integrated current or charge. In the following, we will refer to F as the *energy adjustment factor* and N as the *normalization factor*.

The specific form of the McNemar's Chi-square used in this work is given as follows:

$$\chi^2 \;=\; \sum_{i=1}^{n}\left[\frac{(O_i - E_i)^2}{0.5(O_i + E_i)}\right], \tag{2.3}$$

where O_i denotes the measured cross-section values and E_i the corresponding recommended cross-section values at the respective monitor foil energies. The value of n equals the total number of monitor foils unless some of the shifted energies reach values below the reaction threshold, in which case those values are excluded, resulting in n having a smaller value.

The Pearson product moment correlation coefficient is given by

$$r \;=\; \frac{(n\sum_{i=1}^{n} O_i E_i) - (\sum_{i=1}^{n} O_i \sum_{i=1}^{n} E_i)}{\sqrt{\left[n\sum_{i=1}^{n} O_i^2 - (\sum_{i=1}^{n} O_i)^2\right]\left[n\sum_{i=1}^{n} E_i^2 - (\sum_{i=1}^{n} E_i)^2\right]}}, \tag{2.4}$$

where the O_i, E_i and n have the same meaning as before. (Note that in the literature, the O_i are often called the *observed* values and the E_i the *expected* values).

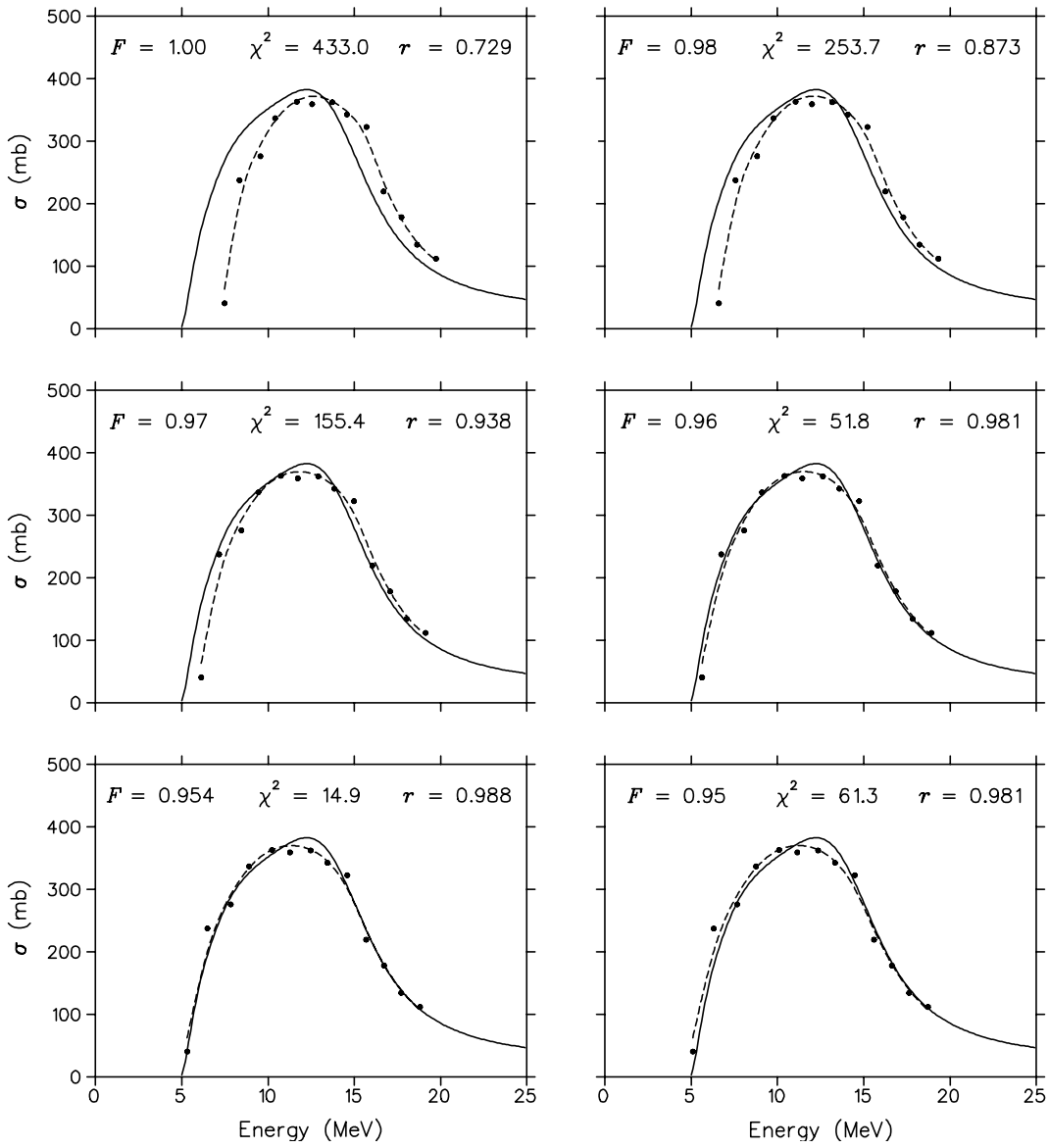

Figure 2.9: Recommended ^{48}V excitation function for Ti + p (solid curves) and the cross-section values extracted from the activated Ti monitor foils, for different energy adjustment factors. The dashed curves through the data points are to guide the eye.

Figure 2.9 shows the measured and recommended ^{48}V monitor excitation functions for various values of the energy adjustment factor, in decreasing order, after the Sum-of-Squares minimization has been performed. The values of χ^2 and r are indicated for each case. It is interesting to see how rapidly χ^2 decreases in value as F is decreased from a value of 1.0 to 0.95 (χ^2 = 433.0, 253.7, 155.4, 51.8, 14.9 and 61.3 at F = 1.0, 0.98, 0.97, 0.96, 0.954 and 0.95, respectively). Thus, χ^2 reaches a minimum at $F = 0.954$, whereafter it rapidly increases again as F is further decreased. Also note how r increases in value until it reaches its closest value to 1.0 at exactly the incident energy where χ^2 reaches a minimum. At this point, r has a value of 0.988, which indicates quite a good correlation. Visually, the shape of the measured excitation function improves progressively in terms of its goodness of fit to the recommended excitation function as F is reduced down to a value

of 0.954. Clearly, as F is further reduced to a value of $F = 0.95$, the incident energy has been reduced too much; the shape of the the measured excitation function is not as good as at $F = 0.954$ (especially near the reaction threshold), χ^2 is significantly higher and r moves away from its closest value to 1.0.

Another useful way to present these results is to plot the residual values versus the proton energy. The residual values, converted to a percentage of the recommended values (*i.e.* $100 \times (O_i - E_i)/E_i$), are shown in Fig. 2.10 for the various values of the energy adjustment factors used in Fig. 2.9.

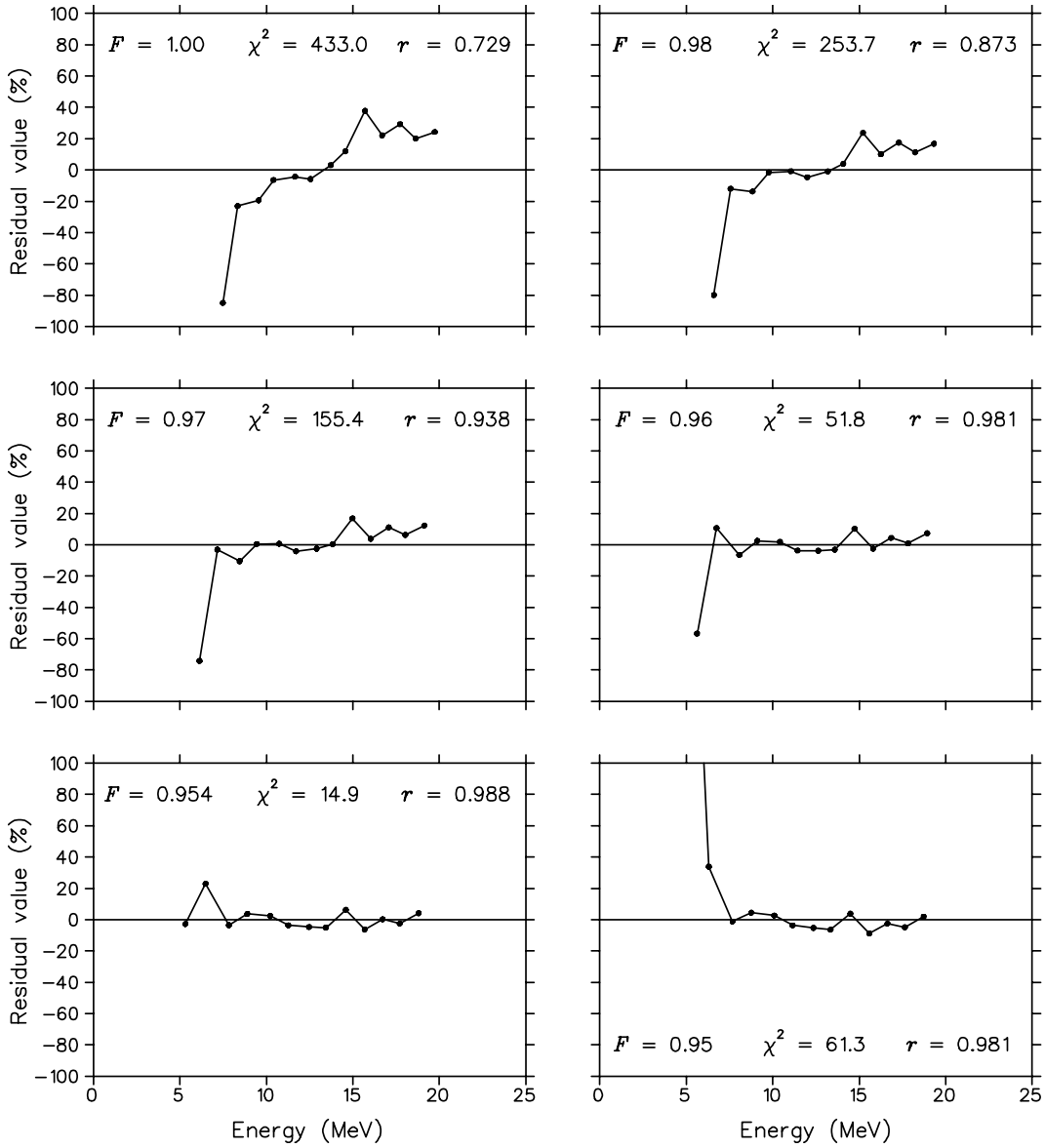

Figure 2.10: Residual values obtained from the fits of the measured ^{48}V excitation function to the recommended values, for those cases presented in Fig. 2.9.

If the correlation between the two cross-section sets would have been perfect (*i.e.* for the hypothetical case where $r = 1$ and $\chi^2 = 0$) then all residual values would have been

zero. Thus, for perfect correlation, the curve of residuals would have been a horizontal line along the $y = 0$ baseline. In practice, small deviations both above and below the $y = 0$ baseline with no particular trend, is an indication of a good correlation. Trends showing any significant deviation from that, for example an overall positive or negative slope or the presence of far outlying points, give an indication of a less than good or poor correlation. As F decreases from a value of 1.0 down to 0.95, the residuals curve changes from an overall positive slope to a negative one, with the most favourable distribution around the baseline when $F = 0.954$.

It is important to realize that any recalculation of the monitor foil energies at values of F different from 1.0, changes the shape of the measured excitation function. This is because the proton stopping power is very non-linear, increasing with penetration depth into the target or stack. As shown in Fig. 2.9, it does appear that the shape improves (*i.e.* gets more similar to the recommended excitation function) as the incident energy is reduced, up to a value of $F = 0.954$. This can be interpreted as positive evidence that the discrepancy shown in Fig. 2.8 is the result of an initially incorrect incident beam energy determination.

In order to illustrate this more convincingly, the same analysis shown in Fig. 2.9 was repeated while keeping the original shape of the measured excitation function fixed (*i.e.* at its $F = 1.0$ shape), thus shifting the excitation function horizontally along the energy axis by subtracting a constant amount from all the energies associated with the monitor foils. The results are shown in Fig. 2.11.

Comparing Figs. 2.11 and 2.9, it is clear that the same goodness of fit cannot be obtained if the original shape of the measured excitation function is adopted throughout. This is supported by the minimum value found for χ^2 and the corresponding value of r. A best fit is found with a rather large value of the energy adjustment factor, $F = 0.904$. At this energy, $\chi^2 = 89.9$ and $r = 0.951$, which is significantly poorer than before. Thus, it seems that there is a real energy shift and not an apparent energy shift, caused perhaps by some other, as yet unidentified, mistake made in the experiment or in the analysis.

It is interesting to plot the normalization factor, N, versus the energy adjustment factor, F, for the case where the monitor foil energies were recalculated and the Sum-of-Squares reached a minimum. This is shown in Fig. 2.12. Note that the range of the y-axis is very small, thus there is very little variation in N, within 1% around its mean value. This is rather reassuring, as it shows that the determination of the integrated beam current is, for all practical purposes, unaffected by the attempt to determine the incident beam energy from the same monitor reaction data set.

Returning now to the reason why the McNemar's Chi-square of equation 2.3 was preferred

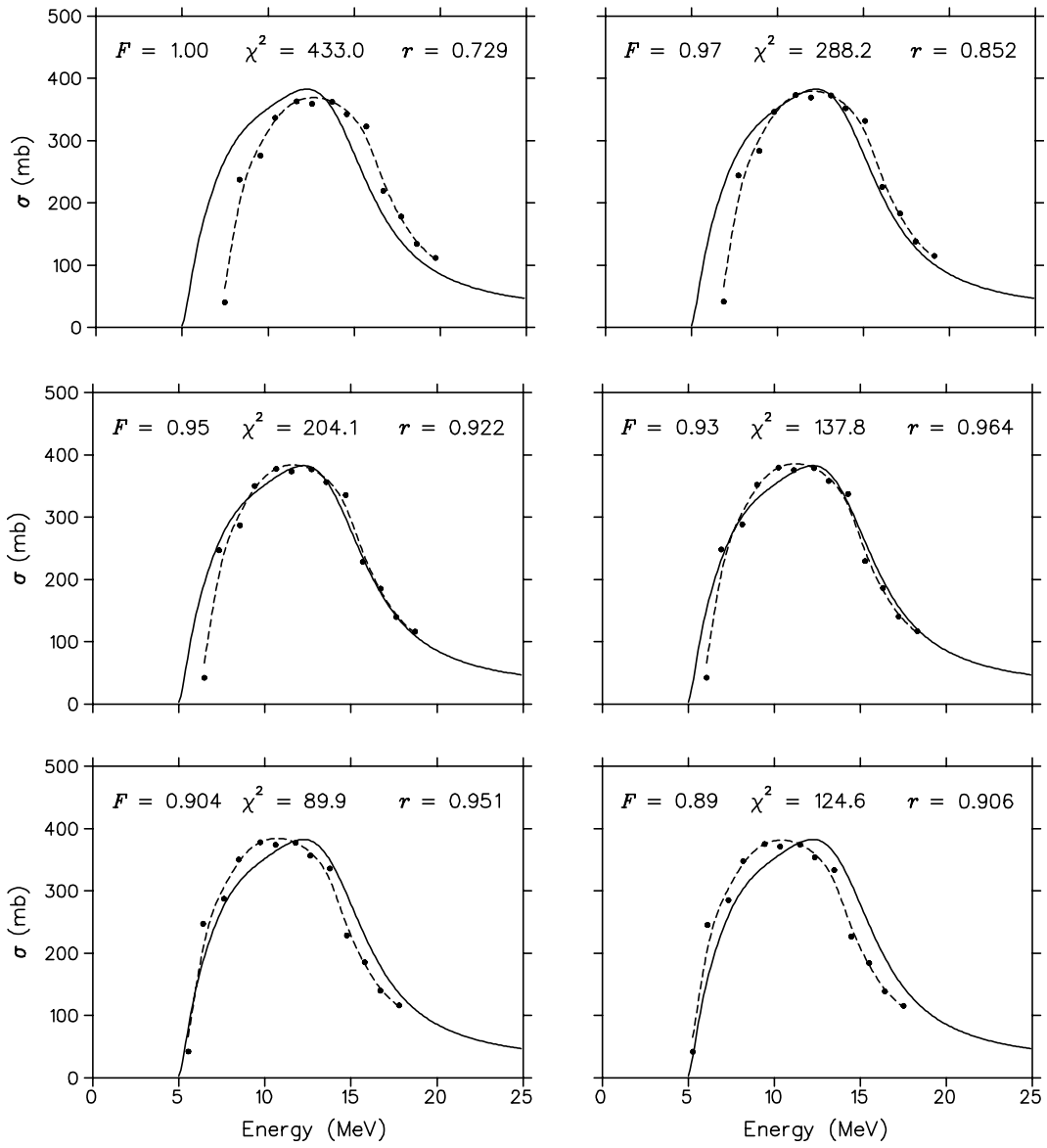

Figure 2.11: Recommended ^{48}V excitation function for Ti + p (solid curves) and the cross-section values extracted from the activated Ti monitor foils, for different energy adjustment factors. In this case, however, the shape of the measured excitation was artificially fixed (see text).

to the normal Chi-square: The normal Chi-square is given by

$$\chi^2 \;=\; \sum_{i=1}^{n}\left[\frac{(O_i - E_i)^2}{E_i}\right], \tag{2.5}$$

where the symbols have the same meaning as before. The ^{48}V excitation function (see Fig. 2.8) has a threshold near 5 MeV and a very steep gradient for the first few MeV above the threshold. It was found that the normal Chi-square of equation 2.5 gave terms having very large values in this low-energy region, even for cases where the fit seemed quite good. Conversely, the McNemar Chi-square was somewhat more well behaved, giving similar numerical values on the steep positive slope near the threshold and on the negative slope at the higher energies beyond the maximum, for the same level of goodness-of-fit. It

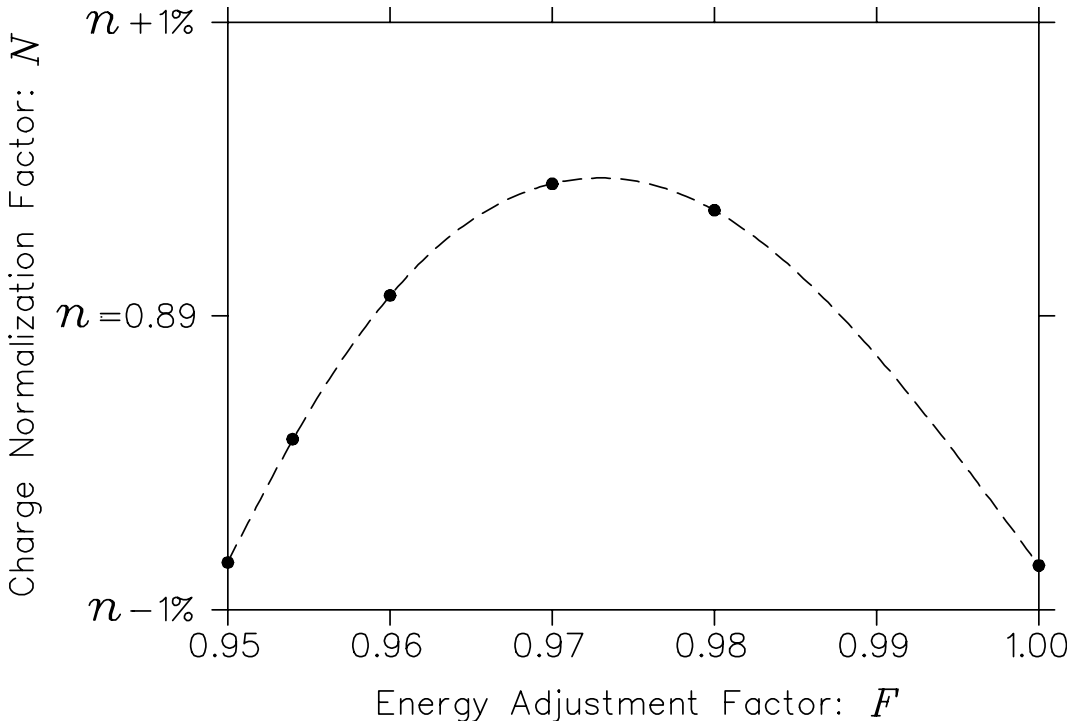

Figure 2.12: Normalization factor, N, plotted versus energy adjustment factor, F.

is also interesting to note that both the McNemar Chi-square and the Pearson product moment correlation coefficient (equations 2.3 and 2.4, respectively) treat the "observed" and "expected" variables on the same footing (those equations are symmetrical to an exchange of variables), while an exchange of variables gives different results when the normal Chi-square is used.

Perhaps our preference for the McNemar Chi-square was somewhat ad hoc, nevertheless, in practice it makes very little difference. Using the normal Chi-square of equation 2.5 leads to an almost identical result.

We still have to explain why the Sum-of-Squares minimization was preferred to a Chi-square minimization during the vertical shift to obtain the normalization factor N. The Sum-of-Squares is given by

$$S^2 \;=\; \sum_{i=1}^{n}\Big[(O_i - E_i)^2\Big], \tag{2.6}$$

where the symbols have the same meaning as before. This expression is very similar to the Chi-square expressions except for the absence of the denominator, which can be seen as a weighing factor. Thus, in the Sum-of-Squares, more weight is given to the larger numerical values, while the Chi-square endeavours to give all points equal weight. In the case of excitation functions, it can be argued that the larger values close to the maxima are more important, especially if the objective will be to integrate the excitation function numerically to obtain integral yields. Those regions of the excitation function where the

cross sections are larger, contribute more to the integral, thus to the yield. Ultimately, it is the yield that we want to estimate from the excitation functions for particular energy windows. It should be stressed, however, that the choice of minimizing the Sum-of-Squares had a very minimal effect on the actual values extracted for N. Minimizing Chi-square, instead, would have given almost the same results.

The rest of the data analysis performed was similar to that described in Section 2.1.3 for ^{141}Pr + p. A somewhat higher total systematic uncertainty of 10% was estimated in the case of the thick-target production rate measurements on La_2O_3, mainly because of a larger uncertainty in the beam flux determination from the Ti monitor foils (based on the overall goodness of fit). Since these activations differed mainly in that the targets used were thicker than those used in the stacked-foil experiments, several of the individual uncertainties were the same as before: detector efficiency (5%), counting geometry (1%) and decay corrections (2%). There was no uncertainty associated with the target thickness as the beam was always stopped inside a target. There was, however, an uncertainty associated with the thickness of the monitor foils, which was estimated to be about 3%. Details on the differentiation to obtain the ^{139}Ce excitation function from the measured thick-target production rate curve, will be given in a later chapter when the results are presented.

Lastly, one more item of evidence emerged pointing to a possible incorrect beam energy measurement on the Jülich CV28 cyclotron: Better agreement between the measured ^{139}Ce excitation function and a theoretical prediction was obtained when the redetermined beam energy was adopted. This will also be discussed further in a later chapter.

2.3 Activation of Ce Targets

2.3.1 Experimental Set-up and Irradiations

For the measurement of thick-target production rates of the Pr radionuclides formed in ^{nat}Ce + p, tablets of anhydrous $CeCl_3$ were irradiated at incident energies of 20, 26 and 32 MeV. In each case the target tablet was thick enough to stop the beam. A primary proton beam of 66 MeV was degraded to each desired energy by means of an accurately machined Cu degrader in front of each target tablet. These irradiations were performed in an accurately calibrated Faraday chamber [30], the details of which will be described below. Each irradiation lasted 20 minutes at a beam intensity of 40 nA. After bombardment, the $CeCl_3$ tablets were dissolved in 10 ml H_2O. Appropriate counting sources were made by transferring the solutions to standard serum vials.

The experimental facility used for these irradiations differed from the older one used in

the Pr + p investigations (see Section 2.1). The reason for this is that a small irradiation chamber previously used in nuclear physics experiments, which has some desirable properties for the activation of samples, became available for other experiments. A few modifications made it possible to irradiate foil stacks and/or other targets in the same type of stack holders as used before.

This irradiation chamber is based on the design of the RERAME facility of the Laboratory Nazionale del Sud (LNS) in Catania, Italy [31]. RERAME is an acronym for REcoil RAnge MEasurements, for which this chamber was originally designed. However, it has proved to be very versatile as a general facility for many kinds of activation studies. A collimator assembly with electron suppression has been designed for the chamber at iThemba LABS. A photograph of the modified version of the RERAME chamber is shown in Fig. 2.13. A vice mechanism for holding the targets in the irradiation position as well as the collimator assembly are mounted on the door of the chamber. A novel feature is that the door can be opened and turned through 180°, thus bringing parts which are normally inside the chamber outside. This allows for rapid and easy insertion and removal of targets. The door is also fitted with a rotatable handle which controls the opening and closing the jaws of the vice, allowing for samples or foil stacks of different thicknesses to be accommodated. The chamber is equipped with insulated feed-throughs for electrical connections, vacuum connections and a transparent port for viewing a fluorescent beam monitor with a TV camera. A beryllium oxide (BeO_2) viewer can be placed in the target position, which is useful for the initial focusing when the beam is first brought into the chamber. The entire chamber is electrically insulated and is provided with electron suppression at the beam entrance. It is, therefore, a true Faraday chamber and allows for the absolute measurement of the integrated beam current.

During irradiations, the beam current to the chamber and also the fraction of the beam which gets intercepted by the collimator are monitored continuously. The vacuum system of the chamber is completely independent because it has to be periodically isolated from the beam-line to insert or remove targets. A rotary pump provides fore vacuum ($\sim 10^{-3}$ mbar) and a turbo-molecular pump the high vacuum ($\sim 10^{-7}$ mbar). Fig. 2.14 presents a simplified diagram of the irradiation chamber, showing the position of the collimator relative to the beam entrance as well as the details of the collimator assembly. This assembly serves two purposes: (1) to prevent electrons stripped from the beam projectiles and/or emitted from materials hit by the beam from escaping, and (2) to define the beam spot on target. This allows for accurate positioning of a well-defined beam. The design of the collimator is such that the charge of beam particles which it intercepts can be measured accurately, *i.e.* it has its own electron suppression. Permanent samarium-cobalt magnets are used in a geometry which makes it impossible for secondary electrons to escape from the collimator

Figure 2.13: The modified RERAME irradiation chamber with the door in open position. The collimator and vice assemblies are mounted on the door. To ensure positional accuracy, the jaws of the vice move on guide rods. The beam enters the chamber from the left. (See text for further details.)

to the target and chamber or from the target to the collimator. The collimator side and target side of the assembly are separated by a section of glass-ceramic (Macor) insulator, while the permanent magnets provide strong magnetic fields which very effectively trap all secondary and delta electrons. The collimator inside the assembly is interchangeable. For this present work, a Cu collimator of 7 mm thickness with a 4 mm circular aperture was selected.

The procedure adopted for the focusing of the beam was as follows: When beam was first brought into the irradiation chamber, the collimator was removed and the BeO_2 viewer was placed in the irradiation position. The final sets of quadrupoles in the beamline were then adjusted until a well-defined beam spot was obtained on the viewer. The viewer was then removed, the collimator replaced and a dummy target mounted in the irradiation position. The quadrupoles were then adjusted to defocus the beam, until about 50% of the beam intensity was measured on the collimator and 50% on the target. The beam spot was then assured to be well-defined but with no sharp intensity gradients on target. The beam current on the target and beam stop was measured with a Brookhaven Instruments model 1000C current integrator. The accumulated charge was also logged in 10 second intervals, which made it possible to correct for beam intensity fluctuations during bombardment, if

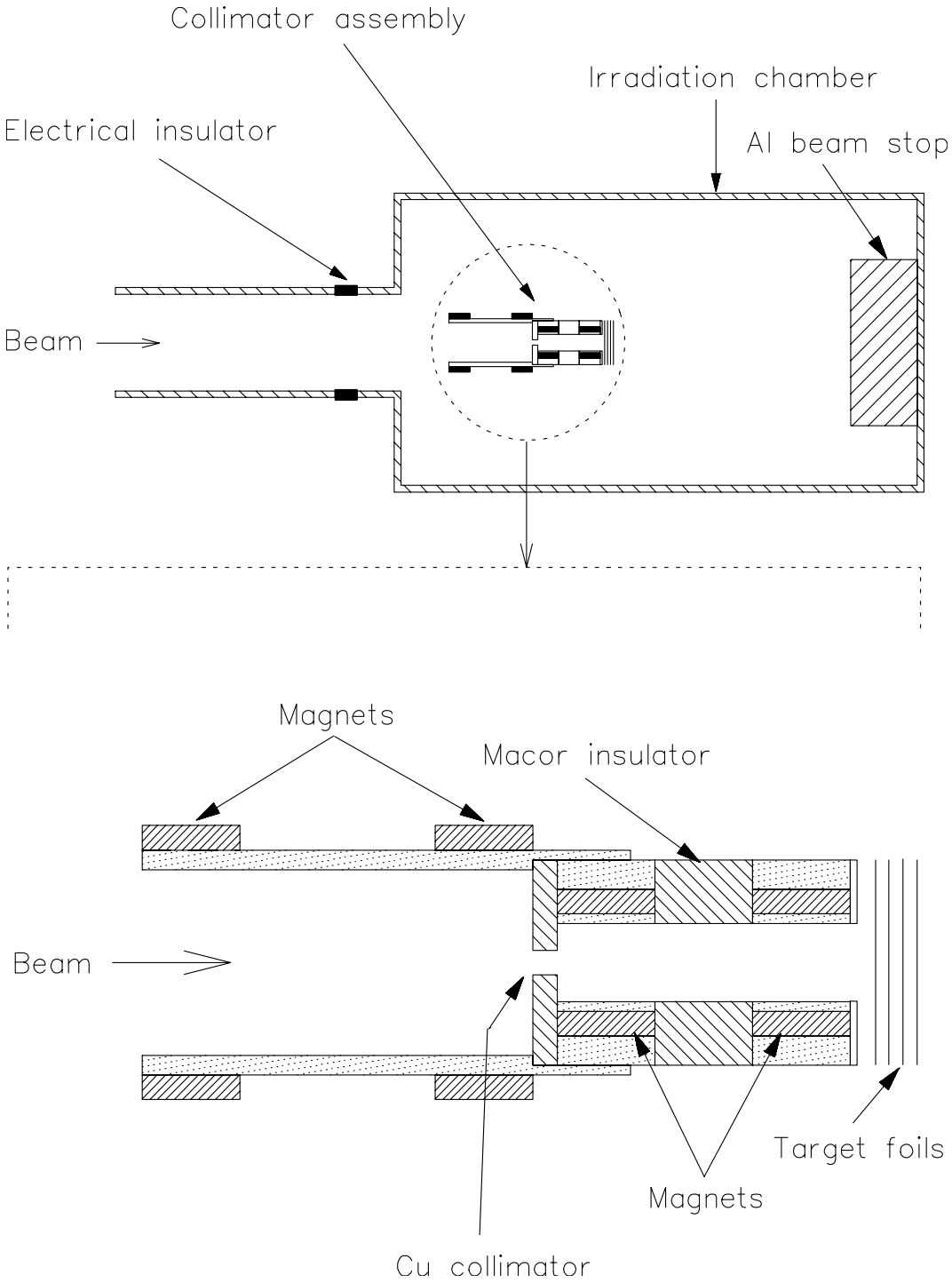

Figure 2.14: Diagrammatic representation of the modified RERAME irradiation chamber, showing the position of the collimator assembly (TOP) and an enlarged cross-sectional view of the collimator assembly (BOTTOM).

required. A Keathley electrometer was used to measure the current intercepted by the collimator. The chamber had been thoroughly tested with protons as well as beams of other charged particles prior to this work. Excellent agreement was found between direct current integration and values extracted using recommended monitor reactions. More details on these tests can be found in Ref. [30].

2.3.2 Radionuclide Assays and Data Analysis

After the sources were prepared by sealing the solutions in serum vials, they were individually assayed by means of standard off-line γ-ray spectrometry, using an accurately calibrated HPGe detector connected to a Silena EMCAPLUS multi-channel analyser. The yields of several Pr radionuclides were extracted using the same nuclear data, corrections and the associated uncertainties described in Sections 2.1.2 and 2.1.3 (see also Table 2.1).

Chapter 3

Nuclear Data: Theoretical Calculations

3.1 Overview

In this work, the focus is primarily on proton-induced reactions in the energy region up to 100 MeV and those nuclear processes which dominate the formation of the residual radionuclides. The theoretical formalisms which are useful for predicting the formation cross sections of heavy target-like residues are the so-called semi-classical pre-equilibrium-evaporation models [20]. For reasons which will be explained below, direct reaction mechanisms only play a very minor role in the formation of residual radionuclides and their contributions are therefore usually neglected.

For the purposes of the present discussion, it is appropriate to briefly revisit the main classes of reaction mechanisms. It is also extremely useful to refer to a typical inclusive spectrum of protons emitted from a thin target during bombardment with protons (*i.e.* the emission spectrum of a (p,p') reaction). Figure 3.1 (top) shows a diagram of such an experiment, utilizing a particle detector of an appropriate type to measure the energy of emitted protons at a forward scattering angle, θ. The measured spectrum is usually expressed as a double-differential cross section, as shown in Fig. 3.1 (bottom). Various characteristic features of this spectrum can be associated with different reaction mechanisms, as discussed below.

The *direct reactions* take place on a time scale comparable with the time it takes the projectile to traverse the target nucleus, typically of the order of 10^{-22} s. The simplest direct reaction is *elastic scattering*, which leaves the target nucleus in its ground state. *Inelastic scattering* typically excites the target nucleus to a low lying discrete state which has a simple structural relationship with the ground state. In these reactions, the energy transferred from the projectile to the target nucleus is relatively small and an ejectile with

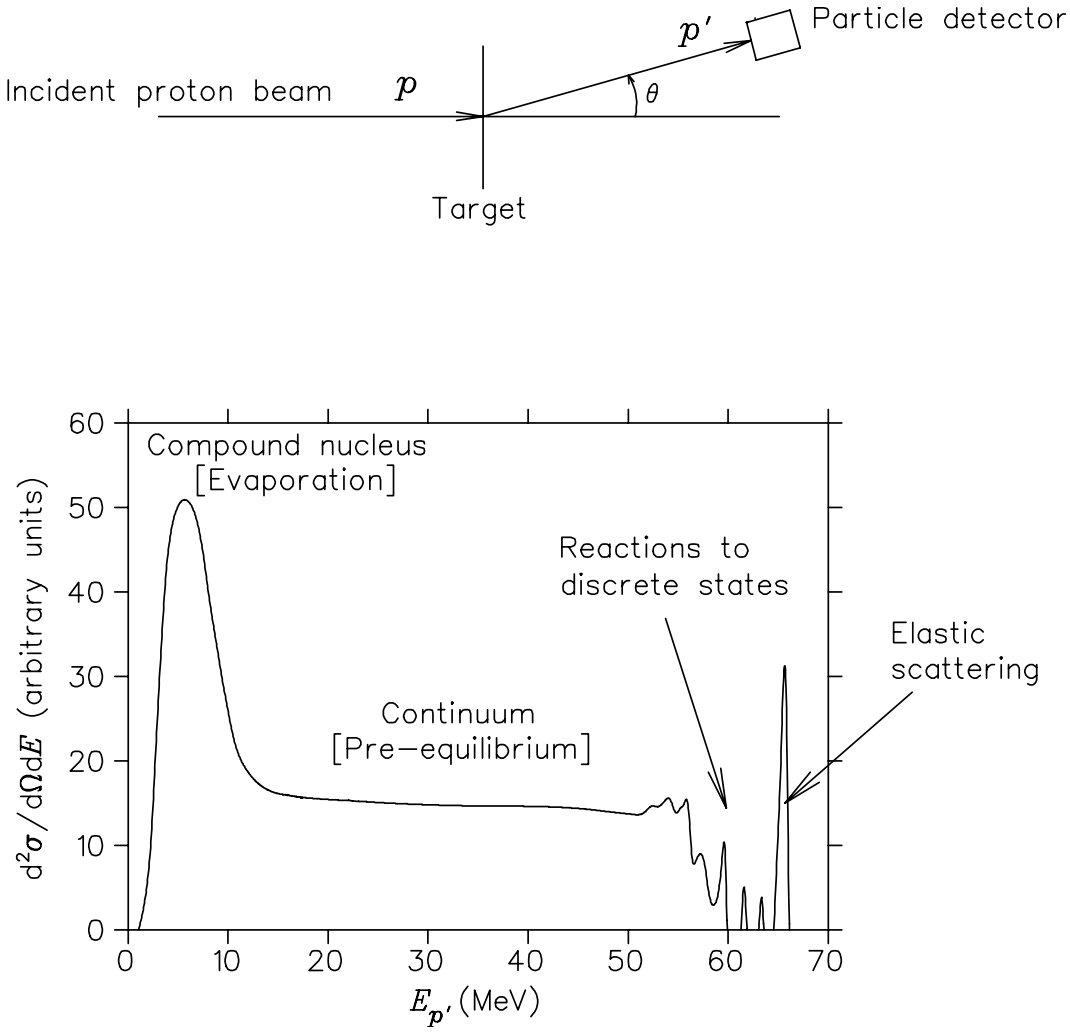

Figure 3.1: Typical experimental set-up (top) to measure the inclusive emission spectrum (bottom) of protons emitted from a thin target. (Idea of figure developed from similar sketch in Ref. [32] by Gadioli and Hodgson.)

properties very similar to the projectile can be observed. Particle emission following the reaction is unlikely and the nucleus will usually de-excite by γ-emission until it reaches the ground state. Although giant resonances may be excited which are more likely to decay by particle emission, these reactions do not occur with a high probability.

A very different class of reactions is the *compound nucleus reactions*. In these reactions, the projectile is absorbed by the target nucleus and the excitation energy is shared amongst all the nucleons by means of successive two-body nucleon-nucleon collisions until the compound nucleus reaches a state of statistical equilibrium. Because of the rapid sharing of excitation energy amongst many nucleons during the initial stages of the reaction, a situation is quickly reached where the individual nucleons do not have enough energy to readily escape. Thus, as the emission probability decreases sharply during the evolution of the reaction, the time scale of compound nucleus reactions increases dramatically compared to that of direct reactions. In fact, the average time period for an evaporation event to occur

may be 10^6–10^7 times longer than the projectile transit time. The emission of particles becomes a statistical process with characteristics similar to the *evaporation* of molecules from a heated liquid drop. Purely by chance and as a result of statistical fluctuations due to the many collisions that occur, a nucleon or cluster of nucleons near the nuclear surface may occasionally receive enough energy to escape. The emission spectrum of Fig. 3.1 very beautifully shows a broad evaporation peak with a Maxwellian shape towards the low-energy side of the spectrum, in contrast to the sharp peaks which characterize elastic scattering and reactions to discrete states at the highest emission energies.

Although there are some notable exceptions which will not be discussed here, by and large the direct reactions are fast and lead to the emission of particles with relatively high kinetic energies. In contrast, compound nucleus reactions are slow and lead to the emission of particles with relatively low kinetic energies. Between these two extremes, a third reaction mechanism represents processes which are neither direct, nor compound. These so-called *pre-equilibrium reactions* (also sometimes called pre-compound reactions) occur at times which are longer than the projectile transit time, yet much shorter than for compound nucleus formation. The emission of particles occurs before statistical equilibrium of the nucleus is reached, consequently, their energies are higher than those of evaporated particles but lower than those emitted during direct reactions. The pre-equilibrium part of the spectrum is also rather flat and featureless, as shown in Fig. 3.1.

It is important to note the relative contributions to the *total cross section* of these various reaction mechanisms (*i.e.* the number obtained when the data of which Fig. 3.1 forms a small part are integrated over the full energy region and solid angle.) In the mass and energy region relevant to the present study, elastic scattering and direct reactions contribute about 3%. The contribution from evaporation is not expected to exceed 20%. Thus, the contribution from pre-equilibrium reactions is of the order of 80%. The compound and pre-equilibrium reactions lead to high excitation of the target nucleus and to significant particle emission, thus they dominate the formation of heavy residues different from the target species. Not only is the probability of particle emission from the direct reactions considerably smaller (*i.e.* the probability to produce radionuclides of non-target species), their contribution to the total cross section is also considerably smaller, thus for both these reasons it is justified to neglect them.

3.2 The ALICE-IPPE computer code

A number of computer codes based on compound and pre-equilibrium nuclear reaction mechanisms exist which can be employed to predict the formation cross sections of heavy residues in a nuclear reaction (*e.g.* STAPRE, ALICE, GNASH, etc. [20]) Although the

underlying physics of these codes is similar, they differ largely in the complexity of implementation and input preparation (mainly due to the level of approximations made to simplify computation). Consequently, the required computing time of these codes vary dramatically. For very detailed calculations of the properties of nuclear reactions where one needs information on each participating channel, codes like STAPRE and GNASH are often employed. The downside is that calculations for a whole family of excitation functions of a particular nuclear reaction become a formidable task. The ALICE code is much faster, require much less input and is more user friendly. It is usually sufficient to estimate optimum bombarding energies for many proton induced reactions [20] and, surprisingly, generate predictions which are by and large not inferior to predictions by the larger codes. The ALICE code has been written to be versatile, yet easy to be used by non-nuclear physicists [33]. For these reasons, it has become the workhorse for theoretical predictions by the radionuclide production community.

Various evolutions of the ALICE code appeared since the early seventies. One of the latest versions, ALICE-IPPE (developed at Obninsk) is a modification of the ALICE-91 code developed by Marshall Blann [34]. The ALICE codes perform equilibrium decay (evaporation) calculations using the *Weisskopf-Ewing* formalism. Pre-equilibrium decay is treated using the *Geometry Dependant Hybrid (GDH) model* approach. ALICE-IPPE was developed and used for the creation of the Medium Energy Nuclear Data Library, MENDL-2, to study activation and transmutation of materials irradiated with nucleons of intermediate energies and for other applications. This flavour of the code uses the Generalized Superfluid model of Ignatyuk and colleagues [35], which includes shell effects and collective enhancements. The code also includes pre-equilibrium cluster emissions in the calculations, which previous incarnations of the ALICE code neglected.

In the following section, a short description is given of the main concepts that drive the ALICE-IPPE code.

3.3 The Hybrid and Geometry Dependant Hybrid models

The Hybrid model is largely based on an approach first published by Griffin [36] for calculating the excited particle populations during equilibration in an excited nucleus (which led to the development of the so-called Exciton models), except that the intra-nuclear transition rates are determined from calculations of the mean free paths of nucleons in nuclear matter [37]. It is assumed that the projectile fuses with the target nucleus and remains bound in an intermediate nucleus which is far from statistical equilibrium. It is

further assumed that equilibration of this intermediate nucleus is achieved by a succession of two-body nucleon-nucleon interactions, also sometimes called the intra-nuclear cascade. Thus, as the reaction proceeds, the nucleus is progressively excited to more and more complex states, each of which is characterized by the number of excited particles (p) above the Fermi energy plus holes (h) below the Fermi energy. The number $n = p + h$ is called the exciton number and collectively the particles above and holes below the Fermi energy (ε_f) are referred to as excitons.

This process is diagrammatically depicted in Fig. 3.2, where a proton with energy E above the Fermi energy is incident upon a target nucleus in its ground state. Before any nuclear interaction takes place, one can view the system as having an exciton number of $n = 1$. In the first nucleon-nucleon interaction, the projectile proton becomes bound by exciting a target nucleon above the Fermi energy. The resulting nucleus is now in a $2p$-$1h$ state, thus the exciton number increases to $n = 3$. A further nucleon-nucleon interaction may lead to a $3p$-$2h$ state, taking the exciton number to $n = 5$. In principle, this process can continue until the nucleus achieves statistical equilibrium, always increasing the exciton number by $\Delta n = +2$ in each successive interaction. However, two other phenomena need to be addressed. One must make provision for the emission of particles, which has a finite probability at each stage of the interaction chain. In the Hybrid model, if any nucleon obtains enough energy to become unbound, it has a finite probability to escape and thus be emitted into the continuum. Thus, for each exciton number (or exciton configuration) there is competition between emission and a further interaction which will increase the complexity of the nuclear state. Note, however, that this last statement is only approximately true, as energetically it is always possible that a further step may reduce the exciton number by 2 (*i.e.* $\Delta n = -2$). This, however, is rather improbable, especially for states which have low exciton numbers. The "never come back" approximation is therefore enforced in the theory, which only allows for Δn to be positive. The density of states of p excited particles and h holes (called a partial state density) also rapidly increases as the exciton number increases. All the states of a given exciton configuration is also assumed to be equally probable.

In order to calculate the excitation functions of heavy residues in a nuclear reaction, it is necessary to keep track of the number and type of emissions from the combined nuclear system (projectile plus target nucleus) as well as the energy carried away by these emissions. If, for the moment, the pre-equilibrium (PE) decay is considered to involve only individual protons and neutrons (neglecting clusters of protons and neutrons), the PE decay probability [32] in the Hybrid model and in the Geometry Dependent Hybrid model (a later enhanced version of the Hybrid model) can be written, respectively, as

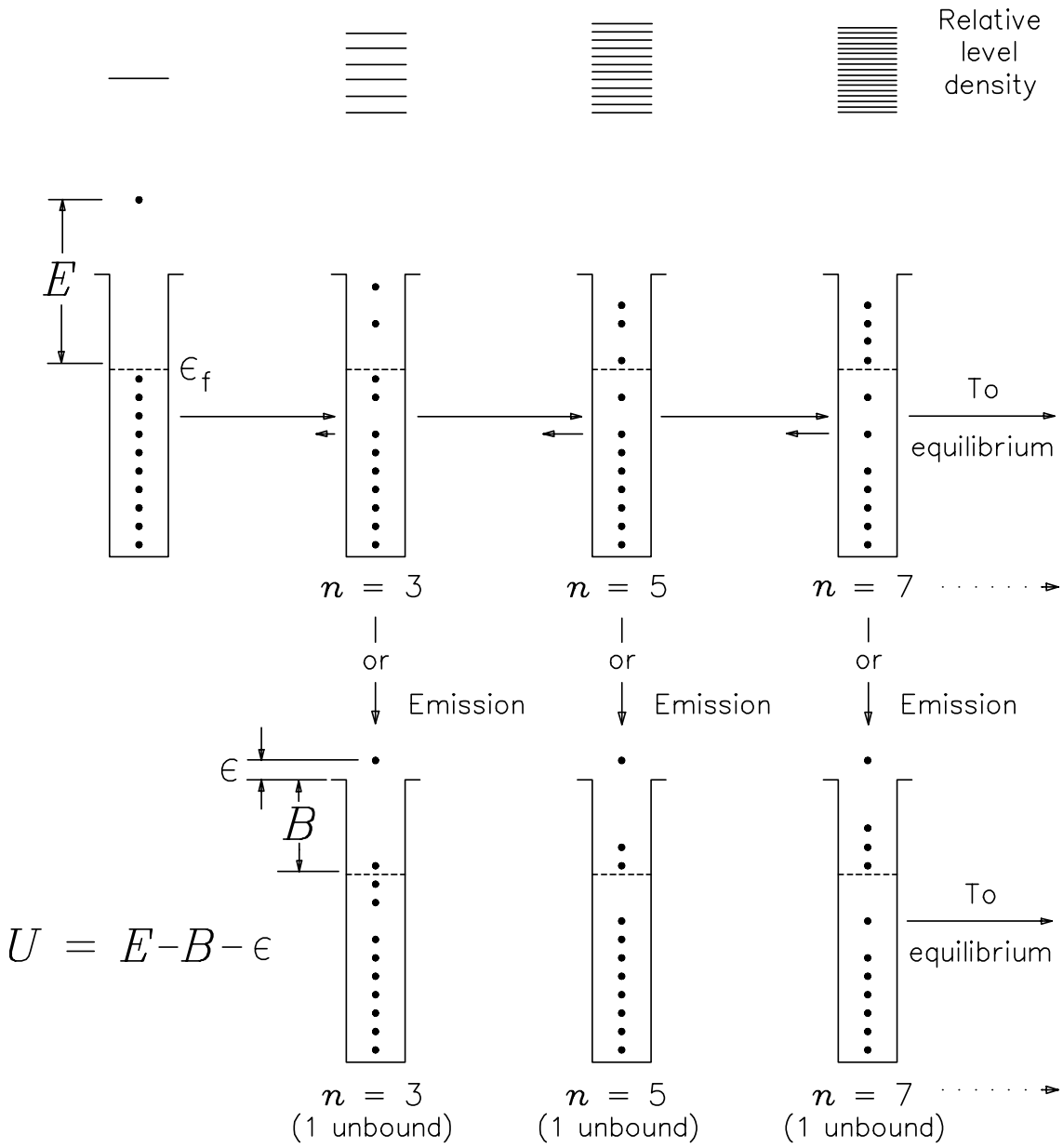

Figure 3.2: Schematic representation of the first few stages of a nucleon-induced reaction in the Exciton, Hybrid or GDH models. The solid symbols represent single nucleons in equally-spaced, single particle levels in a nuclear potential well. The incident energy of the projectile nucleon, as measured from the Fermi energy ε_f, is denoted by E. B is the average nucleon binding energy and an escaping nucleon has an emission energy ε. (Idea of figure developed from similar schematic representation in Ref. [32] by Gadioli and Hodgson.)

$$P_x(\varepsilon_x)d\varepsilon_x = \sum_{n=n_o}^{\bar{n}} \left[R_x(n) \frac{\omega(p-1,h,U)}{\omega(p,h,E)} g d\varepsilon_x \right] \left[\frac{\lambda_c^x(\varepsilon_x)}{\lambda_c^x(\varepsilon_x) + \lambda_+^x(\varepsilon_x)} \right] D_n, \tag{3.1}$$

and

$$P_x(\varepsilon_x)d\varepsilon_x = K \sum_{l=o}^{l_{max}} (2l+1) T_l \sum_{n=n_o}^{\bar{n}} \left[R_x(n) \frac{\omega(p-1,h,U)}{\omega(p,h,E)} g d\varepsilon_x \right] \left[\frac{\lambda_c^x(\varepsilon_x)}{\lambda_c^x(\varepsilon_x) + \lambda_+^x(\varepsilon_x)} \right] D_n. \tag{3.2}$$

The PE energy differential cross section (angle integrated) is then given by

$$\frac{d\sigma_x^{PE}}{d\varepsilon_x} = \sigma_R P_x(\varepsilon_x). \tag{3.3}$$

Note the similarity between equation (3.1) and the second summation in equation (3.2), which we will discuss first: This summation is over the exciton number n, from an initial exciton number n_0 (which is 3 for a nucleon-induced reaction) in increments of $\Delta n = 2$ up to an upper value $\bar{n}$, which should be selected large enough so that it may be assumed that the nucleus has reached statistical equilibrium. (A value of $\bar{n}$ between 20 and 30 is usually sufficient). $R_x(n)$ is the number of particles of type x (either protons or neutrons) in the n-exciton state. The quantity $\omega(p,h,E)$ is the density of n-exciton states (having p particles and h holes) at an excitation energy E. This definition applies similarly to $\omega(p-1,h,U)$, where $U = E - B - \varepsilon_x$ is the residual excitation energy for sharing amongst $n-1$ remaining excitons should a particle which had a binding energy B be emitted with energy ε_x. The quantity g is the single-particle level density, while $d\varepsilon_x$ is an energy increment. (An energy bin size of 0.5 MeV was used in all calculations presented in this work.) Thus, the expression in the first set of square brackets gives the number of particles of type x in an n-exciton state that are in an unbound level with energy between ε_x and $\varepsilon_x + d\varepsilon_x$ in the continuum. The second expression in square brackets gives the fraction of those particles at energy ε_x which are emitted into the continuum, rather than interacting in a way that leads to a transition to a $n+2$ exciton state. Here, $\lambda_c^x(\varepsilon_x)$ is the particle decay rate to the continuum while $\lambda_+^x(\varepsilon_x)$ is the intra-nuclear collision probability per unit time. (Note that the denominator $\lambda_c^x(\varepsilon_x) + \lambda_+^x(\varepsilon_x)$ is the total particle decay rate). The quantity D_n is the so-called depletion factor for the n-exciton state, representing the fraction of the particle population surviving from simpler exciton states. Since the details of the calculation of all these quantities are rather voluminous, we will constrain the present discussion by mentioning that the densities of exciton states (or partial state densities) are calculated according to the Strutinski-Ericson formalism.

In the ALICE-IPPE code [13], one can specify whether the calculations should be performed according to the standard Hybrid model or the Geometry Dependent Hybrid model. In the standard Hybrid model, the effect of different impact parameters is not explicitly

considered but rather averaged over the nucleus as a whole. In the GDH, the diffuse surface of the nucleus, which is preferentially sampled in collisions at higher impact parameters, is explicitly incorporated. The different possible trajectories of the incident projectile relative to the target nucleus translate into different values of the entrance channel orbital angular momentum. The higher the impact parameter, the larger the orbital angular momentum and the more peripheral (*i.e.* confined to the nuclear surface) the interaction becomes. This is the reason why in equation (3.2) for the GDH, the first summation is over the orbital angular momentum. This summation is from $l = 0$, which represent the most central collisions, becoming progressively more peripheral as l increases, up to a sufficiently large cut-off value $l = l_{max}$, above which a nuclear interaction becomes unlikely. The quantity T_l is the transmission coefficient, calculated using the Optical model. The GDH model is thus built on the basic idea that the nucleus has a density distribution that can affect pre-equilibrium decay in two ways [38]. Firstly, the mean free path of a nucleon in the diffuse nuclear surface is expected to be longer. Secondly, there is a density dependant limit to the hole depth in the approximation of local density. This last statement is obvious, as intuitively one can understand that the allowed hole depth in the nuclear interior should be larger than at a radius where the nuclear density is, say, only one tenth of that of the interior.

To conclude this section, equation (3.3) should still be explained. The energy differential cross section of emitted pre-equilibrium nucleons of type x is just a partitioning of the *reaction cross section*, σ_R, by multiplying it with the probability for those kinds of pre-equilibrium events. The reaction cross section is inclusive of all reaction channels except the entrance channel, thus it is the same as the total cross section for all possible nuclear interactions excluding elastic scattering (*i.e.* $\sigma_R = \sigma_T - \sigma_{el}$).

3.4 Further refinements, multi-particle and cluster emission

The ALICE-IPPE code differs from its predecessor, ALICE-91, in that pre-equilibrium cluster emission has been incorporated in the code. For this purpose, additional expressions remarkably similar in form to equation (3.2) have been formulated, with summations over orbital angular momenta and exciton numbers appropriate for the clusters. For pre-equilibrium deuteron emission, a nucleon pick-up is assumed prior to the emission. In a similar fashion, triton and ^{3}He emission spectra are incorporated according to the *coalescence pick-up model* of Sato, Iwamoto and Harada [39, 40]. In the case of α-particle emission, both coalescence pick-up and knock-out processes have been incorporated. In the case of knock-out, the emission rates of pre-formed α-clusters according to Oblozinski

and Ribanski [41] were used. It is beyond the scope of this thesis to present the details.

The multiple pre-equilibrium nucleon emission of previous versions of the ALICE code has been retained. Let P_n and P_p denote the emission probabilities for neutrons and protons, respectively, from a particular n-exciton configuration. The probability for emission of both a neutron and a proton from the same exciton state is then given by $P_{np} = P_n P_p$. The emission of two neutrons is given by $P_{nn} = P_n P_n/2$.

In previous versions of the ALICE code, single particle level densities were calculated using a Fermi gas model. In ALICE-IPPE, the option has been included to calculate the level densities according to the Generalized Superfluid model (GSM) [35, 42].

3.5 Calculations

The ALICE-IPPE calculations presented in this work were performed using the recommended values of the input parameters according to the comments in the preamble to the code. No attempt was made to fine-tune the calculations in order to obtain better agreement for individual residual nuclides. Level densities were calculated according to the Generalized Superfluid model. The normal pairing shift was selected. Experimental nuclidic masses were used where available, else calculated using the built-in Myers and Swiatecki mass formula of the code. A level density parameter of $a = A/9$ was used throughout. The energy bin size was 0.5 MeV. The evaporated particles included protons, neutrons, deuterons and α-particles.

3.6 Comments in conclusion

The GDH model is quite successful in reproducing the angle-integrated emission spectra of nucleons emitted into the continuum. A shortcoming of the code is that the Hauser-Feshbach theory used to describe the evaporation does not explicitly take the conservation of angular momentum into account, thus it does not accurately predict angular distributions, nor does it predict the excitation functions of residues formed in long-lived isomeric states. In this work, such cases were either scaled or added incoherently with the ground state, for purposes of comparison with the ALICE-IPPE predictions.

It is interesting that, unlike the authors of the original ALICE codes [34], the authors of ALICE-IPPE [13] insist that the Hybrid model is a bona-fide version of the Exciton model. They therefore insist on the names Hybrid Exciton model and Geometry Dependent Hybrid Exciton model.

Chapter 4

Nuclear Data: Results and Discussion

4.1 Results relevant to ^{139}Pr production

4.1.1 Excitation functions

The measured cross sections for the production of Nd and Pr radionuclides are presented in Tables 4.1 and 4.2 as well as Figs. 4.1, 4.2 and 4.3. All the cross-section values are for the direct production of the particular radionuclides. In the case of ^{138m}Pr there is no feeding from precursor decay. In the case of ^{136}Pr and ^{137}Pr, the contributions to the γ-ray photo-peak areas from the decay of the respective Nd precursors were subtracted first, in order to obtain cross sections for their direct production. Unfortunately, the cross sections for the ^{141}Pr(p,p2n)^{139}Pr reaction could not be extracted in the same way, since the intensities of the γ-rays from ^{139}Pr decay are extremely weak, resulting in photo-peaks which were not well resolved from the Compton background. However, since this reaction leads to a product that is not carrier free, it was not considered essential for the present study as the focus is on the production of no-carrier-added ^{139}Pr.

The various sets of excitation function data for the production of the radioneodymiums produced in ^{141}Pr + p are compared in Fig. 4.1. Except for a few outlying points, the agreement with data of Hilgers *et al.* [10] is satisfactory. Since the focus of the present study is the higher-energy region, the comparison with older data below 20 MeV is not repeated.The only results above 45 MeV found in the literature are by Hogan [43]. This author presented cross sections at selected energies up to 85 MeV for ^{141}Nd, ^{140}Nd, ^{139m,g}Nd and ^{138}Nd. The agreement with the present results is generally poor (significantly higher values by Hogan and a different shape of the excitation functions for both ^{141}Nd and ^{140}Nd, while significantly lower values for ^{138}Nd than the present work). In the case of $^{139m+g}$Nd, however, the agreement is reasonable. Note that in the case of $^{139m+g}$Nd, the ^{139m}Nd and

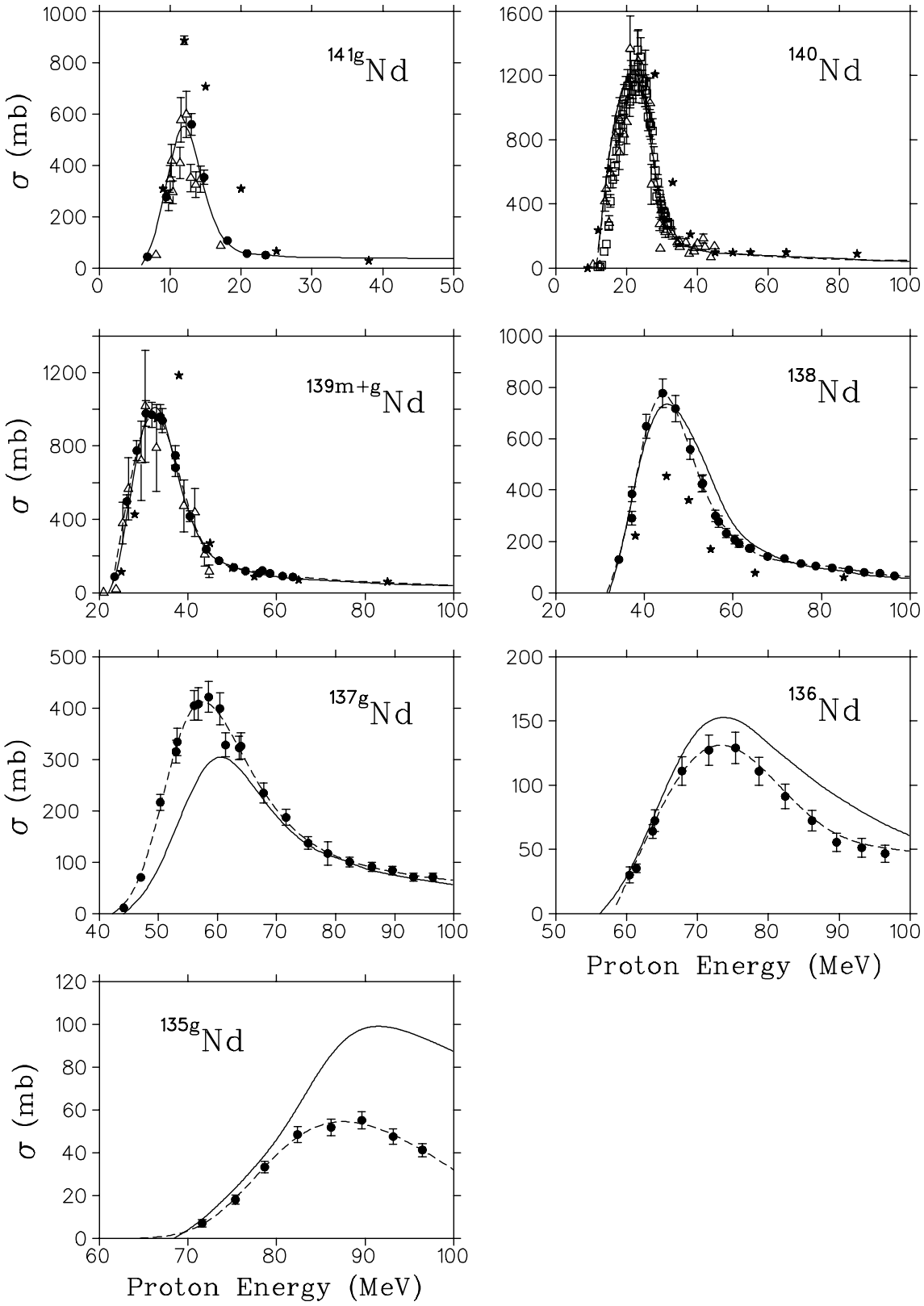

Figure 4.1: Excitation functions for the production of the denoted Nd radionuclides in the irradiation of ^{141}Pr with protons. The solid circles are the experimental values of this work. The open squares are the measurements of Becker [5]. The open triangles are the measurements of Hilgers *et al.* [10]. The solid stars are the measurements of Hogan [43]. The solid curves are theoretical predictions by means of the code ALICE-IPPE (see text). The dashed curves are polynomial fits used for numerical integration in order to obtain the thick-target production rates for the denoted radionuclides.

Table 4.1: Measured cross sections for the production of the denoted radionuclides in the irradiation of ^{141}Pr with protons

Energy	Cross section[a] (mb)				
(MeV)	^{135g}Nd	^{136}Nd	^{137g}Nd	^{138}Nd	^{139g}Nd
23.5 ± 1.06	—	—	—	—	34.8 ± 2.54
26.2 ± 0.94	—	—	—	—	189.5 ± 13.6
28.5 ± 0.87	—	—	—	—	256.9 ± 18.3
30.5 ± 0.76	—	—	—	—	312.1 ± 22.7
31.9 ± 0.71	—	—	—	—	276.7 ± 19.7
33.8 ± 0.66	—	—	—	—	248.1 ± 17.7
34.3 ± 0.61	—	—	—	129.4 ± 12.6	269.8 ± 19.8
37.1 ± 1.55	—	—	—	290.1 ± 26.0	171.1 ± 12.3
37.2 ± 0.55	—	—	—	383.9 ± 29.0	174.2 ± 13.0
40.5 ± 1.42	—	—	—	647.8 ± 47.2	107.4 ± 8.71
44.1 ± 1.31	—	—	11.3 ± 1.88	776.5 ± 55.8	62.5 ± 5.42
47.0 ± 1.21	—	—	70.9 ± 5.79	716.7 ± 51.6	48.2 ± 4.65
50.3 ± 1.13	—	—	216.8 ± 15.8	558.4 ± 40.4	36.0 ± 3.84
53.0 ± 1.04	—	—	315.6 ± 22.7	422.5 ± 30.9	29.8 ± 4.16
53.2 ± 2.52	—	—	334.4 ± 27.1	425.9 ± 32.1	—
56.1 ± 0.97	—	—	405.1 ± 28.9	299.0 ± 22.3	29.3 ± 3.63
56.8 ± 2.29	—	—	408.0 ± 31.8	276.7 ± 21.4	41.1 ± 8.88
58.5 ± 0.90	—	—	421.8 ± 30.1	231.5 ± 17.7	31.5 ± 3.05
60.4 ± 2.08	—	30.1 ± 6.25	399.2 ± 31.1	206.8 ± 16.4	—
61.4 ± 0.71	—	35.2 ± 3.36	328.6 ± 23.4	191.7 ± 15.0	24.6 ± 2.87
63.7 ± 0.62	—	64.1 ± 5.33	322.8 ± 23.1	172.6 ± 14.02	24.7 ± 3.55
64.0 ± 1.90	—	72.5 ± 8.36	326.3 ± 25.6	172.8 ± 13.6	—
67.8 ± 1.74	—	111.1 ± 11.1	234.8 ± 19.3	141.0 ± 11.8	—
71.6 ± 1.59	7.1 ± 1.76	127.3 ± 11.9	187.5 ± 15.6	132.9 ± 11.1	—
75.4 ± 1.45	18.1 ± 2.07	129.1 ± 12.1	137.4 ± 12.3	113.6 ± 9.90	—
78.7 ± 1.31	33.3 ± 2.71	110.9 ± 10.8	117.2 ± 12.7	103.8 ± 9.22	—
82.4 ± 1.18	48.5 ± 3.74	91.4 ± 9.46	100.9 ± 9.56	96.4 ± 8.72	—
86.2 ± 1.06	51.9 ± 3.86	72.4 ± 8.15	91.3 ± 8.90	88.6 ± 8.33	—
89.6 ± 0.94	55.1 ± 4.09	55.6 ± 6.99	84.3 ± 8.28	78.8 ± 7.54	—
93.2 ± 0.83	47.5 ± 3.52	51.4 ± 7.23	71.5 ± 7.91	75.9 ± 7.69	—
96.5 ± 0.72	41.3 ± 3.07	46.8 ± 6.60	71.3 ± 7.57	65.3 ± 6.96	—

[a]The error values listed include a systematic uncertainty, which is estimated to be about 7% (see text).

Table 4.2: Measured cross sections for the production of the denoted radionuclides in the irradiation of ^{141}Pr with protons

Energy	Cross section[a] (mb)				
(MeV)	^{139m}Nd	^{141g}Nd	^{136}Pr	^{137}Pr	^{138m}Pr
6.8 ± 2.43	—	44.0 ± 5.22	—	—	—
9.4 ± 2.09	—	277.6 ± 22.1	—	—	—
13.0 ± 1.82	—	559.5 ± 42.0	—	—	—
14.8 ± 1.58	—	353.3 ± 27.4	—	—	—
18.1 ± 1.37	—	106.9 ± 9.84	—	—	—
20.8 ± 1.20	—	56.9 ± 6.30	—	—	—
23.5 ± 1.06	52.1 ± 3.84	50.6 ± 11.5	—	—	—
26.2 ± 0.94	307.5 ± 21.7	—	—	—	—
28.5 ± 0.87	517.4 ± 36.4	—	—	—	—
30.5 ± 0.76	664.6 ± 50.0	—	—	—	—
31.9 ± 0.71	693.2 ± 48.7	—	—	—	3.0 ± 0.61
33.8 ± 0.66	711.1 ± 49.9	—	—	—	3.2 ± 0.62
34.3 ± 0.61	668.6 ± 47.2	—	—	—	5.5 ± 0.65
37.1 ± 1.55	576.9 ± 40.5	—	—	—	6.2 ± 0.82
37.2 ± 0.55	507.4 ± 35.8	—	—	—	8.9 ± 0.85
40.5 ± 1.42	308.7 ± 21.8	—	—	—	22.1 ± 1.72
44.1 ± 1.31	173.9 ± 12.3	—	—	—	44.7 ± 3.26
47.0 ± 1.21	126.3 ± 8.92	—	—	—	60.8 ± 4.38
50.3 ± 1.13	101.8 ± 7.20	—	—	503.6 ± 91.9	75.9 ± 5.43
53.0 ± 1.04	87.8 ± 6.21	—	1.8 ± 0.40	741.5 ± 94.9	77.4 ± 5.52
53.2 ± 2.52	91.2 ± 6.61	—	—	722.5 ± 124.1	81.0 ± 5.94
56.1 ± 0.97	77.5 ± 5.48	—	7.5 ± 0.66	861.38 ± 94.2	76.2 ± 5.43
56.8 ± 2.29	79.3 ± 5.72	—	19.1 ± 2.16	925.6 ± 129.8	77.4 ± 5.67
58.5 ± 0.90	73.2 ± 5.18	—	21.1 ± 1.57	1029.8 ± 103.9	75.9 ± 5.40
60.4 ± 2.08	69.8 ± 5.03	—	37.1 ± 7.06	999.5 ± 122.2	73.5 ± 5.36
61.4 ± 0.71	66.1 ± 4.68	—	20.3 ± 2.71	887.6 ± 91.4	73.6 ± 5.25
63.4 ± 0.62	60.9 ± 4.32	—	46.4 ± 4.40	804.0 ± 82.5	69.6 ± 4.96
64.0 ± 1.90	63.3 ± 4.57	—	79.4 ± 9.28	788.2 ± 108.5	70.2 ± 5.12
67.8 ± 1.74	58.0 ± 4.17	—	129.6 ± 12.7	639.4 ± 88.0	68.3 ± 4.95
71.6 ± 1.59	54.5 ± 3.91	—	153.1 ± 13.8	642.5 ± 108.3	66.6 ± 4.82
75.4 ± 1.45	47.8 ± 3.43	—	151.4 ± 13.8	544.9 ± 96.3	63.4 ± 4.57
78.7 ± 1.31	43.9 ± 3.15	—	144.2 ± 12.9	380.4 ± 79.7	61.6 ± 4.43
82.4 ± 1.18	43.0 ± 3.08	—	137.2 ± 12.2	381.3 ± 70.5	59.0 ± 4.21
86.2 ± 1.06	38.4 ± 2.76	—	122.4 ± 10.9	351.6 ± 79.8	56.8 ± 4.04
89.6 ± 0.94	36.5 ± 2.62	—	124.3 ± 10.7	238.4 ± 55.7	54.1 ± 3.84
93.2 ± 0.83	32.7 ± 2.36	—	108.2 ± 10.0	224.9 ± 55.4	52.4 ± 3.71
96.5 ± 0.72	32.4 ± 2.33	—	105.8 ± 9.52	279.2 ± 55.3	51.9 ± 3.67

[a]The error values listed include a systematic uncertainty, which is estimated to be about 7% (see text).

^{139g}Nd cross sections were determined independently and added for purposes of comparison with the theoretical prediction as the ALICE-IPPE code does not take the spin of the final residual nuclei into account. The overall agreement between the new experimental data and the theoretical predictions is satisfactory. For the purpose of yield calculations, however, polynomial functions fitted through the data by means of non-linear regression were integrated numerically. These polynomials, obtained by means of the software code TABLECURVE [44], reproduce the data reliably as shown by the dashed curves in Fig. 4.1. As already mentioned, the ALICE-IPPE predictions were adopted only in a few cases where there was a lack of experimental data or if the data were considered to be unreliable (*e.g.* in the case of ^{140}Nd above 45 MeV).

Fig. 4.2 compares the available data for ^{139m}Nd only. The agreement between the present results and the results of Becker [5] is satisfactory. The values of Hogan [43] agree well in the low-energy slope region, reaches a marginally higher peak and follows a generally lower trend in the higher-energy tail region.

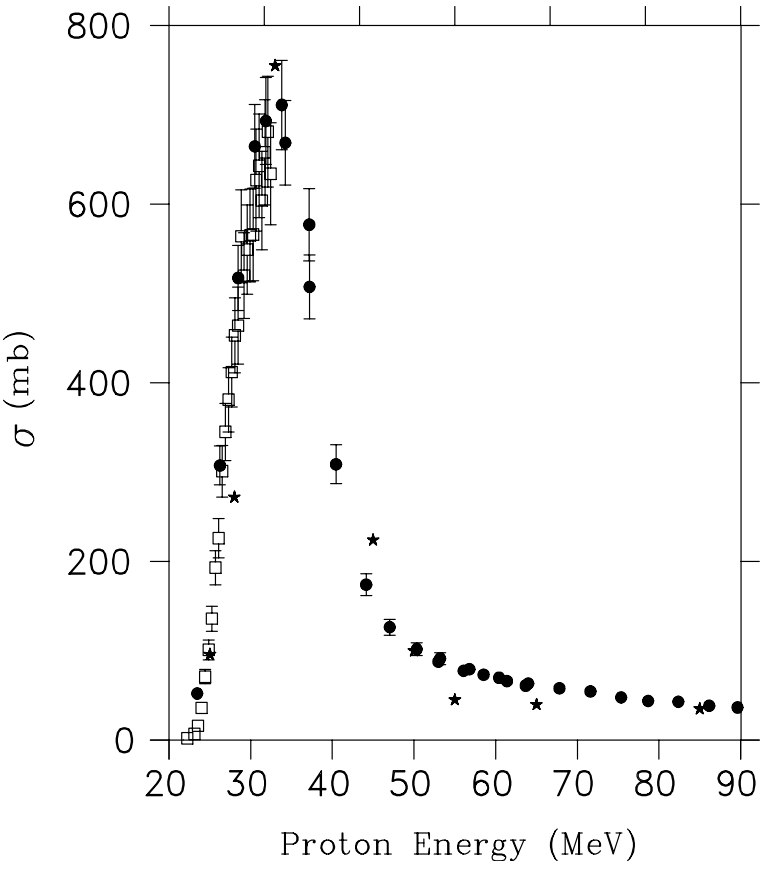

Figure 4.2: Excitation function for the production of ^{139m}Nd in the irradiation of ^{141}Pr with protons. The solid circles are the experimental values of this work. The open squares are the measurements of Becker [5]. The solid stars are the measurements of Hogan [43]. Error bars are shown only where these exceed the symbol size (see also caption to Fig. 4.1).

Excitation functions for the radiopraseodymiums observed in ^{141}Pr + p are shown in

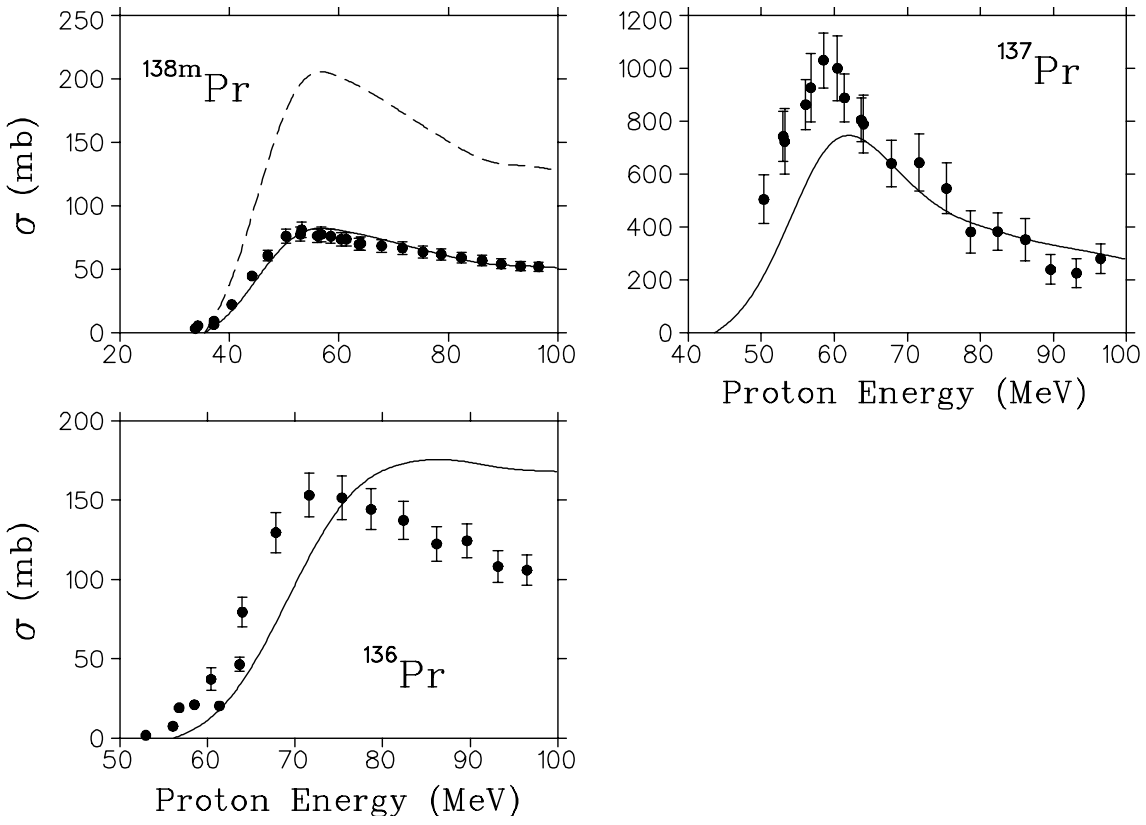

Figure 4.3: Excitation functions for the production of the denoted Pr radionuclides in the irradiation of ^{141}Pr with protons. The solid circles are the experimental values of this work. The curves are theoretical predictions by means of the code ALICE-IPPE (see text). In the case of ^{138m}Pr, the dashed curve is the unscaled calculation while the solid curve has been scaled to fit the data (see text). Error bars are shown only where these exceed the symbol size (see also caption to Fig. 4.1).

Fig. 4.3. The ALICE-IPPE prediction for ^{138}Pr is given by the dashed curve; however, the measurement is for the metastable state ^{138m}Pr only. In this case, the calculation was renormalized to the data (solid curve), reproducing the shape of the measured excitation function very well. In the case of ^{136}Pr and ^{137}Pr, the measurements show a somewhat lower threshold than the theoretical predictions, nevertheless, the overall agreement is still considered to be satisfactory.

4.1.2 Production yields for ^{139}Pr and ^{140}Nd through the ^{141}Pr + p reaction

In order to calculate the indirectly produced yield of ^{139}Pr via precursor decay, one should in fact consider three branches of decay [19]:

1. ^{139m}Nd→^{139}Pr (88.2%),
2. ^{139m}Nd→^{139g}Nd→^{139}Pr (11.8%),
3. ^{139g}Nd→^{139}Pr (100%).

As will be seen later, the first branch is by far the most dominant, therefore one should consider the growth and decay of ^{139}Pr via this branch in particular. Let $t = 0$ denote the time when an isolated quantity of pure ^{139m}Nd starts to decay. The growth and decay curve of ^{139}Pr formed via branch (1) is shown in Fig. 4.4 (where $A_d(t)$ denotes the activity of the daughter ^{139}Pr at time t and $A_m(0)$ denotes the activity of the mother radionuclide ^{139m}Nd at time $t = 0$). The relevant mathematical equations are derived in Appendix C. The curve reaches a maximum at $t = 6.3$ h; thus, in practice, one would expect the ^{139}Pr activity to reach a maximum after a similar waiting time. At $t = 4.3$ h, the curve reaches a value of 90% of the maximum and only at times larger than $t = 10.8$ h does it fall below 90%. This is very convenient, as it indicates that there is an interval of several hours during which the second chemical separation can be performed. (Obviously, one would still endeavor to keep the actual procedure as short as possible within this time interval.)

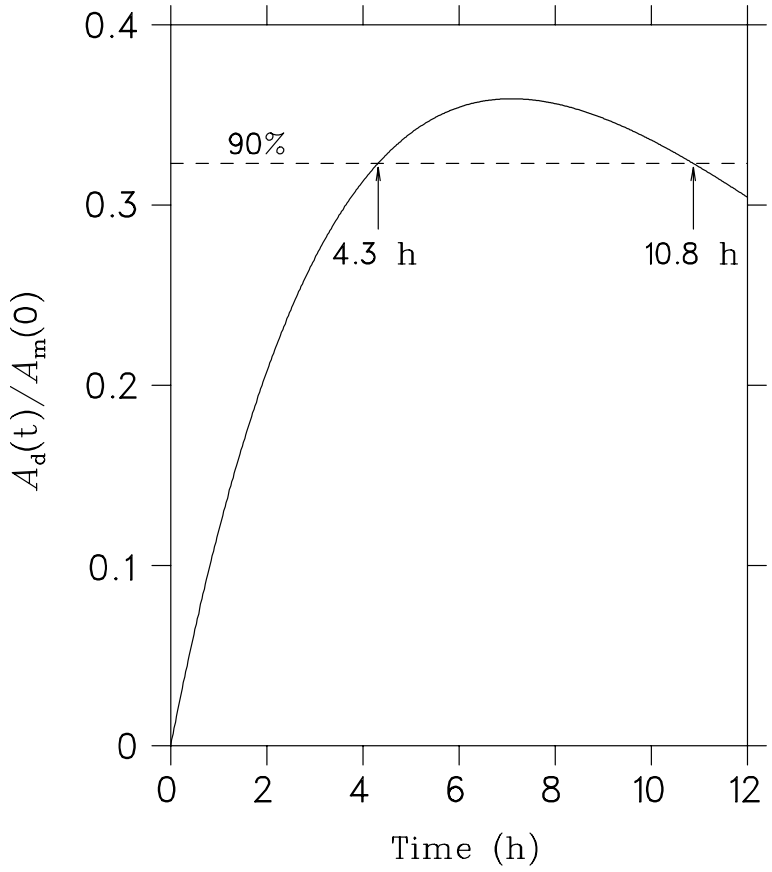

Figure 4.4: Growth and decay of ^{139}Pr formed in the decay of ^{139m}Nd via its most dominant branch, ^{139m}Nd→^{139}Pr (88%). A_d and A_m denote daughter and mother activities, respectively (see text).

In order to compare the direct ^{nat}Ce + p and indirect ^{141}Pr + p production routes of ^{139}Pr in a consistent manner, one should compare the ^{139}Pr yield of a desired radionuclidic purity for similar, practical irradiation conditions (*e.g.* the same realistic bombardment time and beam current). For this purpose, a FORTRAN code was written which follows

the growth and decay of all the Pr radionuclides via their Nd precursors on a time axis. (See Appendices C and D for the derivation of the mathematical expressions.)

Variable parameters were provided for the bombardment, waiting and processing times. For any given scenario, the code calculates the yield and radionuclidic purity based on the excitation function data, the results of which can be directly compared. In the remainder of this chapter, the conditions listed in Table 4.3 have been adopted throughout. These are values which we consider to be typical for a routine ^{139}Pr production run. A bombardment time of 5 hours approaches one half-life of the mother radionuclide ^{139m}Nd ($T_{1/2} = 5.50$ h).

Table 4.3: Production conditions used for purposes of comparison of the denoted production routes

Production Step	Duration (hours)	
	Indirect route via ^{141}Pr + p	Direct route via ^{140}Ce + p
Bombardment time	5.0	5.0
Waiting time 1	0.5	0.5
Chemical separation 1[a]	0.5	0.5
Waiting time 2	variable	0.5
Chemical separation 2[b]	0.5	—
Waiting time 3	0.5	—

[a]Nd from Pr target matrix in the case of the indirect route.
[b]Pr from Nd eluate in the case of the indirect route.

Waiting time 1 is the time interval between EOB and the start of the first chemical separation (the direct ^{nat}Ce + p route only has this one chemical separation) and includes tasks such as removal of the target from the beamline, transport to a reception hot cell, decapsulation and transfer of the irradiated target material to a processing hot cell. The actual chemical separation procedures are assumed to take half-an-hour. In the case of the indirect ^{141}Pr + p route, waiting time 2 is the period allowed for the accumulation of ^{139}Pr from decay of its precursors. In the case of the direct ^{nat}Ce + p route, waiting time 2 is a time allowed from the end of the chemical separation until the radionuclidic assay is done of a sample taken from the final solution. Waiting time 3 is similar for the indirect ^{141}Pr + p route and also allows some time for the decay of very short-lived radiocontaminants.

Assuming the production conditions listed in Table 4.3, calculations were performed using a value of 6.3 h for waiting time 2 (*i.e.* the time at which a maximum of the growth and decay curve shown in Fig. 4.4 was obtained) while varying the incident proton energy between 30 and 100 MeV. Furthermore, it was assumed that the exit energy is 10 MeV, *i.e.* below the effective thresholds for ^{139m}Nd and ^{140}Nd production. The yield and radionuclidic purity of the ^{139}Pr formed under these conditions are plotted in Fig. 4.5 as a function of the incident

energy. (Note that radiochemical losses were assumed to be negligible.) Below 49 MeV the radionuclidic purity is close to 100%, while above 49 MeV it progressively decreases to a value of about 94.5% at 100 MeV.

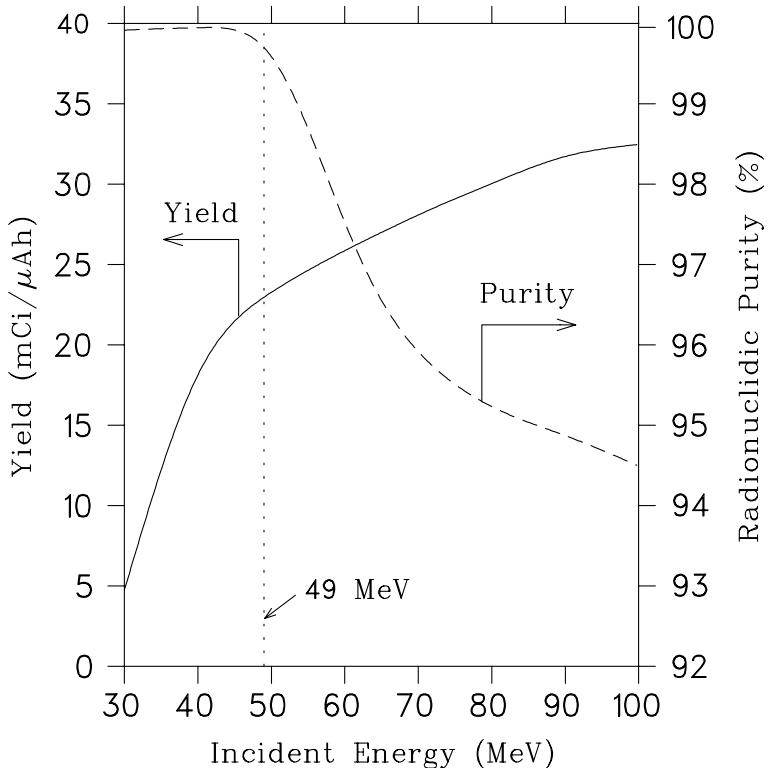

Figure 4.5: Production yield (solid curve) and radionuclidic purity (dashed curve) of ^{139}Pr formed via precursor decay in the proton bombardment of ^{141}Pr, plotted as a function of the incident proton energy. Note that the production conditions are those listed in Table 4.3 (see text).

It should be pointed out that none of the co-produced Pr radiocontaminants has a half-life exceeding that of ^{139}Pr, thus the radionuclidic purity will increase with time. The most dominant contaminant, ^{137}Pr ($T_{1/2}$ = 1.28 h), can be reduced by lowering the incident energy or by increasing the waiting time after the second separation (*i.e.* waiting time 3). We opted for a relatively high purity product at iThemba LABS, adopting an energy window of 49 $\rightarrow$ 10 MeV. The expected yield for this energy window is 22.9 mCi/μAh (847 MBq/μAh), while for 100 $\rightarrow$ 10 MeV it is 32.5 mCi/μAh (1202 MBq/μAh). (Note that these yields should be interpreted in the light of Table 4.3 with the units μAh strictly that of the accumulated charge obtained with a constant beam current.)

Using the production conditions of Table 4.3 in conjunction with an incident proton energy of 49 MeV, calculations were performed in which the waiting time 2 was varied between 4 and 10 hours. The yield and radionuclidic purity obtained for ^{139}Pr are plotted in Fig. 4.6 as a function of this waiting time. As expected from the growth and decay curve (Fig. 4.4), a maximum yield is obtained after a waiting time of 6.3 hours but the shape of

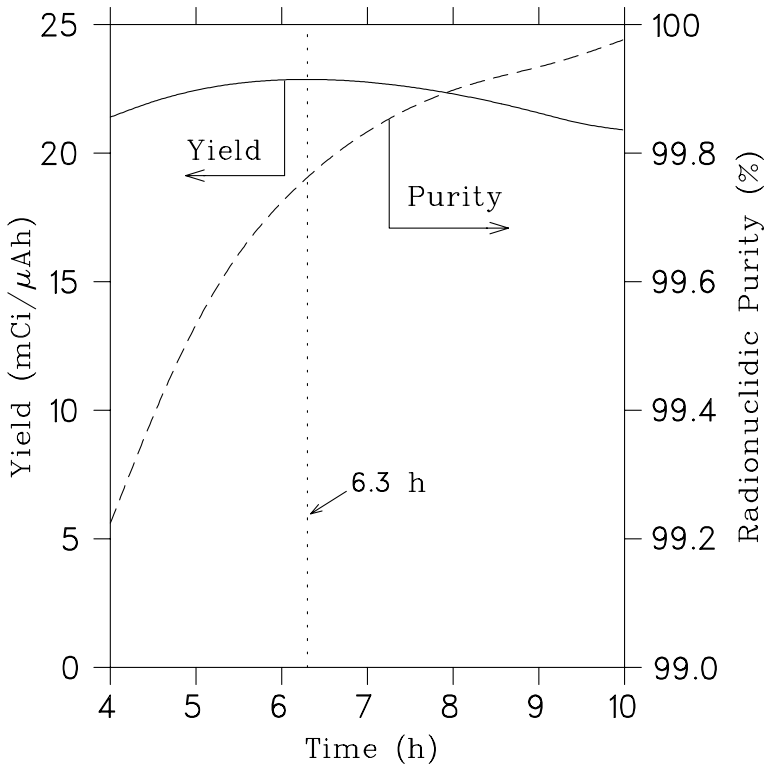

Figure 4.6: Production yield (solid curve) and radionuclidic purity (dashed curve) of ^{139}Pr formed via precursor decay in the proton bombardment of ^{141}Pr, plotted as a function of the waiting time between the two radiochemical separations. Note that the production conditions are those listed in Table 4.3 and a production energy window of 49 → 10 MeV.

the yield curve is quite flat, peaking at 22.9 mCi/μAh (847 MBq/μAh) and remains above 20.9 mCi/μAh (773 MBq/μAh) over the entire time period considered. The maximum value of 22.9 mCi/μAh (847 MBq/μAh) could also have been expressed as 114.5 mCi/μA (4236 MBq/μA) as the bombardment time according to Table 4.1 is 5 hours.

It is interesting to observe the contributions of all the Pr radionuclides formed via precursor decay to the total precursor-produced Pr activity at the end of the process as summarized in Table 4.3. These values are presented in Table 4.4 for a production energy window of 49 → 10 MeV. The ^{139}Pr contribution is 99.79% of the total Pr activity, of which 95.93% is formed via the ^{139m}Nd→^{139}Pr branch.

The question remains whether a useful quantity of ^{140}Nd can be simultaneously produced. The ^{140}Nd yield obtained under the production conditions outlined in Table 4.3 is shown in Fig. 4.7 as a function of the incident energy. In this case, we assumed the radionuclidic assay to be performed 30 minutes after separating the Nd from the Pr target matrix, *i.e.* after completing chemical separation 1 of Table 4.3. At 49 MeV the yield is 9.45 mCi/μAh (350 MBq/μAh) and at 100 MeV it is 12.9 mCi/μAh (477 MBq/μAh). These production rates are high, especially if one considers the relatively long half-life of this radionuclide.

With a beam intensity of 85 μA, which is a typical beam current used for routine ra-

Table 4.4: Contributions to the total Pr activity obtained via Nd precursor decay in the proton bombardment of ^{141}Pr

Contributing process	Percentage of total Pr activity
^{140}Pr via ^{140}Nd	0.01%
^{139}Pr via ^{139m}Nd (direct)	95.93%
^{139}Pr via ^{139m}Nd$\rightarrow^{139g}$Nd	0.02%
^{139}Pr via ^{139g}Nd	3.82%
^{138g}Pr via ^{138}Nd	0.0%
^{137g}Pr via ^{137}Nd	0.22%
^{136}Pr via ^{136}Nd	0.0%
^{135}Pr via ^{135g}Nd	0.0%

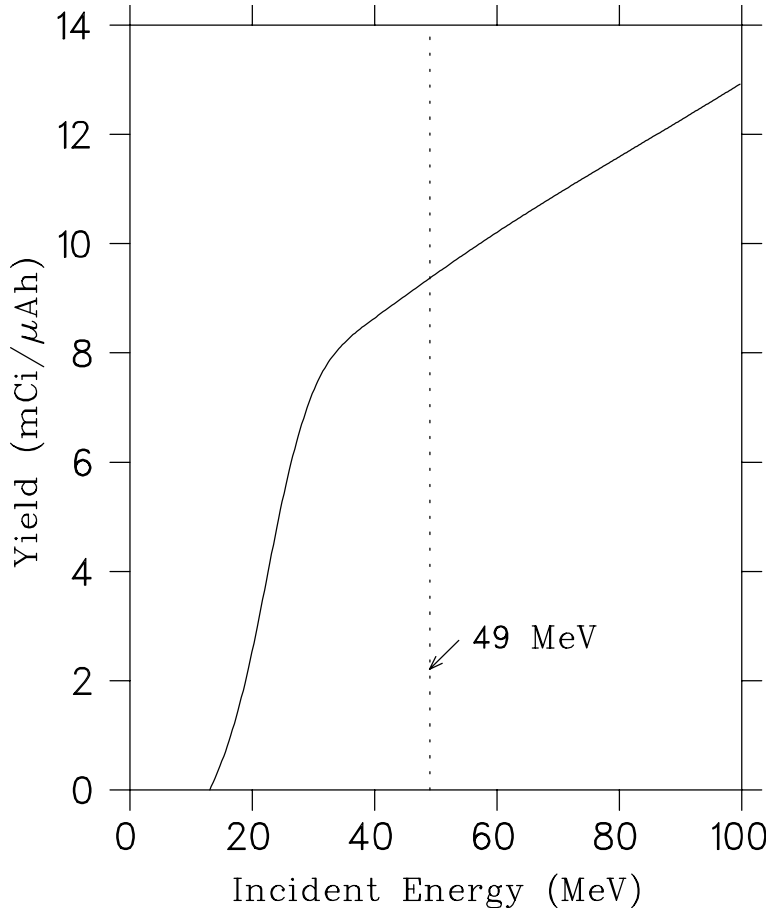

Figure 4.7: Production yield of ^{140}Nd (solid curve) directly produced in the proton bombardment of ^{141}Pr, plotted as a function of the incident proton energy. Note that the production conditions are those listed in Table 4.3.

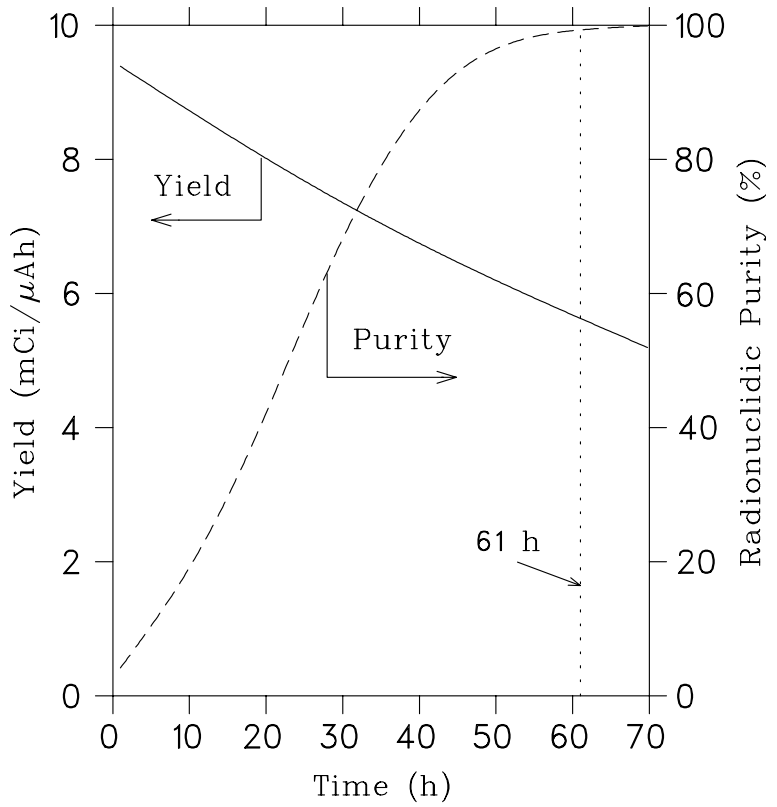

Figure 4.8: Production yield (solid curve) and radionuclidic purity (dashed curve) of ^{140}Nd directly produced in the proton bombardment of ^{141}Pr, plotted as a function of the waiting time after completion of the first radiochemical separation. Note that the production conditions are those listed in Table 4.3. The energy window is 49 → 10 MeV (see text).

dionuclide productions at iThemba LABS, several curies of ^{140}Nd can be produced per production run. Of course, the radionuclidic purity should also be considered. With a 49 → 10 MeV energy window, the main contaminants are ^{138}Nd and ^{139m}Nd, both having half-lives longer than 5 hours. The ^{140}Nd yield and corresponding radionuclidic purity for this energy window is shown in Fig. 4.8 as a function of the time after completion of the first radiochemical separation. As can be seen from the figure, the radionuclidic purity is initially very low ($< 10\%$). However, it improves steadily with time. After a waiting period of 61 hours, the purity is $> 99\%$. The yield after 61 hours is 5.63 mCi/μAh (208 MBq/μAh), still sufficiently high to produce curie quantities of high-purity ^{140}Nd.

Note that very useful quantities of ^{139}Pr and ^{140}Nd can also be simultaneously produced with certain commercial medical cyclotrons. For example, utilizing an energy window of 30 → 10 MeV, the conditions of Table 4.3 and a waiting time of 6.3 hours between the two chemical separations, 4.62 mCi/μAh (171 MBq/μAh) of ^{139}Pr is expected with a radionuclidic purity of 99.95%. The corresponding ^{140}Nd yield is 7.43 mCi/μAh (275 MBq/μAh) 30 minutes after the first chemical separation, with a radionuclidic purity of 25.5%. In this case, a waiting time of 46 h is required to achieve a purity $> 99\%$, at which point in time the yield will be 5.03 mCi/μAh (186 MBq/μAh). For the energy window of 18 → 10 MeV,

no ^{139}Pr is produced as the incident energy is below the reaction threshold, however, the ^{140}Nd yield is 1.51 mCi/μAh (56 MBq/μAh) with a purity of 100%, 30 minutes after the end of the first chemical separation.

4.1.3 Production yields for ^{139}Pr through the ^{140}Ce + p reaction

The yield and radionuclidic purity of the ^{139}Pr produced directly in the irradiation of an enriched $^{140}CeO_2$ target is shown in Fig. 4.9 as a function of the incident proton energy. As before, the production conditions are those outlined in Table 4.3. An exit energy from the target of 12 MeV (near the threshold of the (p,2n) reaction) was assumed. The excitation function data of Zeisler and Becker [9] were used for these calculations. Below about 24 MeV the radionuclidic purity is very close to 100%, while above 24 MeV it rapidly decreases to a value below 90% at 32 MeV. This is mainly due to the radiocontaminant ^{138m}Pr ($T_{1/2}$ = 2.12 h). For the 24 → 12 MeV energy window a yield of 28.3 mCi/μAh (1047 MBq/μAh) is obtained with a radionuclidic purity of 99.93%. This yield for radionuclidically pure ^{139}Pr is 24% higher than what can be obtained with a Pr target. However, the higher yield comes at the cost of having to use an enriched target.

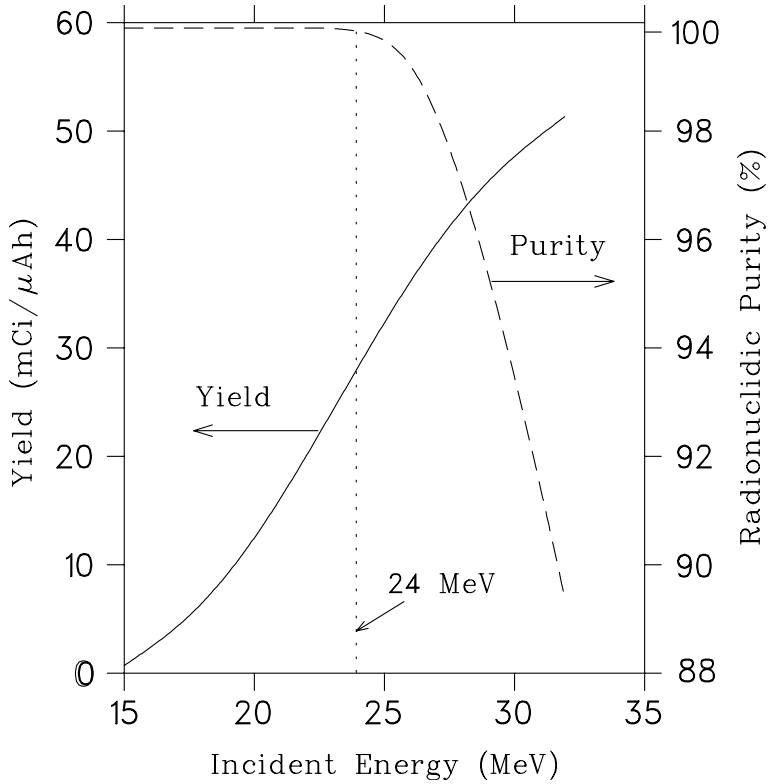

Figure 4.9: Production yield (solid curve) and radionuclidic purity (dashed curve) of ^{139}Pr directly produced in the proton bombardment of an enriched $^{140}CeO_2$ target, plotted as a function of the incident proton energy. Note that the production conditions are those listed in Table 4.3 (see text).

Since the natural abundance of ^{140}Ce is quite high (88.48%), economically it would make

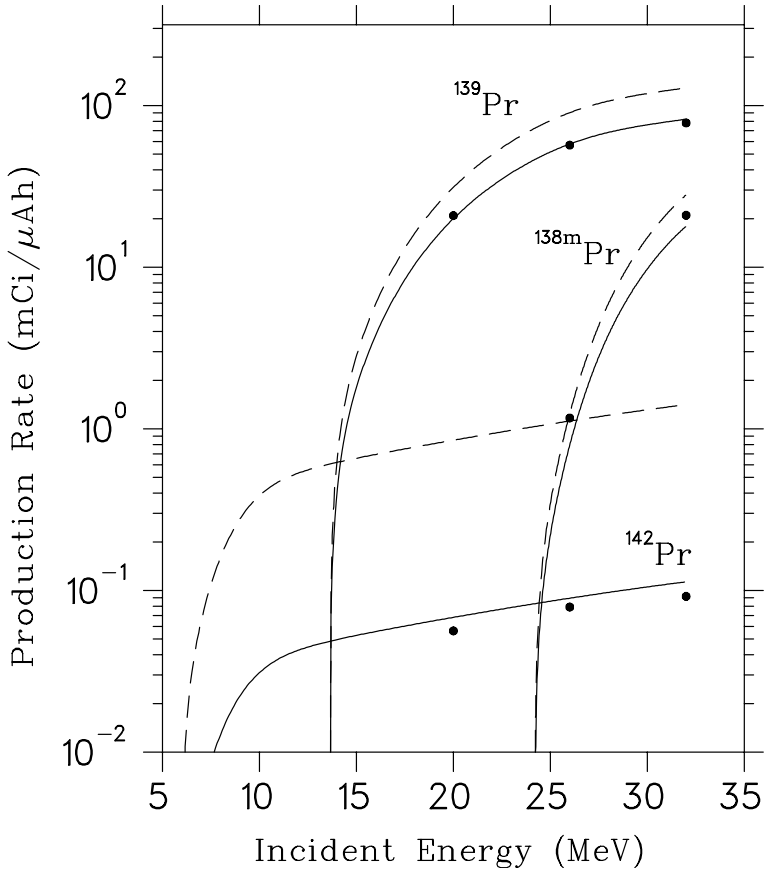

Figure 4.10: Production rates of some Pr radionuclides directly produced in the proton bombardment of Ce. The dashed curves represent enriched metallic targets, *i.e.* ^{140}Ce + p in the case of ^{139}Pr and ^{138m}Pr, and ^{142}Ce + p in the case of ^{142}Pr. The solid curves represent the same information but re-normalized for a natural CeO_2 target (see text). The solid symbols are the experimental values of this work, also re-normalized for a natural CeO_2 target.

sense if ^{nat}Ce can be used as target material instead of enriched ^{140}Ce. The main concern is the production of the relatively long-lived radiocontaminant ^{142}Pr ($T_{1/2}$ = 19.13 h) via the (p,n) reaction on ^{142}Ce. In Fig. 4.10, the calculated thick-target production rate curves of ^{138m}Pr and ^{139}Pr (based on the measured cross sections of Zeisler and Becker [9]) as well as of ^{142}Pr (based on an ALICE-IPPE calculation) for ^{nat}Ce + p are compared with the measured values of this study. Note that this study distinguishes between "production rate" and "yield" in that the former precludes radioactive decay. The numerical values pertaining to enriched targets are presented in Table 4.5.

In the case of ^{139}Pr the agreement is excellent. Slightly higher values were measured for ^{138m}Pr than Zeisler and Becker, and obtained slightly lower values than the theoretical predictions for ^{142}Pr. With an energy window of 24 → 12 MeV, a yield of 25.0 mCi/μAh (925 MBq/μAh) is expected on a $^{nat}CeO_2$ target. The contribution of the contaminant ^{142}Pr is negligible at all three incident energies (20, 26 and 32 MeV). Thus natural Ce targets are indeed suitable for ^{139}Pr production with protons above 20 MeV. One should,

Table 4.5: Measured production rates of some Pr radionuclides directly produced in the proton bombardment of Ce targets as indicated

Isotope	Target	Energy	Production rate (mCi/μAh)	
		(MeV)	This work[a]	Becker [5]
^{139}Pr	^{140}Ce	20	32.6 ± 2.29	31.26
		26	88.9 ± 6.23	90.88
		32	122.0 ± 8.55	128.28
^{138m}Pr	^{140}Ce	26	1.82 ± 0.13	1.17
		32	32.8 ± 2.30	28.20
^{142}Pr	^{142}Ce	20	0.701 ± 0.059	—
		26	0.985 ± 0.080	—
		32	1.15 ± 0.092	—

[a]The error values listed include a systematic uncertainty, which is estimated to be 7% (see text).

however, take some care below 18 MeV, where the ^{142}Pr contribution becomes significant as the threshold of the ^{139}Pr excitation function is approached.

4.2 Results relevant to ^{139}Ce production

The measured cross sections for the production of various Ce radionuclides in ^{141}Pr + p are presented in Table 4.6. The data for the cumulative production of ^{139}Ce are compared with previous literature data in Fig. 4.11. The agreement with the values of Hilgers *et al.* is satisfactory in the overlap energy region (*i.e.* below 45 MeV). For the purpose of thick-target yield calculations, a polynomial function was fitted through the data by means of the non-linear regression code TABLECURVE [44] and integrated numerically. This polynomial reproduces the data reliably, as shown by the dashed curve in Fig. 4.11. The theoretical prediction (by means of the code ALICE-IPPE) is also in excellent agreement with the measured data for this radioisotope.

It is interesting to look at the individual contributions to the theoretical cumulative excitation function from the relevant reaction channels: The dot-dashed curve in Fig. 4.11 is the contribution from the reaction ^{141}Pr(p,3n)^{139}Nd$\rightarrow^{139}$Pr$\rightarrow^{139}$Ce; the long-dashed curve is the contribution from the inclusive reaction ^{141}Pr(p,x)^{139}Pr$\rightarrow^{139}$Ce; and the dotted curve is the directly produced contribution from the reaction ^{141}Pr(p,x)^{139}Ce. Clearly, the (p,3n) re-

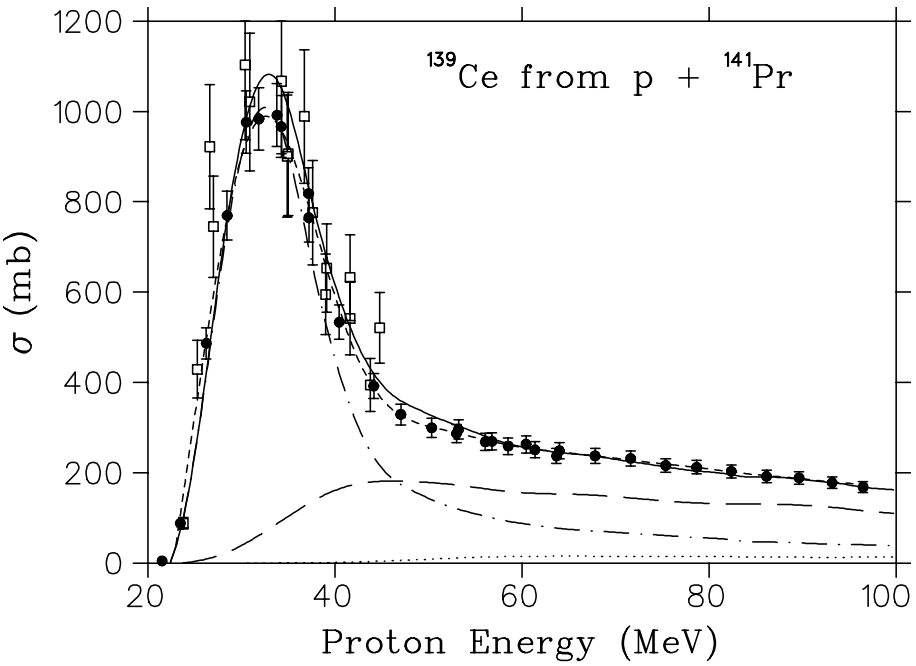

Figure 4.11: Excitation function for the cumulative production of ^{139}Ce in the irradiation of ^{141}Pr with protons. The solid circles are the experimental cross sections of this work. The open squares are the measurements of Hilgers *et al.* [10]. The error bars represent the total experimental uncertainties, shown only where these exceed the symbol size (see text). The short-dashed curve is a polynomial fit used for numerical integration in order to obtain the thick-target production rate curve for this radionuclide. The solid curve is a theoretical prediction by means of the code ALICE-IPPE (see text). The dot-dashed curve is the ALICE-IPPE contribution from the reaction ^{141}Pr(p,3n)^{139}Nd→^{139}Pr→^{139}Ce. The long-dashed curve is the ALICE-IPPE contribution from the reaction ^{141}Pr(p,x)^{139}Pr→^{139}Ce. The dotted curve is the directly produced contribution from the reaction ^{141}Pr(p,x)^{139}Ce, as calculated using the ALICE-IPPE code.

action is dominant in the peak region towards lower energies while the ^{141}Pr(p,x)^{139}Pr→^{139}Ce reaction becomes progressively more important in the tail region towards higher energies. The directly produced component is almost negligible.

Since the half-lives of the other co-produced Ce radioisotopes are much shorter than the half-life of ^{139}Ce (see Table 2.1), they do not affect the radionuclidic purity of the final product. A week after EOB, for example, the contaminants would have decayed to negligible levels. It is nevertheless interesting to compare the excitation functions of these other observed Ce radioisotopes with the ALICE-IPPE predictions, shown in Fig. 4.12. As ^{137m}Ce has no precursors, the excitation function is for its direct production only. Consequently, these cross sections are relatively small. The agreement with the theoretical prediction is satisfactory from threshold up to about 75 MeV. Above 75 MeV, the prediction show a curious increasing trend up to a maximum at about 94 MeV, over-predicting the measurements. It should, however, be stressed that the ALICE-IPPE code neglects final-state spin, thus the absence of the ground-state contribution in the measured data may be responsible for the deficit. Unfortunately, data for ^{137g}Ce could not be extracted

Table 4.6: Measured cross sections for the production of the denoted cerium radionuclides in the irradiation of ^{141}Pr with protons

Energy	Cross section[a] (mb)				
(MeV)	^{132}Ce	^{133m}Ce	^{135}Ce	^{137m}Ce	^{139}Ce
20.9 ± 1.3	—	—	—	—	4.61 ± 1.39
23.5 ± 1.1	—	—	—	—	78.8 ± 7.0
26.2 ± 0.9	—	—	—	5.31 ± 1.19	486.5 ± 34.3
28.5 ± 0.9	—	—	—	7.08 ± 1.16	769.7 ± 54.1
30.5 ± 0.8	—	—	—	7.91 ± 0.92	976.4 ± 69.1
31.9 ± 0.7	—	—	—	6.72 ± 0.87	983.5 ± 69.0
33.8 ± 0.7	—	—	—	5.34 ± 0.74	991.8 ± 69.6
34.3 ± 0.6	—	—	—	6.15 ± 0.75	966.5 ± 68.3
37.1 ± 1.6	—	—	—	4.37 ± 0.63	818.0 ± 57.4
37.2 ± 0.5	—	—	0.82 ± 0.24	4.78 ± 0.60	764.8 ± 54.0
40.5 ± 1.4	—	—	5.26 ± 0.46	4.06 ± 0.59	533.4 ± 37.7
44.1 ± 1.3	—	—	15.5 ± 1.1	3.29 ± 0.51	391.8 ± 27.7
47.0 ± 1.2	—	—	23.2 ± 1.7	3.63 ± 0.57	328.9 ± 23.3
50.3 ± 1.1	—	—	28.5 ± 2.0	3.43 ± 0.55	299.4 ± 21.2
53.0 ± 1.0	—	—	27.9 ± 2.0	3.40 ± 0.55	286.6 ± 20.3
53.2 ± 2.5	—	—	27.9 ± 2.0	3.51 ± 0.54	295.5 ± 21.4
56.1 ± 1.0	—	—	23.3 ± 1.7	4.34 ± 0.58	268.3 ± 19.0
56.8 ± 2.3	—	—	22.8 ± 1.7	4.87 ± 0.63	269.4 ± 19.5
58.5 ± 0.9	—	—	20.2 ± 1.5	5.29 ± 0.64	258.8 ± 18.3
60.4 ± 2.1	—	—	17.9 ± 1.3	6.25 ± 0.66	263.0 ± 18.9
61.4 ± 0.7	—	—	16.7 ± 1.2	6.94 ± 0.71	250.6 ± 17.8
63.7 ± 0.6	—	2.18 ± 0.41	14.5 ± 1.1	7.51 ± 0.74	237.1 ± 16.8
64.0 ± 1.9	—	4.21 ± 0.53	15.1 ± 1.1	7.38 ± 0.73	248.7 ± 17.9
67.8 ± 1.7	—	8.71 ± 0.76	15.8 ± 1.2	9.78 ± 0.86	237.3 ± 17.0
71.6 ± 1.6	0.64 ± 0.16	16.6 ± 1.3	30.9 ± 2.2	11.1 ± 0.9	231.6 ± 16.6
75.4 ± 1.5	3.16 ± 0.27	23.0 ± 1.7	63.4 ± 4.5	11.0 ± 0.9	215.8 ± 15.5
78.7 ± 1.3	7.89 ± 0.58	22.5 ± 1.7	110.3 ± 7.8	12.7 ± 1.1	212.1 ± 15.2
82.4 ± 1.2	15.1 ± 1.0	21.7 ± 1.8	157.3 ± 11.1	13.3 ± 1.1	203.1 ± 14.5
86.2 ± 1.1	22.4 ± 1.6	17.2 ± 1.4	188.2 ± 13.2	14.0 ± 1.2	191.9 ± 13.7
89.6 ± 0.9	25.5 ± 1.8	14.9 ± 1.2	198.0 ± 13.9	14.1 ± 1.2	188.5 ± 13.5
93.2 ± 0.8	27.1 ± 1.9	13.2 ± 1.1	199.6 ± 14.0	15.2 ± 1.3	178.0 ± 12.8
96.5 ± 0.7	25.7 ± 1.8	12.4 ± 1.0	187.5 ± 13.1	14.8 ± 1.3	168.2 ± 12.1

[a]The error values listed include a 7% estimated systematic uncertainty (see text).

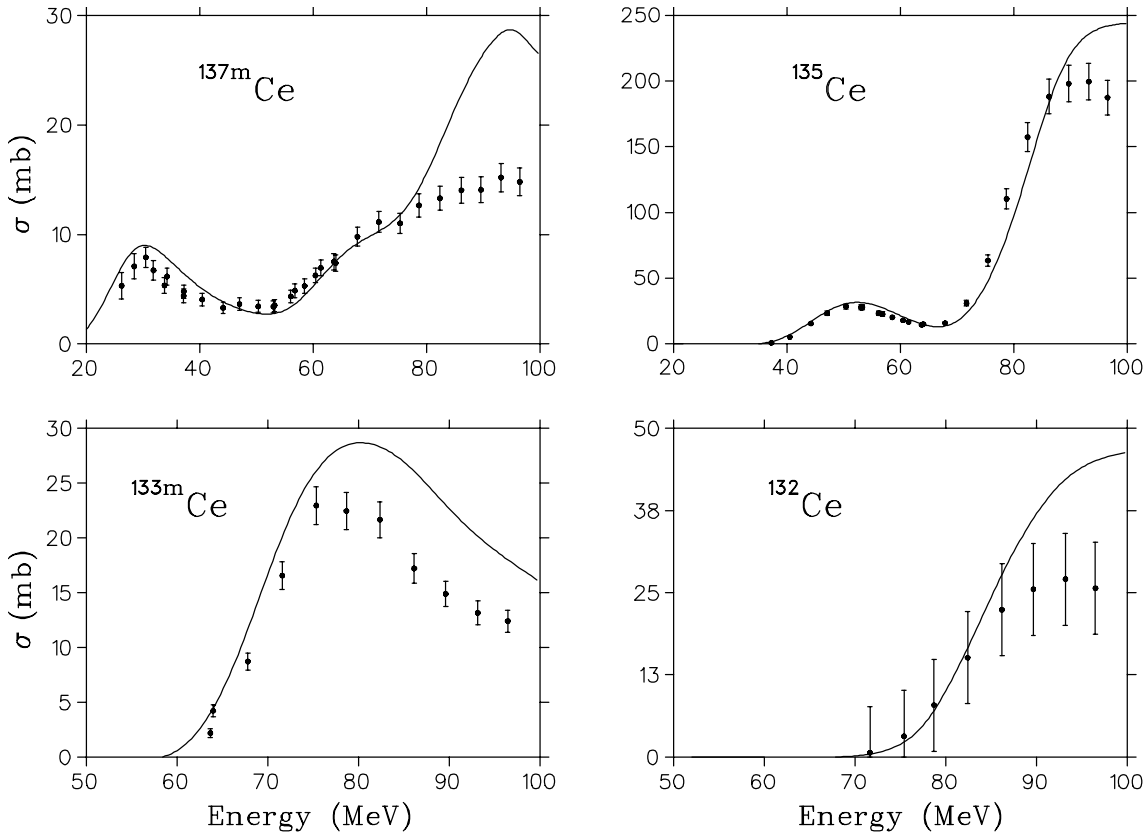

Figure 4.12: Excitation functions for the production of the denoted Ce radioisotopes in the irradiation of ^{141}Pr with protons. The solid symbols are the experimental values of this work. The error bars represent the total experimental uncertainties, shown only where these exceed the symbol size. The solid curves are theoretical predictions by means of the code ALICE-IPPE (see text).

from the measured γ-ray spectra for two reasons: Firstly, all the γ-rays emitted during ^{137g}Ce decay have very weak intensities and, secondly, it is continuously fed from the decay of the much longer-lived ^{137m}Ce, precluding sufficient statistics when this metastable contribution is subtracted. Also note that cumulative cross sections could not be extracted for ^{137}Ce as the ground state has a shorter half-life than the metastable state. In the case of ^{133}Ce, the shorter-lived ground state could similarly not be extracted with meaningful statistics, thus only data for the direct production of the longer-lived ^{133m}Ce is presented.

The excitation functions for ^{135}Ce and ^{132}Ce are for their cumulative production. In these cases, the ALICE-IPPE predictions are reasonable but show a measure of over-prediction at the highest energies. The peak between 40 and 60 MeV on the ^{135}Ce excitation function is from its direct production only, whereafter the precursor decay becomes dominant, leading to the sharp rise towards higher energies (see Fig. 4.12). In the cases of ^{133m}Ce and ^{132}Ce, the contributions from precursor decay are negligible compared to their direct production.

The derived thick-target production rates for ^{139}Ce in ^{141}Pr + p are presented in Table 4.7 and Fig. 4.13. Clearly, useful quantities of this radioisotope can be produced with protons

Table 4.7: Thick-target production rates of ^{139}Ce formed in the irradiation of ^{141}Pr with protons

Energy (MeV)	Thick-target production rate[a] (μCi/μAh)
25.0	4.37
30.0	51.5
35.0	131.8
40.0	200.2
45.0	244.5
50.0	279.4
55.0	312.9
60.0	345.4
65.0	377.6
70.0	410.2
75.0	442.7
80.0	475.1
85.0	506.9
90.0	538.4
95.0	569.4
100.0	599.8

[a]Values calculated from measured excitation function.

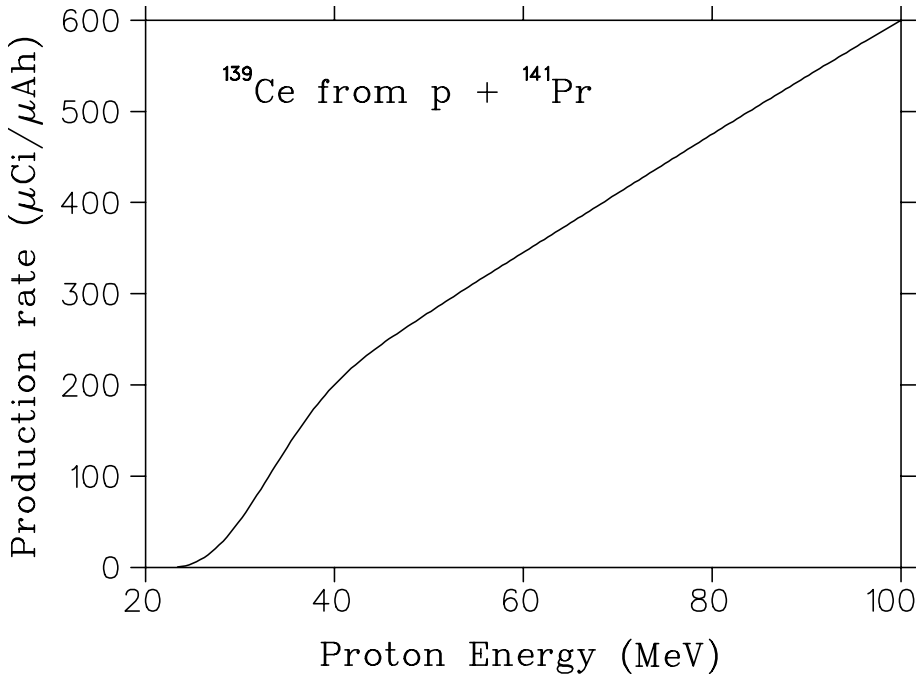

Figure 4.13: Calculated thick-target production rate curve of ^{139}Ce, derived from the experimental excitation function obtained in the irradiation of ^{141}Pr with protons.

of about 30 MeV and higher. About 50 μCi/μAh (1.8 MBq/μAh) is possible with 30 MeV protons, more than 300 μCi/μAh (11.1 MBq/μAh) with 60 MeV protons and 600 μCi/μAh (22.2 MBq/μAh) with 100 MeV protons.

The measured thick-target production rates of ^{139}Ce formed in the irradiation of $^{nat}La_2O_3$ with protons are shown in Fig. 4.14 and listed in Table 4.8. The dashed curve is a function fitted through the data by means of the non-linear regression code TABLECURVE [44], which could be differentiated analytically for purposes of calculating the corresponding excitation function. The solid curve in Fig. 4.14 has been derived for the case where the target is pure metallic ^{nat}La.

Table 4.8: Measured thick-target production rates of ^{139}Ce formed in the irradiation of $^{nat}La_2O_3$ with protons

Energy (MeV)	Thick-target production rate[a] (μCi/μAh)
1.8	$3.8 \times 10^{-3} \pm 3.8 \times 10^{-4}$
3.4	$4.3 \times 10^{-3} \pm 4.3 \times 10^{-4}$
5.2	$9.3 \times 10^{-3} \pm 9.3 \times 10^{-4}$
6.4	$2.4 \times 10^{-1} \pm 2.4 \times 10^{-2}$
7.7	$4.1 \times 10^{-1} \pm 4.1 \times 10^{-2}$
8.8	2.03 ± 0.20
10.1	3.40 ± 0.34
11.2	6.14 ± 0.61
12.4	7.02 ± 0.70
13.4	8.64 ± 0.86
14.5	9.46 ± 0.95
15.6	10.2 ± 1.0
16.7	10.5 ± 1.1
17.7	11.7 ± 1.2
18.8	11.8 ± 1.2

[a]The error values listed include a 10% estimated systematic uncertainty (see text).

The derived excitation function is shown in Fig. 4.15 (solid curve), where it is compared with the data of Wing and Huizenga [45]. The values of Wing and Huizenga appears to be systematically shifted to higher energies, by about 1 MeV; however, the shape appears to agree well with the present results. In order to point this out, a shifted excitation function is also shown in Fig. 4.15, presented by the dotted curve. The dashed curve is an ALICE-IPPE prediction. It is interesting to note that the theoretical excitation function has a maximum very close to the experimentally derived excitation function of this work and does not show an energy shift. It does, however, have a slightly narrower distribution. Although it has been reported that at energies above 20 MeV the (p,n) reaction in this mass

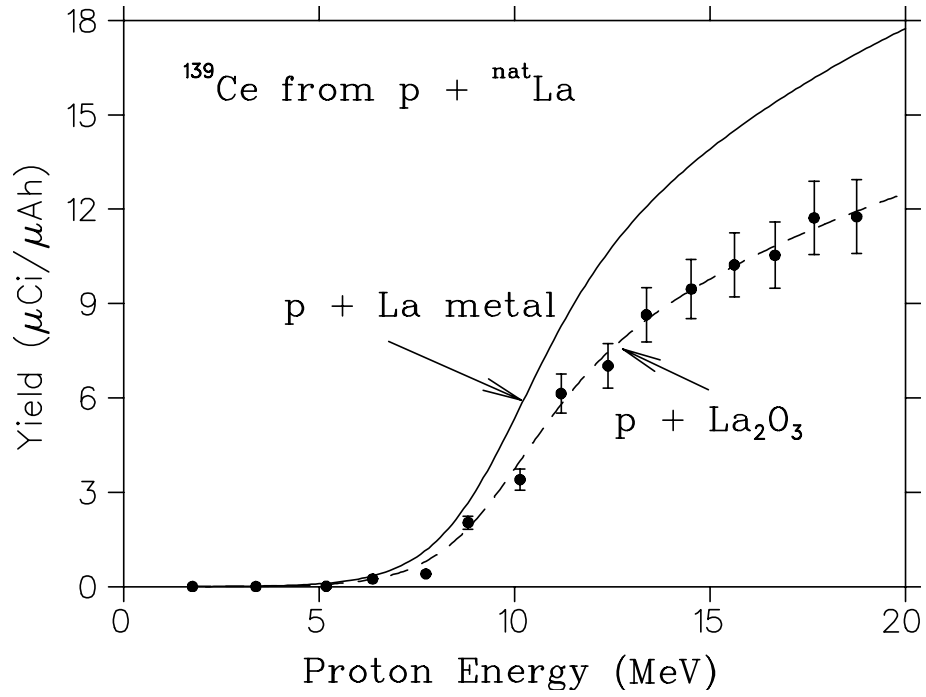

Figure 4.14: Thick-target production rates of ^{139}Ce formed in the irradiation of ^{nat}La and $^{nat}La_2O_3$ with protons. The solid circles are the experimental values of this work, while the dashed curve is a fitted function through these values for the purpose of performing numerical calculations (see text). The solid curve is a calculated prediction for the reaction of protons on a pure metallic La target.

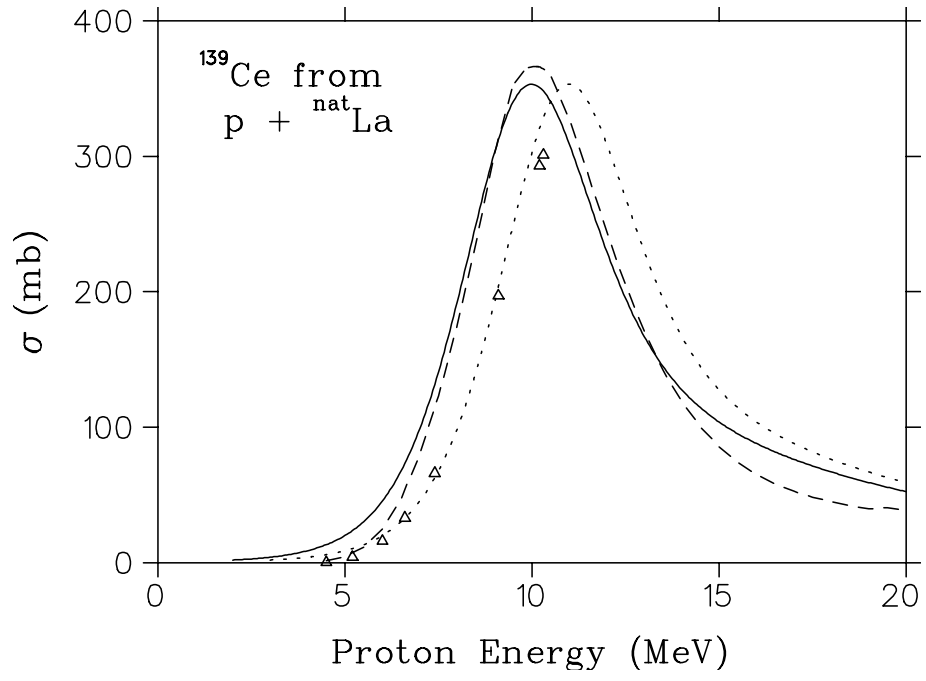

Figure 4.15: Excitation function of ^{139}Ce formed in the reaction of protons with ^{nat}La. The solid curve was derived from the measured thick-target production rate data (see Fig.4.14). The dashed curve is a theoretical prediction by means of the code ALICE-IPPE. The triangles are measured data by Wing and Huizenga [45], while the dotted curve displays the same information as the solid curve but shifted to higher energies in order to overlap with the measured data for the purpose of comparison (see text).

Table 4.9: Cross sections and thick-target production rates of ^{139}Ce for ^{nat}La + p as deduced from the data measured using activated La_2O_3 targets

Energy (MeV)	Cross section (mb)	Thick-target production rate[a] (μCi/μAh)
2.0	1.89	—
3.0	3.95	—
4.0	8.77	3.2×10^{-2}
5.0	20.0	8.8×10^{-2}
6.0	45.5	2.4×10^{-1}
7.0	99.0	6.1×10^{-1}
8.0	192.6	1.5
9.0	303.0	3.0
10.0	353.2	5.4
11.0	308.7	7.8
12.0	229.5	9.9
13.0	166.9	11.6
14.0	127.7	12.9
15.0	103.8	13.9
16.0	87.9	14.8
17.0	76.2	15.7
18.0	66.9	16.4
19.0	59.1	17.1
20.0	52.4	17.8

[a]An estimated 10% systematic uncertainty applies.

region is not described as well by ALICE-IPPE calculations as the (p,xn) reactions [46], the agreement found in this work is acceptable.

The derived cross sections and experimental thick-target production rates for ^{139}Ce formed in ^{nat}La + p (*i.e.* converted for the case of a pure natural La target) are presented in Table 4.9.

One of the objectives of the present study was to investigate whether it would be meaningful to use a Pr/La tandem target (Pr in a high-energy slot and La in a low-energy slot) to optimize the ^{139}Ce yield. At iThemba LABS, for example, the ^{141}Pr + p route offers a production rate in excess of 300 μCi/μAh with the 66 MeV proton beam which is routinely available for the production of radioisotopes. By including a La_2O_3 target in the low-energy slot, only an additional 12 μCi/μAh will be gained. This is too little to justify the effort to process a second target. With smaller cyclotrons, however, only the La + p production route may be suitable (when the beam energy is below 24 MeV). In this case, the production of small to moderate quantities of ^{139}Ce is feasible.

Chapter 5

Nuclear Data: Conclusions

5.1 Production of ^{139}Pr

The optimum energy windows for the production of ^{139}Pr with a high radionuclidic purity were determined for the proton bombardment of Pr and Ce targets under similar bombardment conditions. Natural targets are suitable in both cases; however, it was assumed that in the case of ^{nat}Ce + p, a CeO_2 target is more suitable due to the extremely reactive nature of metallic Ce. Assuming the specific bombardment conditions adopted in this study and assuming negligible radiochemical losses, a ^{139}Pr yield of 22.9 mCi/μAh (847 MBq/μAh) is expected for ^{141}Pr + p in the energy window 49 $\rightarrow$ 10 MeV.

Similarly, for $^{141}CeO_2$ + p, a yield of 25.0 mCi/μAh (925 MBq/μAh) is expected in the energy window 24 $\rightarrow$ 12 MeV. Thus the expected ^{139}Pr yield from $^{nat}CeO_2$ + p is marginally higher. In practice, however, the yields from the two production routes can be considered to be quite similar and other factors may affect the choice. The $^{nat}CeO_2$ + p production route only requires one chemical separation step and the optimum production energy window is suitable for a 30 MeV commercial cyclotron. On the other hand, the ^{141}Pr + p production route offers the possibility to simultaneously produce useful quantities of ^{140}Nd.

Referring again to the chart of the nuclides shown in Fig. 1.1, it is astonishing that ^{139}Pr of such a high purity (approaching 100%) can be produced via the decay of its precursor ^{139}Nd. At the recommended incident energy of 49 MeV, for example, many reaction channels are open. It just so happens that several of the co-produced Pr radionuclides have relatively short half-lives and ^{138m}Pr is not populated in the decay of ^{138}Nd, thus Mother Nature is unusually friendly in this case. It also deserves mention that this surprising result could not have been anticipated by consulting the chart of the nuclides and studying a complete set of excitation functions, without further calculation of the yields of all the relevant Pr radionuclides according to the time evolution of their growth and decay via precursor decay.

5.2 Production of ^{139}Ce

From a nuclear data point of view, the results indicate that Pr is the target material of choice for the production of ^{139}Ce, if the available proton energy is high enough to exploit the ^{141}Pr(p,3n)$^{m+g}$Nd$\rightarrow^{139}$Pr$\rightarrow^{139}$Ce process, which is the dominant channel leading to ^{139}Ce formation in ^{141}Pr + p (about 30 MeV or higher). The reaction ^{139}La(p,n)^{139}Ce is suitable to produce small to moderate quantities using protons of lower energy, e.g. at smaller medical cyclotrons such as found at many PET facilities. The excitation functions of the Ce radionuclides presented in this work are well reproduced by GDH model predictions, however, in several cases the theoretical calculations over-predict the measured data at the highest energies.

Pr/La tandem targetry is not meaningful if the incident proton energy is sufficiently high (it e.g. the 66 MeV beam at iThemba LABS) as the La + p reaction does not offer a significant increase in the total ^{139}Ce yield. The La + p production route, however, may be important for smaller commercial cyclotrons.

Chapter 6

Chemistry and Separation: Overview

6.1 Cerium

6.1.1 Introduction

Cerium is the most abundant member of the lanthanides. Chemically, cerium can be characterized as having two valence states, *viz.* Ce^{4+} or ceric and Ce^{3+} or cerous. This property is the important parameter that allows the easy separation of cerium from the other lanthanides. The ceric ion is a very powerful oxidizing agent but when associated with oxygen, which is a strongly coordinating hard ligand, it is completely stabilized as CeO_2. This form of cerium is the most widely used in industry.

Cerium was named after the asteroid, Ceres, which in turn was named after the patron saint of Sicily and the Roman goddess of food and plants. It was first isolated from the impure oxide in 1803. The recognition that cerium was a unique element, and its relationship to other elements, were factors in the gradual development of the Periodic Table concept. The separation and identification of all the individual 4f elements, cerium included, caused considerable confusion a hundred years ago. This process did however lead to our eventual understanding of atomic structure.

Cerium was introduced to the public for the first time in 1891 when gas lights were successfully installed in front of the Opern Cafe in Vienna. These lights used the Welsbach gas mantle that had fabric impregnated with thorium- and cerium oxide. This form of illumination soon became widespread throughout Europe. Natural cerium is still found in lighting today, as well as in televisions, automobiles and now the radioactive isotopes of this element may also start to play a role in our daily lives.

Table 6.1: Properties of cerium

The Element Cerium	
Chemical Symbol	Ce
Atomic Number	58
Atomic Weight	140.12
Electron Configuration	$[Xe]4f^26s^2$
Valencies	3, 4
Ionic Radius for (3+)	114 pm
8-coordination (4+)	97 pm
Magnetic Moment	$2.4\mu B$
Cerium Metal	
Crystal Structure	fcc
Melting Point	798 °C
Boiling Point	3443 °C
Density	6.77 g/cm^3
Metallic Radius	182 pm
Thermal Conductivity	0.110 w/cm^{-K}
Specific Heat,	0.192 J/g K
Heat of Fusion	1305 cal/mole
Thermal Expansion	6.3x10^{-6} K^{-1}
Electrical Conductance	0. 13 Ω^{-1}

In the bulk form the element is a reactive metal, prepared by the calciothermic reduction of the fluoride, CeF_3:

$$2CeF_3 + 3Ca \Rightarrow 2Ce + 3CaF_2.$$

A slight excess of calcium is used and the exothermic reaction, carried out in a tantalum crucible, is initiated at 900 °C. After physical separation of the upper layer of immiscible fluoride slag, vacuum distillation removes unreacted volatile Ca. Cerium can also be made by the electrolytic reduction of fused chloride. On a fresh surface the metal has a steely lustre but rapidly tarnishes in air due to the surface formation of oxide and carbonate species. For protection against oxidation the metal is usually stored in a light mineral oil. When made finely divided, *e.g.* on being cut, it can be strongly pyrophoric and for this reason it is used as the ferro-alloy mischmetall in lighter flints and ordnance. The metal reacts steadily with water, readily dissolves in mineral acids and is also attacked by alkalies. It will react with most non-metals upon heating [47]. Table 6.1 shows a synopsis of the properties of cerium.

6.1.2 Electronic Structure and Oxidation States

Cerium is the most reactive of the lanthanides. It is very electro-positive and has predominantly ionic chemistry due to the low ionization potential for the removal of the three most

weakly bound electrons. The energetics are such that for all lanthanides the most stable state is a trivalent one, with [Xe]$4f^n$, *i.e.* for Ce^{3+}, [Xe]$4f^1$ [48].

The 4f electrons are well-shielded from influence by the external environment and hence the chemical behavior of all Ln^{3+} ions, including Ce^{3+}, is very similar. At the start of the Ln series though, the 5d orbitals are not much higher in energy than the 4f shell and with cerium a potential 4f - 5d charge transition accounts for the absorption by Ce(III) compounds in the u.v. region just outside the visible spectrum.

The relative increased stability of empty $4f^0$, half-full $4f^7$ and completely full $4f^{14}$ shells can for certain elements cause oxidation states other than three also to be reasonably stable, in particular Ce^{4+} with a [Xe]$4f^0$ configuration.

6.1.3 Cerium(IV) Chemistry and Compounds

The tetravalent cerium state, ceric, is (apart from Eu^{2+}) the only non-trivalent lanthanide ion stable in aqueous solution. The influence of the higher cation charge and a smaller ionic size make ceric salts much more hydrolyzed in aqueous solution than those of the trivalent lanthanides:

$$\mathbf{[CeL}_m\mathbf{(H_2O)]}^{n+} + \mathbf{H_2O} \Rightarrow \mathbf{[CeL}_m\mathbf{(OH)]}^{(n-1)+} + \mathbf{H_3O}^+$$

Consequently, ceric salt solutions are strongly acidic. Basic salts tend to form in solution and there are no stable simple salts of weak acids. Ceric salts tend to be orange or red in color due to charge transfer interactions. The simple uncoordinated ceric ion, *e.g.* in a glass matrix or the oxide, absorbs in the ultraviolet portion of the spectrum but not in the visible. The details of the spectra are very dependent on composition.

The fluorite structure, with its large crystal lattice energy, provides an exceptionally strong stabilizing influence for tetravalent cations and is adopted by CeO_2 (see below), preferentially stabilizing this oxide form rather than Ce_2O_3 with trivalent cerium. Some complex fluorides and oxides are also stabilized by a similar factor. Compounds of cerium(IV), other than the fluoride, oxide and related materials, are less stable but can be prepared. Those most readily obtained include the sulfate, $Ce(SO_4)_2$, and certain "double" salts [47]. Orange crystals of ceric sulfate can be obtained from solutions prepared by dissolving a reactive cerium precursor, such as the freshly precipitated hydrated oxide, in sulfuric acid in excess to prevent hydrolysis to basic insoluble salts. The double salts, ceric ammonium nitrate and ceric ammonium sulfate (see below for more suitable names) are stable orange compounds prepared by dissolving freshly prepared (hence reactive) hydrate or oxide, in

excess of the appropriate acid, adding the correct amount of ammonium salt, and evaporating down at low temperatures to cause crystallization. The tetravalent cerium is present in the anion, not the cation, of these salts. The crystal structure, with cerium(IV) at the center of the anion complexed, for example, by six bidentate nitrate groups, shows that the formal name is di-ammonium hexanitratocerate. Similarly solid sulfate analogues are correctly - sulfatocerates, *e.g.*:

$$\mathbf{(NH_4)_2\ [Ce(NO_3)_6]\ :\ (NH_4)_4\ [Ce(SO_4)_4].2H_2O\ :\ (NH_4)_2\ [Ce(SO_4)_3].}$$

The complex anions, along with other similar stable anionic species, exist in the aqueous solutions. The complex equilibria between these species and the dependence on pH means that the solution chemistry of cerium(IV) is intricate.

Chlorocomplexes of cerium(IV) are not as stable as nitrato or sulfato derivatives due to oxidation of Cl^- by Ce(IV). The simple tetrachloride $CeCl_4$ is unstable but salts of the $[CeCl_6]_2^{4-}$ ion can be stabilized with large cations such as $NEthyl_4$ and also neutral chlorocomplexes can be obtained with large chelating ligands.

Cerium in the tetravalent state is a strong oxidizing agent and can be reduced by, for example, oxalic acid, halogen acids, sulfur dioxide and hydrogen peroxide. The exact redox potential (E) for the reaction Ce(IV)/Ce(III) ranges from ∼1.3V (1N HCl) to ∼1.8V (6N $HClO_4$) and depends strongly on the concentration, electrolyte and on which small anionic groupings are complexed to the cerium ion:

$$E = 1.61 + 0.059 \log \frac{[Ce^{4+}]}{[Ce^{3+}]} \tag{6.1}$$

Despite the lower standard electrode potential, E, for the H_2O/O_2 couple (1.23V), aqueous solutions containing Ce(IV) species are stable, probably for kinetic reasons. Water can nevertheless be oxidized to oxygen by Ce(IV) in the presence of catalysts such as Pt or RuO_2 [49]. Cerium(IV) ion oxidation is a useful tool in organic chemistry [50] and can be used for quantitative volumetric oxidation reactions, "cerate oxidimetry", in analytical chemistry. In addition, the oxidizing ability of Ce^{4+} offers possibilities in indirect electroorganic synthesis where, after a reaction, the Ce^{4+} can be regenerated from the Ce^{3+} in a separate electrochemical step.

6.1.4 Cerium(III) Chemistry and Compounds

Trivalent cerium, cerous, closely resembles (apart from its possible oxidation to Ce(IV)) the other trivalent lanthanides in chemical behavior. The early original literature [51],

contains a lot of descriptive chemistry, and current publications [52] can provide detailed chemical and physical property information.

The simple cerous salts can be prepared by dissolving the oxide or a more reactive precursor in the appropriate acid, or where possible, produced by precipitation from solution. Upon crystallization, most salts are capable of forming a wide variety of hydrated species, with the hydrates of the soluble salts tending to be hygroscopic. Basic salts, *e.g.* $Ce(OH)CO_3$, may be formed and can be contaminants in the solid salts.

Ce(III) forms a water-insoluble hydroxide, carbonate, oxalate, phosphate and fluoride, sparingly soluble sulfate and acetate, and soluble nitrate and chloride as well as the bromide. With the sparingly soluble sulfate and acetate, an increase in temperature causes a decrease in solubility. In solution the salts are only slightly hydrolyzed. (The carbonate is readily prepared, easily handled, and is a convenient precursor for the preparation of other derivatives.) The stability of the tetravalent oxide means that, after intermediate hydroxy- and oxy-species, CeO_2 is the end product of the calcination of most Ce(III) salts although with halides, stable oxyhalides, CeOX, can be formed.

6.1.5 Cerium Dioxide, CeO_2

The most stable oxide of cerium is cerium dioxide, CeO_2, also called ceria or ceric oxide. (The sesquioxide, Ce_2O_3, with trivalent Ce, can be prepared under strongly reducing conditions but is unstable in air and water and readily converts to the dioxide. Consequently, it is not suitable for target material.) Cerium (along with the other lanthanides) has one of the highest free energies of formation for an oxide [47].

The oxide is soluble in mineral acids but can prove difficult to dissolve unless a trace of reducing agent such as hydrogen peroxide is added. Ceria has the fluorite (CaF_2) structure, Fm3m space group, with 8-coordinate cations and 4-coordinate anions. It can be visualized as a cubic close-packed array of metal atoms with oxygens filling all the tetrahedral holes. The structure-determining OCe_4 coordination tetrahedra thereby share all edges in three dimensions.

When pure, CeO_2 is a very pale yellow probably due to Ce(IV) - O(II) charge transfer transitions. The color of the oxide is sensitive not only to stoichiometry but also to the presence of other lanthanides. A slight trace ($\sim 0.02\%$) of Pr results in a buff color attributable to Ce(IV) - Pr(III) transitions. (With higher values of Pr ($\sim 2\%$) the material becomes a potential red pigment [53].) Grossly non-stoichiometric ceria samples are reported to be blue, related to Ce(IV) - Ce(III) transitions. In addition, as the oxide is usually produced

by the calcination of a precursor salt, the observed color depends on the extent of that calcination.

Ceria can be sintered (at ∼1400 °C) to high densities (> 97% theoretical) by the addition of trace amounts (< 1.0 %) of oxides such as TiO_2 or Nb_2O_5. These additives work either by the formation of a transient liquid-phase intermediate, *e.g.* $CeTi_2O_6$ (m.p. 1350 °C), or by suppressing oxygen deficiencies, *e.g.* with high valent Nb. This phenomenon might be useful for targets that behave better under bombardment conditions, provided the impurities formed from the additives can be successfully removed from the final product.

6.2 Lanthanum

6.2.1 Introduction

Lanthanum is the first member of the lanthanide series and is recovered from the minerals bastnasite and monazite. It is the second most abundant lanthanide after cerium and was first isolated in 1839 by C. G. Mosander from the cerium of J.J. Berzelius. Its name is derived from the Greek word "lanthanein" which means "to lie hidden". In broad terms the chemical properties of the lanthanides fall between those of the alkaline-earths and that of iron/aluminum. La(III) is the only easily accessible valence state for lanthanum and the chemistry of La(III) species is the prototype for the behavior of all the trivalent lanthanides (Ln^{3+}) [52]. Lanthanum is the least acidic of the lanthanides. Table 6.2 gives some of the properties of lanthanum.

6.2.2 Chemistry of Lanthanum and the Lanthanides

There is often a gradual, nearly-linear, change in properties along the lanthanide series from La to Lu, attributable to a reduction in ionic size from the largest, La, to the smallest, Lu (the so-called "lanthanide contraction") as the 4f shell fills. This size contraction arises because of poor shielding of the outer electrons, from the coulomb forces of the atomic nucleus, by the highly directional 4f electrons. The 4f electrons themselves are shielded from interaction with external forces and have little influence on chemical reactions. Consequently, when there is no change in 4f electron count the chemistry of all the lanthanides is very similar. This makes them extremely difficult to separate [54].

La^{3+}, and all of the trivalent Ln^{3+} ions, form compounds based on:

Table 6.2: Properties of lanthanum

The Element Lanthanum	
Chemical Symbol	La
Atomic Number	57
Atomic Weight	138.91
Electron Configuration	$[Xe]4f^0 5d^1 6s^2$
Valency	3
Ionic Radius, 8-coordination	117.2 pm
Magnetic Moment	$0\mu B$
Lanthanum Metal	
Crystal Structure	dhcp
Melting Point	918 °C
Boiling Point	3464 °C
Density	6.15 g/cm^3
Metallic Radius	188 pm
Thermal Conductivity	0.134 W/cm^{-K}
Specific Heat,	0.195 J/g K
Heat of Fusion	6.20 kJ/mole
Thermal Expansion	4.5 K^{-1}
Electrical Conductance	Ω^{-1}

- ionic bonding between cation and ligand atom,
- preference for bonding with negatively charged "hard" atoms, and in the order 0 > N > S, and
- lack of stereochemical definition in the arrangement around the cation.

One consequence is that water molecules and hydroxide ions are particularly strong ligands and in aqueous solutions only negatively charged oxygens, *e.g.* in oxalates and carbonates, can also bind strongly.

At pH's on the acidic side of ~ 6 the lanthanide ions will exist as unhydrolyzed aquo ions. If the pH increases, goes basic, hydrolysis of the hydrated cation occurs:

$$\mathbf{Ln(H_2O)_n^{3+} + H_2O \Rightarrow Ln(H_2O)_{n-1}OH^{2+} + H_3O^+ \Rightarrow Ln(H_2O)_{n-2}(OH)_2{}^+ + H_2O^+.}$$

and the hydroxide precipitates out at a pH ranging from 7.5 (La) to 5.8 (Lu).
For the simple compounds, aqueous solubility can be summarized as follows:

readily soluble: nitrate, chloride, bromide, and iodide,
($\sim$ 400 g oxide-eq./l).

partially soluble: acetate, sulfate,
($<\sim$ 100 g oxide-eq./l and occasionally with an inverse temp./solubility relationship).

insoluble in water: oxide, carbonate, oxalate, fluoride, hydroxide, and phosphate.

Double salts can sometimes be less soluble than the simple soluble salts, *e.g.* La/Mg nitrates and sulfates.

In the solid state, the precise coordination arrangement around the cation is very variable, being determined by ligand flexibility, chelating effects, overall packing, etc. The coordination number around the central Ln atom, however, is often decided by the packing of oxygen atoms from the anions and consequently similar coordination numbers for any individual lanthanide are found, somewhat independent of the actual anion. For the lighter lanthanides, a coordination number of 9 is common whereas for the heavier smaller cations, 8 is the choice. The switch over from 9 to 8 often leads to a structural change within the lanthanide series, *e.g.* with oxides, nitrates and phosphates. [48]

Lanthanum, and all the lanthanides, form very stable complexes with chelating oxygen-bonding ligands such as EDTA. Lanthanum, however, is very electro-positive (as are all the other lanthanides) and does not readily form complexes with pi-bonding ligands nor form covalent Ln-C bonds, *i.e.* true organometallic compounds. In inert environments, though, a wide range of Ln-C-donor compounds can be prepared. Most of these, however, are not stable with respect to air and moisture [55].

6.2.3 Oxides of the Lanthanides

The Ln_2O_3 sesqui-oxides are the stable well-defined solids usually obtained as the final product of the calcination in air of most Ln metals and Ln salts such as oxalates, carbonates and nitrates. This is a consequence of the high thermodynamic affinity of the lanthanide elements for oxygen and the stability of the Ln(III) valence state. The lanthanide oxides have the greatest, most negative, standard free energies of formation for any oxides, accounting for their exceptional thermodynamic stability [56] . The basic physical and chemical data for the oxides are summarized in Table 6.3.

The Ln(III) ion's size, ranging for 8-coordination from 116 pm for La to 98 pm for Lu, is not so different from that of the O^{2-} anion. This, along with the imposed Ln_2O_3 formula, means that the crystal structures of the Ln_2O_3's are not easy to visualize, unlike oxides of smaller elements where the cations fit into holes within arrays of close-packed O^{2-} ions. The A- and B-type Ln_2O_3 structures can be described as based on layers of polymeric $[LnO]_n^{n+}$ cations separated by discrete layers of O^{2-} anions. (Similar $[LnO]_n^{n+}$ layers are seen in many Ln oxo-compounds.) The arrangement around the Ln ion is 7-coordinate with several differing Ln-O distances [48].

Table 6.3: Properties of Rare Earth Oxides $\mathbf{Ln}_m\mathbf{O}_n$

Ln	stable oxide	formula wt.	element %	color	structure type	density $g.cm^{-3}$	m.pt. °C
La	La_2O_3	325.8	85.3	white	A	6.6	2305
Ce	CeO_2	172.1	81.4	off white	[flourite]	7.3	2600
Pr	Pr_6O_{11}	1021.5	82.8	black	[flourite]	6.9	2200
Nd	Nd_2O_3	336.5	85.7	pale blue	A	7.3	2320

The C-type Ln_2O_3 structure is related to the fluorite, CaF_2, system by the ordered removal of one-quarter of the anions. (The Ln atom is coordinated to 6 oxygens but there are two vacant sites at cube corners.) As mentioned before, ceria (CeO_2), crystallizes as a fluorite and, as a consequence of the close similarity of the C-type Ln_2O_3 and fluorite structures, a range of stable intermediate non-stoichiometric compositions, $Ce_{l-x}Ln_xO_{2-x/2}$, are possible. Praseodymium and terbium oxides have complex fluorite-derived structures.

The oxides of the lanthanides are among the most thermally stable materials known, melting in the range 2200 - 2500 °C. In general, the metal cation structure is rigid up to the melting point whereas there is high mobility in the oxide anion lattice, starting above $\sim$ 300 °C.

The oxides dissolve in aqueous acids to produce the corresponding salt, *e.g.* nitrates and chlorides from HNO_3 and HCl respectively. The reactivity with acid is noticeably slower for C-type structures, *i.e.* the heavy Ln-oxides, than for the A- and B-types, the light Ln-oxides. To avoid hydrolysis of the hydrated lanthanide ion, the solutions should be kept acidic (pH < 4).

Furthermore, oxides with Ln(IV) ions are even less reactive and a trace of reducing agent, *e.g.* H_2O_2, may be required to take the oxide into solution. All the oxides will absorb water and/or carbon dioxide onto their surfaces, forming a layer of hydrate (this was clearly demonstrated in the preparation of the La_2O_3 targets as shown in Figure 6.1), carbonate or hydroxy-carbonate [57]. The A- and B- types do this more readily with lanthanum oxide being the most hygroscopic of the series.

6.3 Neodymium

Neodymium is the third most abundant lanthanide and is recovered from the minerals bastnasite and monazite. This element is of current commercial interest because of the de-

Figure 6.1: The target pellet on the left was photographed just after pressing while the photograph on the right shows the same pellet 24 hours later. This phenomenon clearly shows the effect of CO_2 absorbtion from the air by the La_2O_3 as explained by Bernal *et. al.* [57].

velopment of the Nd-Fe-B alloys as permanent magnet materials [58]. In addition Nd-based lasers are becoming more widely used. In all readily prepared compounds, neodymium is trivalent and the Nd^{3+} ion shows typical Ln^{3+} chemical properties (see Section 6.2). Table 6.4 lists some properties of neodymium.

Neodymium salts usually appear pale purple, a consequence of the spectral absorption of the Nd^{3+} ion. (The oxide, in contrast to the salts, is sky-blue, with the subtle shift from the normal Nd-salt color being caused by the stronger ligand field influences in the oxide.) Nd has a strong absorption band centered at 580 nm, others at $\sim$ 740 and $\sim$ 800 nm and several more bands of lesser strength [59]. The 580 nm band is in the yellow region and very close to the position of the eyes' maximum sensitivity. Consequently, the perceived color of Nd-containing glass, caused by both reflection and subtraction phenomena, depends on the spectrum of the illuminating light. This creates so-called "dichroism". The Nd ion colors artistic glassware and is added, for example, to the glass used in protective goggles worn during welding in order to block light of the 580 nm wavelength. Nd doped glass can be used as a contrast enhancing filter, clarifying the eye's discrimination between reds and greens, on CRT displays.

Table 6.4: Properties of neodymium

The Element Neodymium	
Chemical Symbol	Nd
Atomic Number	60
Atomic Weight	144.24
Electron Configuration	$[Xe]4f^46s^2$
Valency	3
Ionic Radius, 8-coordination	111 pm
Magnetic Moment	$3.62\mu B$
Neodymium Metal	
Crystal Structure	dhcp
Melting Point	1021 °C
Boiling Point	3074 °C
Density	6.72 g/cm^3
Metallic Radius	182.1 pm
Thermal Conductivity	0.165 W/cm^{-K}
Specific Heat,	0.190 J/g K
Heat of Fusion	7.14 cal/mole
Thermal Expansion	9.6 K^{-1}
Electrical Conductance	15.1 mΩ.cm^{-1}

6.4 Praseodymium

In most compounds this element is trivalent like lanthanum, and in chemical behavior Pr(III) compounds closely resemble the analogous La(III) derivatives (see Section 6.2). Table 6.5 lists some properties of praseodymium. Most Pr^{3+} salts are pale green due to strong absorption bands in the blue from 440 to 490 nm [59]. (Similar color and bands are seen in a glass matrix when Pr^{3+} is present.) Most praseodymium salts, when calcined in air, do not produce the sesquioxide, Ln_2O_3, but a black material whose composition is best expressed as Pr_6O_{11}.

The tetra-valent state of Pr is of just sufficient stability to form this oxide preferentially with mixed Pr valencies. Charge transfer behavior leads to the enhanced stability. (The Pr-O phase diagram is complex and several oxides that form a homologous series, Pr_nO_{2n-2}, are known, each with a defect fluorite structure.) The Pr(IV) ion is only stable in a few solid compounds, all oxide and fluoride based. A pale green Pr_2O_3 oxide can be made under strongly reducing conditions but it is not stable in air [60].

Praseodymium forms $\sim 4\%$ of the lanthanide content of bastnasite but all that proportion is not recovered as a separated pure Pr material because there is currently insufficient commercial demand. The element will be present in a small amount in almost all mixed light lanthanide derivatives, again because of the difficulty in separation. The most popular

Table 6.5: Properties of Praseodymium

The Element Praseodymium	
Chemical Symbol	Pr
Atomic Number	59
Atomic Weight	140.91
Electron Configuration	$[Xe]4f^36s^2$
Electronegativity	1.13
Valency	3 (4)
Ionic Radius, 8-coordination	113 pm
Magnetic Moment	3.60 μB
Praseodymium Metal	
Crystal Structure	dhcp
Melting Point	931 °C
Boiling Point	3520 °C
Density	6.77 g/cm^3
Metallic Radius	182.8 pm
Thermal Conductivity	0.125 W/cm^{-K}
Specific Heat,	0.193 J/g K
Heat of Fusion	6.89 kJ/mole
Thermal Expansion	6.7 K^{-1}
Electrical Conductance	14.7 mΩcm^{-1}

yellow ceramic pigment is a Pr doped zircon [61] that is "cleaner" and "brighter" than alternatives probably due to the Pr pigment having an optimum reflectance at $\sim$ 560 nm.

In the preparation a "mineralizer", usually a metal halide MX, must be present to ensure complete reaction. Presumably the vapor phase transport of Pr happens through the intermediacy of a transient $PrMX_n$ complex. The cause of the coloration has been attributed solely to the Pr^{4+} ion stabilized in the host $ZrSiO_4$ but it is also possible that charge transfer bands contribute. The color of potential red pigments such as $Ce_{l-x}Pr_xO_2$ [53] is certainly due to charge transfer bands associated with the Ce(IV)/Pr(III) system.

On excitation the Pr^{3+} ion shows a variety of emissions, depending strongly on the host lattice, due to the strong influence of that lattice on the energy of the excited 4f5d level. Pr doped fluoride fibers have been proposed for optical amplification at 1310 nm for telecommunications. This is a system that could rival erbium doped fiber amplifiers. Another application of Pr emission is in the scintillator Pr,Ce,F : Gd_2O_2S for X-ray computed tomography. Such scintillators need to be made as small translucent ceramics with an emitter with a very fast decay time (5 μs for Pr^{3+}) and a wavelength matching the detector's sensitivity [60].

Permanent magnets based on praseodymium have the potential to be comparable in prop-

erties to the well recognized samarium-cobalt material, $SmCo_5$. Certain oxides, added as powders (up to 1 wt%) prior to sintering, can suppress the formation of undesirable impurity phases. The added oxide reacts with any excess lanthanide in the starting alloy composition and keeps the overall Pr : Co ratio down to the desired 1 : 5. One esoteric use of this element is in the intermetallic $PrNi_5$ and $PrCu_6$ compounds, which has made the attainment of ultra-low temperatures possible in the milli- to micro-Kelvin range [62]. The ^{141}Pr nuclei have the requisite novel magnetic properties to achieve this feat.

6.5 Principles of Ion Exchange

6.5.1 Introduction

The chemical methods mentioned in this work all make use of ion exchange techniques to achieve separation of target materials from the radionuclides of interest. Ion exchange is a process in which ions, electrostatically bound to functional groups contained within a matrix, exchange with mobile ions from an external solution. Anions are involved in the exchange when the functional groups are positively charged, and conversely, cations are involved when they are negatively charged. By taking advantage of the fact that, under certain conditions, ion exchange media have a greater affinity for certain ionic species than for others, a separation of these species is possible. For example, the hydrogen form of a cation exchanger will release its hydrogen ion into solution and pick up a potassium ion from the solution according to the following equation:

$$\mathrm{R\text{ - }H + K^+ \leftrightarrow R\text{ - }K + H^+},$$

where R represents the insoluble matrix of the ion exchange resin. The negative counter ion of the potassium salt is not affected by the exchange since every potassium ion removed from the solution is replaced by a hydrogen ion and electro-neutrality is maintained.

Depending on the type of the functional group, ion exchangers can be divided into several types: weak acidic, weak basic, strong acidic and strong basic. In Table 6.6 the negative logarithm of the dissociation constant (pK) is presented for different functional groups. Media containing sulpho- and phospho-acidic groups and those containing tetra-ammonium basic groups are strong acidic and strong basic ion exchangers, respectively, whereas those containing phenolic and primary amino groups are weak acidic and weak basic ion exchangers, respectively. Media with carboxy groups and tertiary amino groups take a medium position between strong and weak acidic and basic ion exchangers, respectively.

Table 6.6: pK Values for the most common functional groups of organic ion exchangers.

Cation exchangers		Anion Exchangers	
Functional Group	pK	Functional Group	pK
-SO_3H(strong acidic)	1-2	-$N^+(CH_3)_3Cl^-$(strong basic)	1-2
-PO_3H_2	2-5	-$N^+(CH_3)_2(CH_2)_2OHCl^-$	4-6
-COOH	4-6		6-8
-OH(weak acidic)	9-10	-$N^+(CH_3)_2$(weak basic)	8-10

6.5.2 Selectivity and Equilibrium in Ion Exchange

Equilibrium in ion exchange can be described in terms of any of the following:

- The ion exchange isotherm,
- The separation factor,
- The selectivity coefficient,
- The thermodynamic equilibrium constant,
- The distribution coefficient.

These terms are defined and described by Helfferich [63]. It should be noted that selectivity coefficients are not constant and will vary with the experimental conditions of, for example, concentration, temperature and the presence of other ions or complexing agents in the solution. Most of these parameters can be extracted from manufacturers data or research literature. For general experimental purposes a few rules of thumb can be applied: for cationic organic ion exchange resins at low concentrations and the temperatures normally encountered in the lab, the affinity typically increases with (a) an increasing charge on the exchanging cation and (b) an increasing atomic number (decreasing hydrated ionic radii) of the exchanging cation, for example:

(a) $Li^+ < H^+ < Na^+ < K^+ < Cs^+ < Mg^{2+} < Co^{2+} < Ca^{2+} < Sr^{2+} < Ce^{3+} < La^{3+} < Th^{4+}$,

(b) $Li^+ < H^+ < Na^+ < K^+ < Cs^+$ (Li^+ is an exception, due to its high hydration energy).

For anions a typical series is as follows:

$F^- < CH_3COO^-$ (acetate) $< Cl^- < Br^- < CrO4^{2-} < NO^{3-} < I^- < C_2O_4{}^{2-}$ (oxalate) $< SO_4{}^{2-}$.

Changes in physical parameters and of the concentration of functional groups affect the distribution coefficient and can affect the driving force for the ion exchange process. High values of the distribution coefficient are always desirable for sorption of ions, and low values for the elution of ions.

The Ion Exchange Isotherm

Sorption equilibrium is usually described by an isotherm equation whose parameters express the surface properties and affinity of the sorbent, at a fixed temperature and pH.

A sorption isotherm describes the relationship between the amount of element adsorbed on the ion exchange material and the concentration of the dissolved ions of the same element in the mobile phase at equilibrium [64]. Equations often used to describe the experimental isotherm data are those developed by Freundlich, Langmuir and Dubinin-Radushkevich. The Freundlich and Langmuir isotherms are the most commonly used to describe the adsorption characteristics of ions adsorbed from aqueous solutions.

For the purpose of explanation we will only consider the Langmuir isotherm. The linear form of the Langmuir isotherm for the sorption of a single component, A, from solution on a single-site solid surface has frequently been applied to ion exchange reactions as follows:

$$\frac{C_\mathrm{A}}{q_\mathrm{A}} = \frac{C_\mathrm{A}}{Q} + \frac{1}{K_\mathrm{A} Q} \tag{6.2}$$

where C_A and q_A are the concentrations of A in the solution and the ion exchange material respectively. Q is the maximum sorption capacity, and K_A is a constant related to the sorption energy. In the Langmuir isotherm, it is assumed that there is no interaction between the sorbed species. Thus the sorption energy is equal for all exchange sites. This assumption makes K_A independant of the degree of sorption. A plot of $C_\mathrm{A}/q_\mathrm{A}$ vs. C_A would then give a straight line from which, following equation 6.2, Q and K_A can be obtained [65].

The Separation Factor

The separation factor, α, is given by the ratio of the distribution coefficients, K_d^A and K_d^B, of two different elements, A and B, that were determined under the same experimental conditions. It can be defined as follows:

$$\alpha_{\mathrm{A}}^{\mathrm{B}} = \frac{K_d^{\mathrm{B}}}{K_d^{\mathrm{A}}} \tag{6.3}$$

where A and B represents the two different elements of interest in the separation process. The separation factor gives an indication of how well the two elements can be separated from each other under a specific set of experimental conditions. For a given pair of ions from different elements, the more the separation factor differs from 1 (no separation) the better the separation of those two elements will be. The separation factor played an important role in the decisions taken for the separation of Nd and Pr, as will be explained in the next chapter.

The Selectivity Coefficient

The reaction during which the exchange of ions between a solution and solid ion exchange material takes place is typically reversible. An equilibrium can thus be established if a solution containing cation A^+, for example, is shaken with a solid ion exchange material, R containing cation B^+, and the A^+ ions displace the B^+ ions. This equilibrium can take anything from a few minutes to a few days, depending on the properties of the ion exchange material and the way it behaves in different solutions. The equilibrium can be written as follows:

$$\mathrm{BR} + \mathrm{A}^+ \rightleftharpoons \mathrm{AR} + \mathrm{B}^+$$

In a case where the cations in question are doubly charged, we can write the following expression:

$$2\mathrm{BR} + \mathrm{A}^{2+} \rightleftharpoons \mathrm{AR}_2 + 2\mathrm{B}^+$$

To represent the final distribution of concentrations use the selectivity coefficient, and it can be represented for ions of equal charge as follows:

$$E_{\mathrm{A}}^{\mathrm{B}} = \frac{[\mathrm{A}^+][\mathrm{BR}]}{[\mathrm{B}^+][\mathrm{AR}]} \tag{6.4}$$

where $[A^+]$ and $[B^+]$ indicate the concentration in the solution and [AR] and [BR] indicate the concentration in the ion exchanger. The assumption is made that B is held

more strongly than A by the ion exchange material.

Small effects of non-ideality aside, the ratio between the concentrations of the two ions does not change with dilution. This is not true for ions of unequal charge, where the ion of higher charge is usually more strongly held by the ion exchange material and as a result the distribution coefficient is shifted by dilution. Thus, the more diluted the solution becomes, the more strongly the ion of higher charge will be held by the resin. The opposite is also true.

The thermodynamic equilibrium constant

From a strictly thermodynamic point of view, a proper representation of the ion exchange equilibrium is not ideal. The partial molal free energies are not linear functions of the logarithms of concentrations and this is especially true for the exchange phase inside the ion exchange resin, where the ions are much closer together than they would be in an external solution. To compensate for non-ideality we introduce activity coefficients and represent the thermodynamic equilibrium coefficient as follows:

$$K_{\mathrm{A}}^{\mathrm{B}} = \frac{\bar{m}_{\mathrm{B}} m_{\mathrm{A}} \bar{\gamma}_{\mathrm{B}} \gamma_{\mathrm{A}}}{\bar{m}_{\mathrm{A}} m_{\mathrm{B}} \bar{\gamma}_{\mathrm{A}} \gamma_{\mathrm{B}}} \tag{6.5}$$

where m represents the molality and γ is the activity coefficient in solution and $\bar{m}$ and $\bar{\gamma}$ are the molality and activity coefficient in the ion exchange matrix.

The distribution coefficient

If a solute is introduced into a two phase system, which in the case of ion exchange chromatography is liquid/solid, it will become distributed between the two phases and when equilibrium is reached the solute distribution can be defined by the distribution coefficient. The distribution coefficient of a solute between the two phases is calculated as the ratio of the concentration of the solute in one phase to the concentration of the solute in the other phase under equilibrium conditions. Either phase may be used as the reference phase, but in ion exchange chromatography, the distribution coefficient always refers to the stationary phase first (*i.e.* the ratio of the concentration of the solute in the stationary phase to that in the mobile phase). The concentration may be taken as mass per unit mass in the dry solid phase and the mass per volume in the mobile phase and can be expressed as follows.

$$K_d = \frac{\text{mass of solute per gram of dry solid phase (ion exchange resin)}}{\text{mass of solute per cm}^3 \text{ of mobile phase (solution)}} \tag{6.6}$$

The magnitude of K_d is determined by the relative affinity of the solute for the two phases. Those solutes interacting more strongly with the stationary phase will exhibit a larger distribution coefficient and will be retained longer in the chromatographic system. Molecular interaction results from intermolecular forces of which there are three basic types. All intermolecular forces are electrical in nature. The three different types are termed *dispersion forces, polar forces and ionic forces.* All interactions between molecules are composites of these three forces.

Glasstone [66] suggested long ago that dispersion forces could be best described as follows, "*although the physical significance probably cannot be clearly defined, it may be imagined that an instantaneous picture of a molecule would show various arrangements of nuclei and electrons having dipole moments. These rapidly varying dipoles, when averaged over a large number of configurations, would give a resultant of zero. However, at any instant they would offer electrical interactions with another molecule resulting in interactive forces*".

Polar interactions arise from electrical forces between localized charges resulting from permanent or induced dipoles. They cannot occur in isolation, but must be accompanied by dispersive interactions and under some circumstances may also be combined with ionic interactions. Polar interactions can be very strong and result in molecular associations that approach, in energy, that of a weak chemical bond. Examples of such instances are "hydrogen bonding" and in particular the association of water with itself [67].

Polar compounds possessing dipoles have no net charge. In contrast, ions possess a net charge and consequently can interact strongly with ions having an opposite charge. Ionic interactions are exploited in ion exchange chromatography where the counter ions to the ions being separated are situated in the stationary phase. Ionic interactions are always accompanied by dispersive interactions and, usually, also with polar interactions. Nevertheless, in ion exchange chromatography, the dominant forces controlling retention usually result from ionic interactions.

6.5.3 Sorption and Ion Exchange

Sorption is a separation process involving two phases between which certain components can become differentially distributed. There are three types of sorption, classified according to the type of bonding involved:

(a) Physical sorption: There is no exchange of electrons in physical sorption, rather, intermolecular attractions occur between "valency happy" sites and are therefore independent of the electronic properties of the molecules involved. The heat of sorption, or activation

energy, is low and therefore this type of sorption is stable only at temperatures below about 150 °C.

(b) Chemical sorption: Chemical sorption, or chemisorption, involves an exchange of electrons between specific surface sites and solute molecules which results in the formation of a chemical bond. Chemisorption is typified by a much stronger sorption energy than physical sorption. Such a bond is therefore more stable at higher temperatures.

(c) Electrostatic sorption (ion exchange): This is a term reserved for coulombic attractive forces between ions and charged functional groups and is more commonly classified as ion exchange.

In addition to being ion exchangers, ion exchange materials can also act as sorbents. When they are contacted with an electrolyte solution the dissolved ions are concentrated on both the surface and in the pores of the ion exchange media. In a solution of weak electrolytes or non-electrolytes, sorption by ion exchangers is similar to that of non-ionic adsorbents. In a solution of strong electrolytes a sorption equilibrium results, owing to the electrostatic attraction between the ions in solution and the fixed ionic groups on the ion exchange media. Sorption equilibrium is normally represented by sorption isotherm curves.

Many forces and interactions have been found by experimentation to affect the sorption of non-electrolytes. Solutes may form complexes or chelates with the counter ions of the exchanger. Temperature variations may not only affect the state of the solute but also the condition of the exchanger. The molecular size of the solute and the degree of cross-linking of the exchanger will also affect the sorption kinetics.

6.5.4 Ion Exchange Capacity

The term "ion exchange capacity" is intended to describe the total available exchange capacity of an ion exchange resin, as described by the number of functional groups on it. This value is constant for a given ion exchange material and is generally given as milliequivalents per gram (meq/g), based on the dry weight of material in a given form (such as H^+ or Cl). For organic ion exchange resins it can be given as milliequivalents per millilitre (meq/mL), based on the wet fully swollen volume of a settled bed of resin. The numbers quoted in the literature vary widely for different resins. This number can be used to compare different resins or to calculate the total amount of resin to be added during a batch exchange process.

For the characterization of ion exchangers, two capacity parameters are commonly used: (a) the total static exchange capacity (which is determined under static conditions) and (b) the dynamic exchange capacity (which is determined by passing a solution through a

column of the exchanger). The exchange capacity depends on the number of functional group per gram of exchanger. The extent of the use of the total exchange capacity depends on the level of ionization of the functional groups of the exchanger and on the chemical and physical conditions of the process.

The operating or breakthrough capacity of a column type ion exchange system depends on its design and operating parameters, the concentration of the ions being removed and the effects of interference from other ions. In a column system for radionuclide purification, this generally refers to the maximum amount of an element the column can hold before it starts being released into the eluent. At this point, the ion exchange medium is considered to be saturated.

Some important parameters that affect the breakthrough capacity are the:

- Nature of the functional group on the exchanger,
- Degree of cross-linking,
- Concentration of the solution,
- Ionic valence,
- Ionic size, and
- Temperature.

6.5.5 Kinetics and Dynamics

When designing an ion exchange processing system for bombarded targets it is desirable to have an appreciation of the rate at which the reaction will occur. The available contact time will be influenced by the short-lived nature of most medically useful radioisotopes. This is especially important in the production of ^{139}Pr and ^{140}Nd, as discussed in this work, since the chemistry has to be performed at optimum times during the production process and cannot take too long to complete. When an ion exchanger particle is brought in contact with a solution, there is a static liquid film formed around it. If the column contains m grams of ion exchange medium, the total capacity of the column V_{tot} can be calculated as:

$$V_{tot} = K_d(m) \tag{6.7}$$

6.5.6 Limitations of Ion Exchangers

Certain characteristics of ion exchange materials and processes limit their applicability and efficiency. When used as a packed bed in a column, the complete removal of a specific radionuclide is not normally possible owing to leakage or breakthrough. This will cause the radionuclide to pass through without being captured. In a properly designed system this breakthrough may be very low, but will still be present. Leakage may be due to:

- Radionuclides in a colloidal form or attached to a finely divided particulate material (pseudo-colloidal);
- A portion of the radionuclide may be in a non-ionic or other non-exchangeable form;
- Mechanical problems, such as channeling in column systems, possibly due to a shrinkage of the resin beads or an uneven settling of the resin bed.

When used in a batch process, inadequate mixing will also limit the effectiveness of the ion exchange material. The total concentration of dissolved salts in solution must generally be low (<1 g/L). At high concentrations the exchange potentials for ions diminish and there is more competition for the available exchange sites between non-radioactive ions and the radioactive species. However, for specifically developed ion exchangers (usually inorganic) the tolerance for dissolved salts can be very high (*e.g.* up to 240 g/L) [68].

When used in a downward flow mode, the amount of suspended solids in the waste solution must be low to avoid the bed of ion exchanger blocking. To overcome this, upward flow is usually preferred.

6.5.7 Synthetic Organic Ion Exchangers

The largest group of ion exchangers available today are synthetic organic resins in a powdered (5 - 150 μm) or bead (0.5 - 2 mm diameter) form. The framework, or matrix, of the resins is a flexible random network of hydrocarbon chains. This matrix carries fixed ionic charges at various locations. The resins are made insoluble by cross-linking the various hydrocarbon chains. The degree of cross-linking determines the mesh width of the matrix, swelling ability, movement of mobile ions, hardness and mechanical durability. Highly cross-linked resins are harder, more resistant to mechanical and radiological degradation, less porous and swell less in solvents.

When an organic ion exchanger is placed in a solvent or solution it will expand or swell. The degree of swelling depends both on the characteristics of the solution/solvent and the exchanger itself and is influenced by a number of conditions, such as:

- The solvent's polarity,
- The degree of cross-linking,
- The exchange capacity,
- A strong or weak solvation tendency of the fixed ion groups,
- The size and extent of the solvation of counter ions,
- The concentration of the external solution,
- The extent of the ionic dissociation of functional groups.

The main advantages of synthetic organic ion exchange resins are their high capacity, wide applicability, wide versatility and low cost relative to some synthetic inorganic media. The main limitations are their limited radiation and thermal stabilities. In the field of short-lived radioisotope production, however, resins are exposed to relatively lower amounts of radiation than, for instance, waste recovery at a nuclear plant where the activity stays on the column for long periods of time. At a total absorbed radiation dose of 10^9 to 10^{10} rad, most organic resins will exhibit a severe reduction in their ion exchange capacity (a 10 to 100% capacity loss), owing to physical degradation at both the molecular and macroscopic level. In the separation of short-lived radioisotopes, the speed of the process is fast enough to allow separation without any significant reduction in ion exchange capacity.

Cation exchange resins are generally limited to operational temperatures below about 150 °C, while anion exchange resins are usually limited to less than 70 °C. This requires that some target solutions, such as the solution in the ^{139}Ce separation from La and Pr, be cooled after dissolution before their introduction to the ion exchange media.

The most common form of ion exchange resin is based on a copolymer of styrene and divinylbenzene. The degree of cross-linking is adjusted by varying the divinylbenzene content and is expressed as the percentage of divinylbenzene in the matrix; for example, 5% cross-linking means 5 mol% divinylbenzene in the matrix. Low divinylbenzene content resins are soft and gelatinous and swell strongly in solvents. Macroporous resins with high crosslinking (15 - 20%) are preferred for their large surface areas, high porosity and stability under extreme conditions. The high surface area provides increased solute retention and selectivity together with a superior loading capacity and, consequently, a wide dynamic range of separation.

Fixed ionic groups are introduced into resin matrices, *e.g.* by sulphonation, to create an ion exchanger. In sulphonation eight to ten SO_3H groups are added for every ten benzene rings in the structure. The H^+ of the SO_3H group then becomes the mobile or counter ion.

It can be replaced by a treatment with a solution containing another cation, *e.g.* a solution of NaOH will produce the SO_3Na group, with Na^+ as the mobile ion. Anion exchangers can be produced by creating NH_3^+ or N_2^+ functional groups on the matrix with OH^-, Cl^- or other anions as the counter ion.

6.5.8 AG MP-1 Resin

Bio-Rad AG MP-1 is a strongly basic, macroporous organic anion exchange resin. It is capable of exchanging anions of acidic, basic and neutral salts. Strong anion exchange resins are used for sample preparation, enzyme assays, metal separations and in the case of iThemba LABS, for the separation of radionuclides from target matrices after bombardment with protons. The resin has quaternary ammonium functional groups attached to the styrene divinylbenzene copolymer lattice. AG MP-1 has an effective surface area of approximately 23 square meters per dry gram with 20% porosity. This large capacity is the main motivation for using a macroporous resin, since a relatively minuscule amount of radionuclide needs to be separated from gram amounts of target material.

Since AG MP-1 is an anion exchanger, neutral species and cations do not interact with the resin. In the chloride form the counterion on the resin is Cl^-. The resin can be converted from one ionic form to another and it is usually used in a form that has a lower selectivity for the functional group than the sample ions to be exchanged. AG MP-1 is available in several particle size ranges. The flow rate in a chromatographic column increases with increasing particle size. Conversely, however, the attainable resolution increases with decreasing particle size and narrower size distribution ranges. Particle size is normally given in mesh sizes. The larger the mesh number, the smaller the particle size. 100-200 Mesh resin is classified as a medium mesh and is well suited for column applications where a balance has to be struck between flow rate and capacity of the column. These factors are particularly important in the separation of radionuclides. 200-400 Mesh resin gives higher resolution analytical separations, but the back pressure and the slow flow speeds that can be achieved with this resin size makes it impractical for the current application [69].

AG MP-1 has an excellent resistance against chemical, thermal and radiological degradation and is therefore very well suited to the separation of radionuclides. Another result of the large capacity is much faster reaction kinetics, allowing for higher flow speeds and thus faster separations.

6.5.9 AG MP-50 Resin

Bio Rad AG MP-50 is a strongly acidic, macroporous cation exchange resin. It is normally used for single step purification methods, for the concentration of cation solutes as well as the analytical separations of various mixed cationic solutes. AG MP-50 comprises of sulfonic acid functional groups attached to a styrene divinylbenzene copolymer lattice. AG MP-50 has an effective surface area of approximately 35 square meters per dry gram with about 30 - 35 % porosity.

In applications involving cation exchange resins, such as AG MP-50, neutral molecules and anions do not interact with the resin. In the hydrogen form the counterion on the resin is H^+. The resin can be converted from one ionic form to another. In normal operation it is used in a form that has a lower selectivity for the functional group than the sample ions to be exchanged, thus, almost always in the hydrogen form. The sample ions are then exchanged when introduced, and can be eluted by introducing an ion with a higher affinity for the resin or, as in the case of the separation Pr and Nd, using an eluant (α-HIB) that forms a complex with the sample ions which lowers the affinity for the resin and thus causes them to be eluted. In general, the lower the selectivity of the counterion, the more readily it exchanges for another ion of like charge. The order of selectivity can be used to estimate the effectiveness for different ions as eluants, with the most highly selective being the most efficient. The order of selectivity can be used to estimate the difficulty of converting the resin from one form to another [70].

6.5.10 Gradient Elution in HPLC

Even though high performance liquid chromatography was not used for this study, the principle of gradient elution was borrowed from this discipline and applied to normal ion exchange chromatography as will be discussed under the separation methods in the next chapter.

Gradient elution is used in HPLC for the same purpose that temperature programming is used in Gas Chromatography, that is, to accelerate the elution of strongly retained solutes. Depending on the interactive character of the stationary phase, the interactive character of the mobile phase is continually changed to have interactive properties more like those of the stationary phase during the development of a separation. As an example, if a reversed phase (*e.g.* silica bonded with long hydrocarbon chains) was used as the stationary phase in a liquid chromatography separation, the solutes would be held and retained predominantly by dispersion. To allow the dispersion forces to dominate in the separation process and retain the solutes, the mobile phase would be made strongly polar, for example, a 10% solution of acetonitrile in water. Now the solvent that has the greater dispersive charac-

ter in the mobile phase mixture is acetonitrile. Thus, if the proportion of acetonitrile is increased during chromatographic development, the dispersive interactions in the mobile phase will become larger until they can compete with those of the stationary phase and elute the dispersively held solutes [71].

Conversely, if the stationary phase was polar (*e.g.* silica gel) the mobile phase would be made dispersive (*e.g.* 5% ethyl acetate in n-heptane). The mobile phase would then be made progressively more polar by increasing the ethyl acetate content, so that the polar interactions between the ethyl acetate and the solutes would be able to compete with the polar interactions of the solutes with the hydroxyl groups of the silica gel and allow them to be eluted more quickly. There is a wide range of solvent mixtures that can be used in gradient elution and the two examples given are extreme to illustrate the basic factors controlling gradient elution. In practice, were the interactive difference between solutes is very subtle, for instance between Nd and Pr, very subtle mixtures of solvents may be necessary to make the gradient elution process successful.

Chapter 7

Separation: Methods and Results

7.1 Overview: Production of ^{139}Ce

The initial production of ^{139}Ce at iThemba LABS was developed based on the work of Mayer *et al.* [72] and MacDonald [73]. The experimental methods investigated to test and optimize this production are described in the following sections. These sections describe the initial separation method, the confirmation of the type of complex and finally an optimized separation of ^{139}Ce from lanthanum.

7.2 Separation of ^{139}Ce from a Pr target

7.2.1 Description

MacDonald described a rapid separation of carrier-free ^{144}Pr from ^{144}Ce on Dowex-1 anion exchange resin [73]. ^{144}Ce was oxidized to the Ce^{+4} state with $NaBrO_3$ in 9 N HNO_3 and ^{144}Ce then sorbed onto the resin column. ^{144}Pr was eluted with 9 N HNO_3 and the column washed with 3 N HNO_3 containing a few drops of hydrazine. Mayer *et al.* [72] separated ^{139}Ce from lanthanum cyclotron targets by anion exchange chromatography in bromic acid / nitric acid. The lanthanum target shavings ($\sim$ 1.65g) were dissolved in 4.0 M HNO_3 and the solution evaporated to dryness. The salts were then dissolved in 0.075 M $HBrO_3$ / 7.89 M HNO_3 and the solution heated until the evolution of bromine fumes became visible. After cooling the solution, ^{139}Ce was sorbed on a AG1-X8 resin column and the target material eluted with 0.075 M $HBrO_3$ / 7.89 M HNO_3. $HBrO_3$ was washed from the column with 7.89 M HNO_3 and ^{139}Ce finally eluted with 0.5 M HNO_3.

The above methods described by MacDonald and Mayer *et.al.*, gave acceptable separation of ^{144}Ce from ^{144}Pr and ^{139}Ce from lanthanum target material, respectively. However, the methods could not be applied directly to separate ^{139}Ce from praseodymium, using a thick praseodymium target, or from lanthanum, using a thick lanthanum oxide target. A

typical mass of a praseodymium target used at iThemba LABS is $\sim$ 15 g. A method was developed to process these targets using nitric acid media. This method was presented at the 4^{th} Conference and Workshop on Cyclotrons and Applications in Cairo, Egypt in 2001 [74].

7.2.2 Reagents and Apparatus

Only analytical grade reagents were used. Praseodymium metal (99.9%) was obtained from Goodfellow Cambridge Ltd., Cambridge, England. Only deionized water was used and was obtained from a Millipore Milli-Q Water System. The strong acid cation exchange resin AG50W-X12 (hydrogen form, 100-200 mesh particle size) and the strong basic anion exchange macroporous resin, AG MP-1 (chloride form, 100-200 mesh particle size), were both supplied by Bio-Rad Laboratories, Richmond, California. The anion exchange resin was converted to the nitrate form before use.

A polyethylene tube (20 mm i.d. and 200 mm long) fitted with a 70 μm frit at the bottom was used as a cation exchange column. The column was filled with slurry of AG 50W-X12 resin until the settled resin reached a mark indicating a volume of 60 mL. A 70 μm frit was placed on top of the resin in the column. A plunger made of a Teflon rod [20 mm diameter, 40 mm long, with a hole (10 mm bore) drilled through the length, fitted with an O-ring near the bottom and a luer-fitting at the top] was used to seal the column at the top. The plunger was pushed firmly onto the frit until the resin column was compacted to a volume of $\sim$ 58 mL.

A polyethylene tube (10 mm i.d. and 70 mm long) fitted with a 70 μm frit at the bottom was used as an anion exchange column. The column was filled with slurry of AG MP-1 resin until the settled resin reached a mark indicating a volume of 5 mL. A 70 μm frit was placed on top of the resin in the column. A plunger made of a Teflon rod [10 mm diameter, 30 mm long, with a hole (1 mm bore) drilled through the length, fitted with an O-ring near the bottom and a luer-fitting at the top] was used to seal the column at the top. The plunger was pushed firmly onto the frit until the resin column was compacted to a volume of $\sim$ 4.5 mL. The resin was equilibrated with 6.0 M HNO_3 - 0.3 M $HBrO_3$.

High-resolution γ-ray spectrometric analysis, with a high purity germanium detector and multichannel analyzer, was used to determine the yield and percentage efficiency of the experimental method.

7.2.3 Bombardment of Target

The Pr target consisted of a 14.77 g disk (20 mm diameter and 7 mm thickness) encapsulated in an aluminium capsule. The target was bombarded, in a tandem configuration in

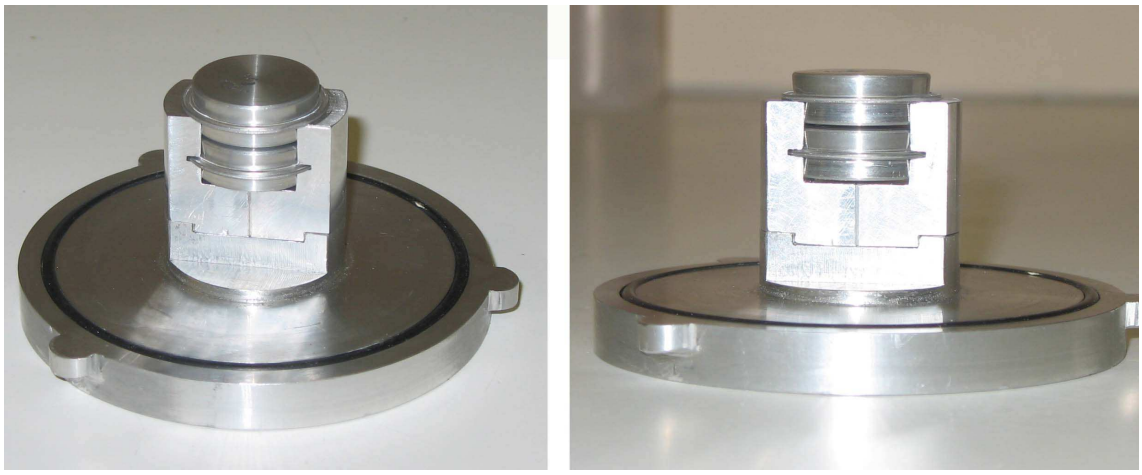

Figure 7.1: The two pictures show different views of the tandem target arrangement used to produce ^{139}Ce. The target at the top is the Pr and will see the proton beam first, thus it is in the higher energy window. The bottom target contains the La_2O_3 target. The space in between the targets allows for a layer of cooling water to be forced between the targets.

front of a La_2O_3 target (5.24 g disk), with a 66 MeV proton beam (energy window: 61.5 $\rightarrow$ 25.5 MeV for Pr and 18.1 $\rightarrow$ 0 MeV for La_2O_3; current 5 μA) for 0.5 hrs to achieve a total integrated charge of 2.51 μAh. The target arrangement is shown in Fig. 7.1.

7.2.4 Preparation of 0.3 M $HBrO_3$

An aqueous potassium bromide solution (12.53 g of $KBrO_3$/50 mL) was prepared and heated to 50 °C together with the column. This was necessary to prevent the $KBrO_3$ from precipitating. The solution was then passed through the cation exchange resin, AG 50W-X12, column and the first 20 mL of the eluate was discarded. The K^+ ions were sorbed on the resin and $HBrO_3$ was eluted with warm water. The eluate was collected in a 250 mL volumetric flask and made up to the mark with cold water. Of this solution, 200 ml was mixed with 416 mL HNO_3 (65%) and diluted to 1000 mL to obtain the 6.0 M HNO_3 - 0.3 M $HBrO_3$ solution.

7.2.5 Separation of ^{139}Ce from the target material

The aluminium capsule, containing the praseodymium target, was cut open at one side and the target removed. The target was placed in a polyethylene bottle containing 125 mL 4.0 M HNO_3. The initial reaction was quite vigorous. When the reaction had slowed down, 50 mL of 70% HNO_3 was added and the dissolution continued until Pr was completely dissolved. After the dissolution of Pr, the solution was decanted into a beaker and heated to 100 °C. The bottle and capsule were rinsed with five 25 mL portions of 70% HNO_3 and these solutions were also added to the beaker. 75 mL 0.3 M $HBrO_3$ was added to the beaker and the solution was heated until its color turned dark brown and fumes of bromine

were released.

The heat was turned off and the solution was allowed to cool for 10 minutes. The beaker was then put in a water bath at room temperature and stirred for 10 minutes. Finally the beaker was placed in ice water and the solution was stirred for another ten minutes. After the solution in the beaker had cooled down to $\sim$ 20 °C, 25 mL 0.3 M $HBrO_3$ was added to the beaker and the solution pumped through the resin column with a peristaltic pump at a flow rate of 5.0 mL/minute. Pr was eluted with 400 mL of the 6.0 M HNO_3 - 0.3 M $HBrO_3$ solution and the $HBrO_3$ washed from the resin column with 25 mL of 6.0 M HNO_3. Finally, ^{139}Ce was eluted from the resin with 50 mL 0.2 M HNO_3 containing 2 mL H_2SO_3. The eluate was collected and the activity measured by γ-ray spectrometry.

7.2.6 Results

The recovered ^{139}Ce activity, when converted to mCi and corrected for decay comes to 75.3% of the total activity measured in the mother solution after dissolution of the target material. During the load step of the separation procedure, the last fraction of load solution changed color back from dark brown to green, indicating that the BrO^{3-} had been used up and the Ce was changing back to the (III) oxidation state. This would lead to a fraction of the Ce not being retained on the column. A contributing reason for the loss can be the influence of the high concentration of Pr on the retention of Ce on the column. The recovered ^{139}Ce was nevertheless of the highest quality in terms of radionuclidic purity.

7.3 Determination of the complexes formed by ^{139}Ce during oxidation in H_2SO_4

7.3.1 Description

Two subsequent experiments were performed to determine how the ^{139}Ce is retained on cation and anion exchange columns when the oxidation of Ce was performed in the presence of H_2SO_4. A part of this investigation was to test if $NaBrO_3$ could be used instead of $HBrO_3$ for the oxidation of Ce.

7.3.2 Experiment A - Cation Exchange

Only analytical grade reagents were used. The ^{139}Ce from the previous separation was used as tracer to follow the Ce through the load, wash and elution steps. Only deionized water was used and was obtained from a Millipore Milli-Q Water System. The strong acid cation exchange resin AG MP-50 (hydrogen form, 100-200 mesh particle size) was supplied

by Bio-Rad Laboratories, Richmond, California.

A polyethylene tube (10 mm i.d. and 60 mm long) fitted with a 70 μm frit at the bottom was used as a cation exchange column. The column was filled with slurry of AG MP-50 resin until the settled resin reached a mark indicating a volume of 5 mL. A 70 μm frit was placed on top of the resin in the column. A plunger made of a Teflon rod [10 mm diameter, 30 mm long, with a hole (1 mm bore) drilled through the length, fitted with an O-ring near the bottom and a luer-fitting at the top] was used to seal the column at the top. The plunger was pushed firmly onto the frit until the resin column was compacted to a volume of $\sim$ 5 mL. The resin was equilibrated with 10 mL 0.45 M H_2SO_4 - 0.1 M $NaBrO_3$.

A 10 mL fraction of the solution containing ^{139}Ce tracer was placed in a vial and the activity determined by γ-ray spectrometry. The solution was then quantitatively washed into a beaker and evaporated to dryness. The resultant residue was then taken up in 10 mL 0.5 M H_2SO_4. To this solution, 1 mL of 1 M $NaBrO_3$ was added. The solution was boiled for 5 minutes and left to cool to ambient temperature. After the solution had cooled it was passed through the prepared column and the eluates collected in 5 mL serum vials. The column was washed with 50 mL 0.45 M H_2SO_4 - 0.1 M $NaBrO_3$ and again the eluate was collected in 5 mL serum vials. Finally the ^{139}Ce was eluted from the column with 5.0 M HCl containing 10% H_2SO_3. The eluate was collected in 5 mL fractions and checked for activity using γ-ray spectrometry. The elution was continued until no more radioactivity was released from the column. The resin was finally removed from the column and transferred to a serum vial. The activity retained on the column was then determined by γ-ray spectrometry.

7.3.3 Results

The ^{139}Ce elution curve is shown in Fig. 7.2. It is clear that the ^{139}Ce activity was quantitatively retained on the column during the load step of the separation and that there was no loss during the wash step. One can conclude that ^{139}Ce is retained on the column as Ce^{+4}. During the elution step, 98.2% of the activity was recovered. It would therefore seem that this method may be well suited to the separation of ^{139}Ce from Pr and even La. One concern, however, is the large elution volume (250 mL, see Fig. 7.2), and further optimization of this method will therefore be required before it can be used for target processing.

7.3.4 Experiment B - Anion Exchange

Only analytical grade reagents were used. The ^{139}Ce tracer solution was again used to follow the Ce through the load, wash and elution steps. Only deionized water was used

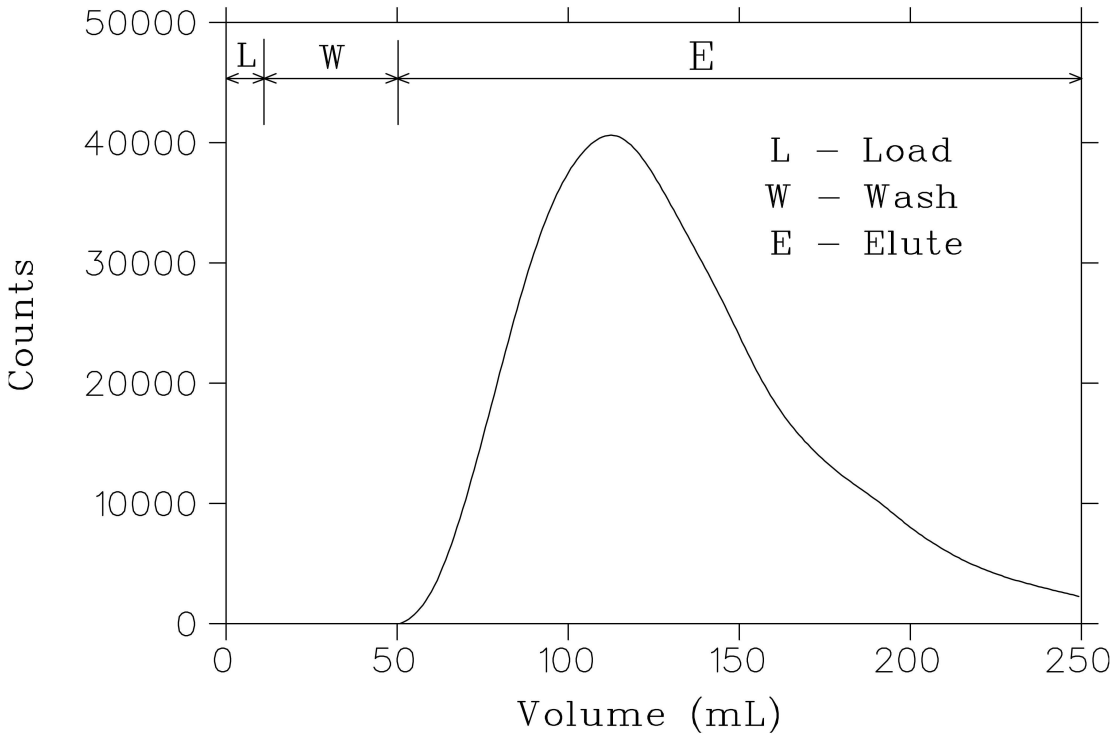

Figure 7.2: Elution curve of ^{139}Ce from the AG MP-50 resin after separation. It is clear that no activity was lost during the wash and load steps and 98.2% was removed from the column during elution.

and was obtained from a Millipore Milli-Q Water System. The strong basic anion exchange resin AG MP-1 (H-form, 100-200 mesh particle size) was supplied by Bio-Rad Laboratories, Richmond, California.

A polyethylene tube (10 mm i.d. and 60 mm long) fitted with a 70 μm frit at the bottom was used as an anion exchange column. The column was filled with a slurry of the AG MP-1 resin until the settled resin reached a mark indicating a volume of 5 mL. A 70 μm frit was placed on top of the resin in the column. A plunger made of a Teflon rod [10 mm diameter, 30 mm long, with a hole (1 mm bore) drilled through the length, fitted with an O-ring near the bottom and a luer-fitting at the top] was used to seal the column at the top. The plunger was pushed firmly onto the frit until the resin column was compacted to a volume of $\sim$ 5 mL. The resin was converted to the sulphate form by passing 20 mL of 5.0 M H_2SO_4 through the column. The column was then equilibrated with 10 mL 4.9 M H_2SO_4 - 0.1 M $NaBrO_3$.

A 10 mL fraction of ^{139}Ce tracer solution was placed in a vial and the activity determined by γ-ray spectrometry. The solution was then quantitatively washed into a beaker and evaporated to dryness. The resultant residue was then taken up in 10 mL 5 M H_2SO_4. To this solution was added 1 mL of 1 M $NaBrO_3$. The solution was boiled for 5 minutes and left to cool to ambient temperature. After the solution had cooled it was passed through the prepared column and the waste collected in 5 mL serum vials and checked for activity

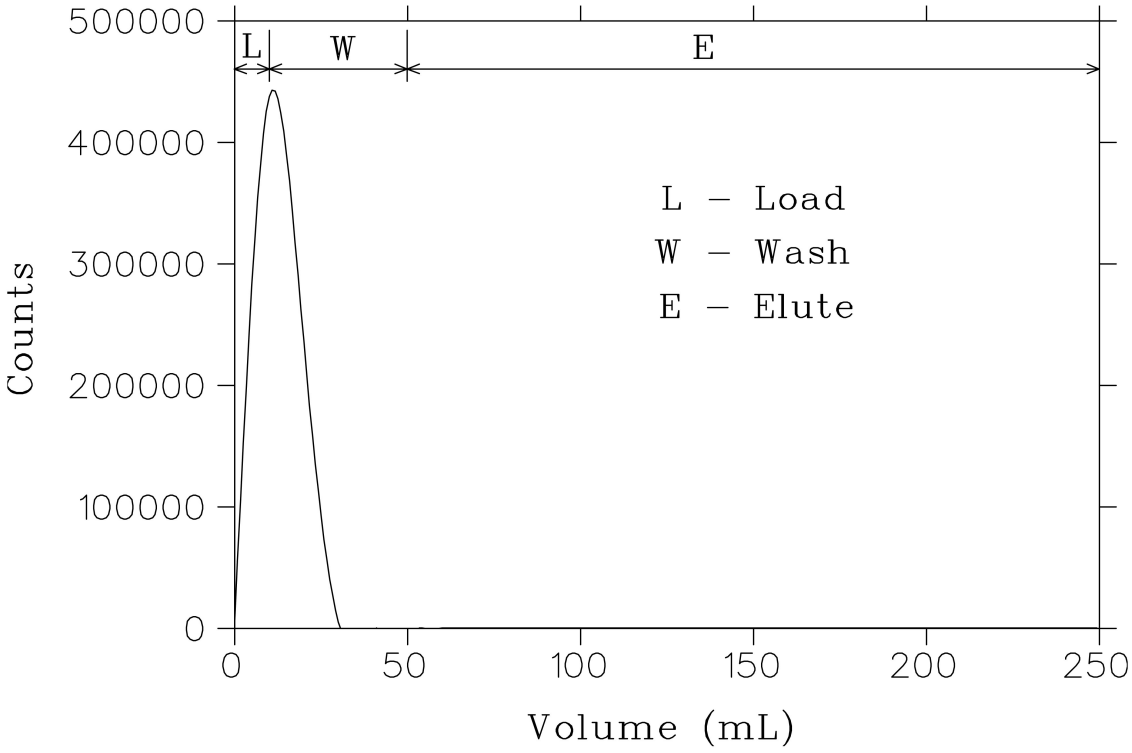

Figure 7.3: Elution curve of ^{139}Ce from the AG MP-1 resin during the separation. It is clear that all the activity was washed through the column without retention during the load and wash steps. 100% of the activity was recovered from the column.

using γ-ray spectrometry. The column was washed with 50 mL 0.45 M H_2SO_4 - 0.1 M $NaBrO_3$ and again the waste was collected in 5 mL serum vials and checked for activity using γ-ray spectrometry. The elution step was not necessary since all the activity was removed in the load and wash steps. The resin was finally removed from the column and transferred to a serum vial. The activity retained on the column was then determined by γ-ray spectrometry.

7.3.5 Results

The second experiment was performed to determine if Ce forms any anionic complexes with sulphuric acid that could cause it not to be retained on the cation exchange resin. If Ce formed any anionic species it would be retained on an anion exchange column. As can be seen from the elution curve in Fig. 7.3, the ^{139}Ce activity simply passed straight through the column during the load step, and was completely eluted during the wash step of the separation. One can therefore conclude that ^{139}Ce is exclusively retained as Ce^{4+} on AG MP-50 resin and the optimization of a production procedure would only need to be done to remove the ^{139}Ce from the column faster and with less eluent.

7.4 Separation of ^{139}Ce from a La_2O_3 target

7.4.1 Reagents and Apparatus

Only analytical grade reagents were used. Lanthanum oxide (99.98%), was obtained from Fluka, Switzerland. Only deionized water was used and was obtained from a Millipore Milli-Q Water System. The strong basic anion exchange macroporous resin, AG MP-1 (chloride form, 100-200 mesh particle size), was supplied by Bio-Rad Laboratories, Richmond, California. The anion exchange resin was converted to the nitrate form before use.

A polyethylene tube (10 mm i.d. and 70 mm long) fitted with a 70 μm frit at the bottom was used as an anion exchange column. The column was filled with slurry of AG MP-1 resin until the settled resin reached a mark indicating a volume of 5 mL. A 70 μm frit was placed on top of the resin in the column. A plunger made of a Teflon rod [10 mm diameter, 30 mm long, with a hole (1 mm bore) drilled through the length, fitted with an O-ring near the bottom and a luer-fitting at the top] was used to seal the column at the top. The plunger was pushed firmly onto the frit until the resin column was compacted to a volume of $\sim$ 5.0 mL. The resin was equilibrated with 6.0 M HNO_3 - 0.6 M $NaBrO_3$.

As before, high-resolution γ-ray spectrometric analysis, with a high purity germanium detector and multichannel analyzer, was used to check the yield and percentage efficiency of the experimental method.

7.4.2 Separation of ^{139}Ce from the La_2O_3 target material

The aluminium capsule, containing the La_2O_3 target, was cut open at one side and the target removed from it. The target was placed in a polyethylene bottle containing 125 mL of 4.0 M HNO_3. When the reaction had slowed down, 50 mL of 70% HNO_3 was added and the dissolution continued until the La_2O_3 was completely dissolved. After the dissolution of the La_2O_3, the solution was decanted into a beaker and heated to 100 °C. The bottle and capsule were rinsed with five 25 mL portions of 70% HNO_3 and these solutions were also added to the beaker. 25 mL of 10 M $NaBrO_3$ was added to the beaker and the solution was heated until its color turned dark brown and fumes of bromine were released.

The heat was turned off and the solution was allowed to cool for 10 minutes. The beaker was then put in a water bath at room temperature and stirred for 10 minutes. It was then placed in ice water and the solution was stirred for another ten minutes. After the solution in the beaker had cooled down to $\sim$ 20 °C, it was pumped through the resin column with a peristaltic pump at a flow rate of 5.0 mL/minute. La was eluted with 400 mL of 6.0 M HNO_3 - 0.7 M $NaBrO_3$ solution and the $NaBrO_3$ washed from the resin

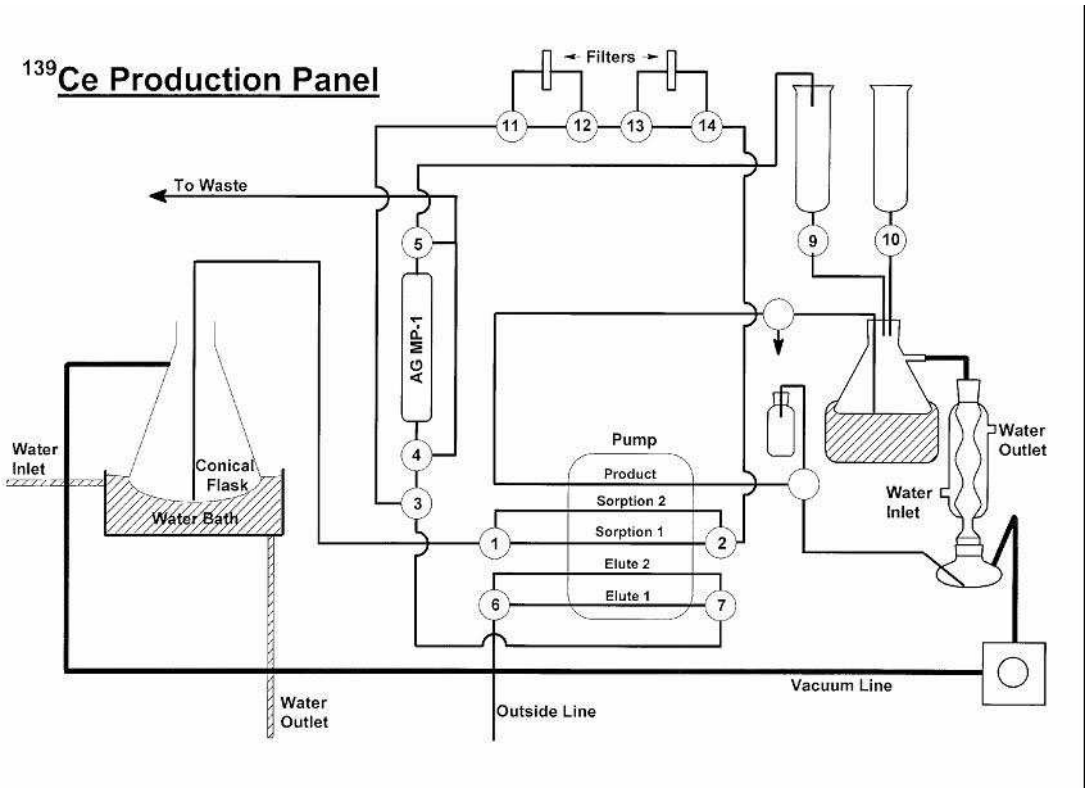

Figure 7.4: The design of a hot-cell production panel for the full scale separation of ^{139}Ce form Pr and La_2O_3 target materials. The schematic follows the standard design philosophy used at iThemba LABS for all ion exchange separation processes.

column with 25 mL of 6.0 M HNO_3. Finally, ^{139}Ce was eluted from the resin with 50 mL of 0.2 M HNO_3 containing 2 mL H_2SO_3. The eluate was collected in 5 mL fractions and the activity measured by γ-ray spectrometry.

7.4.3 Results

In this experiment, the method was changed so that the concentration of the BrO^{3-} was much higher than in the separation of ^{139}Ce from a Pr target. The recovery of ^{139}Ce was improved to 83.5%. The losses can in this case be attributed to the massive amounts of Br_2 released during the load step that totally saturated the column and allowed some of the ^{139}Ce to be carried through the column into the waste stream. A balance between the two concentrations of BrO^{3-} used in this work will have to be found and the size of the column will have to be enlarged to accommodate all the Br_2. This technique shows a lot of promise and, with further refinement, yields of up to 95% should be achievable. Figure 7.4 shows the design of a hot-cell production panel for the full scale separation.

7.5 Production of ^{140}Nd and ^{139}Pr

7.5.1 Introduction

The separation of the lanthanides is notoriously difficult and many processes have been used over the years with varied levels of success. In 1950, Fitch and Russel reported on the ion-exchange separation of lanthanides using complexing agents, as well as careful control over pH and ion concentration [75]. This type of technique is very important for the success of the current work. Over the next forty years, various authors reported on the separation of the lanthanides. Solvent extraction techniques were extensively used because they are suited to large-scale separations. The selectivities for the nearest neighbors of lanthanides by solvent extraction are generally very low because of their similar chemical properties, which in turn results in a large number of extraction stages to obtain the desired high purities. Another difficulty of solvent extraction is the fact that without expensive centrifuge systems, it is very awkward to implement in the hot-cell separation of very radioactive materials. This method is simply not practical for the separation of short-lived radionuclides.

The addition of water-soluble chelating agents such as ethylenediaminetetraacetic acid (EDTA) and diethylenetriaminepentaacetic acid (DTPA) to an aqueous phase was proved to be very effective in enhancing the selectivities in the solvent extraction of lanthanides in both equilibrium and non-equilibrium conditions. Matsuyama *et al.* [77] showed a number of successes using DTPA as chelating agent for the separation of some of the lanthanides.

In the literature, a number of interesting, yet impractical, techniques have been reported for lanthanide separations in recent years. In 2000 Uda *et al.* [78] reported in Science on a process for the enhanced separation of the lanthanides. The process used a combination of selective reduction and vacuum distillation of halides of some of the lanthanides. Kondo and Kamio [79] described the mutual separation of lanthanides by using a column packed with microcapsules containing an acidic organophosphorus compound as an extractant. They found they could achieve small scale separations of better than 95%. Microcapsule technology is unfortunately still in its infancy and therefore not very useful for the current work, but could well change the way radioisotopes are separated in the future. In 2003 Hubicka and Kolodynska used gel-based anion exchangers [80] and DCTA as complexing agent and showed an unusual order of elution, but could not do much better than previous attempts at this separation.

Over the last fifteen years, α-hydroxyisobuteric acid (α-HIB) has consistently proven itself as a complexing agent that has the potential to allow effective separation of the lanthanides in quantities much greater than the trace amounts separated for analytical purposes. To

this end, specifically, cation exchange chromatography using α-HIB is widely considered to be the most effective method of separating lanthanides. Reversed-phase resins that are Ln-specific and anion exchange techniques have in recent years been used to separate lanthanides as well and gave separation resolutions that are comparable to α-HIB and cation exchange chromatography. Reversed-phase resins can be either gravity fed or used with a vacuum box. This makes it difficult to use in a hot-cell environment for the separation of short-lived radionuclides, since practicality and speed are of the essence. Ion exchange resins, on the other hand, are well suited for this purpose and also lend themselves well to the application of High Performance Liquid Chromatography (HPLC) in separations, since they remain stable at high pressure. A very important paper was published by Schwantes *et al.* [81] in 2006. They showed that by adjusting both initial pH and (α-HIB) concentration, a much better separation than before can be achieved. They also hinted at the separation of large amounts of target material from radioactive tracers. This paper is currently the basis for the present investigations into the separation of Nd and Pr at iThemba LABS.

For the present study, cation exchange is proposed, where the two elements of interest are first loaded onto a column and then eluted, using an HPLC gradient pump to change the complexing agent concentration. Because the bulk of the target material is rather large, a normal HPLC column would be saturated and probably rendered useless if employed for the separation. Therefore, the columns used in this study were based on the type of ion exchange column routinely used for separation of radioisotopes at iThemba LABS.

Gradient elution of the elements with α-HIB is effective since it manipulates the formation of complexes of the lanthanides (Pr + Nd) by changing the concentration gradually. The element which forms the more stable complex will react just a little faster with the α-HIB, and will begin to be eluted, while the other element is still retained on the column a little bit longer. When the concentration is high enough, both bands of the two elements start moving through the column.

7.5.2 Experiment 1: Separation of Nd from Pr

Columns

An initial separation used two parallel columns according to the proposal of Schwantes *et al.* [81]. Two polyethylene tubes (10 mm i.d. and 70 mm long) fitted with 70 μm frits at the bottom were used as columns. The columns were filled with slurry of AG MP-50 resin until the settled resin reached a mark indicating a volume of 5 mL. 70 μm frits were placed on top of the resin in the columns. Plungers made of Teflon rod [10 mm diameter, 30 mm long, with a hole (1 mm bore) drilled through the length, fitted with an O-ring

near the bottom and a luer-fitting at the top] was used to seal the columns at the top. The plungers were pushed firmly onto the frits until the resin columns were compacted to a volume of $\sim$ 5.0 mL. The resin was equilibrated with 25 mL 0.1 M HNO_3.

Load Solution

Quantities of 81.1 mg Pr_6O_{11} and 24.5 mg Nd_2O_3 were dissolved in 5 mL of 1 M HNO_3. The solution was evaporated to dryness and reconstituted in 50 mL of 0.1 M HNO_3. The pre-equilibrated columns (25 mL of 0.1 M HNO_3) were loaded with this solution at 10 mL/min and washed with 50 mL of 0.1 M HNO_3. A 1 mL stock sample was retained as a control. Load and wash samples were taken at half stages of loading and washing, respectively, to test for breakthrough during these steps. Inductively coupled plasma (ICP) analysis of the wash and load samples showed no breakthrough of Nd or Pr from the column.

Elution

The method for the elution was taken from the Dionex techical note on the separation of lanthanide metals [82]. A gradient pump was used with solutions: A = Water and B = 0.4 M α-HIB at pH 4.3. A linear gradient of A : B = 30% : 70% was applied to the columns for 30 minutes at 2.5mL/min. Samples were collected every 3 minutes (9 mL sample). A total of 14 samples were collected.

Analysis

Samples were analyzed by ICP using direct measurement of the emission lines, 414.311 nm and 401.225 nm, for Pr and Nd respectively.

Results

In Fig. 7.5, the elution curves for the Nd and Pr elutions from AG MP-50, using the gradient elution method and two parallel columns, are plotted. One can see that the Nd peak has been shifted to the right, but still fall within the Pr peak. The original suggestion from Schwantes *et al.* [81] was to use three parallel columns. This was found to be impractical however, since a constant flow rate through three columns was very difficult to maintain using an HPLC pump. The second detrimental factor is the 30 min time limit needed for separation of ^{139}Nd from the Pr target material.

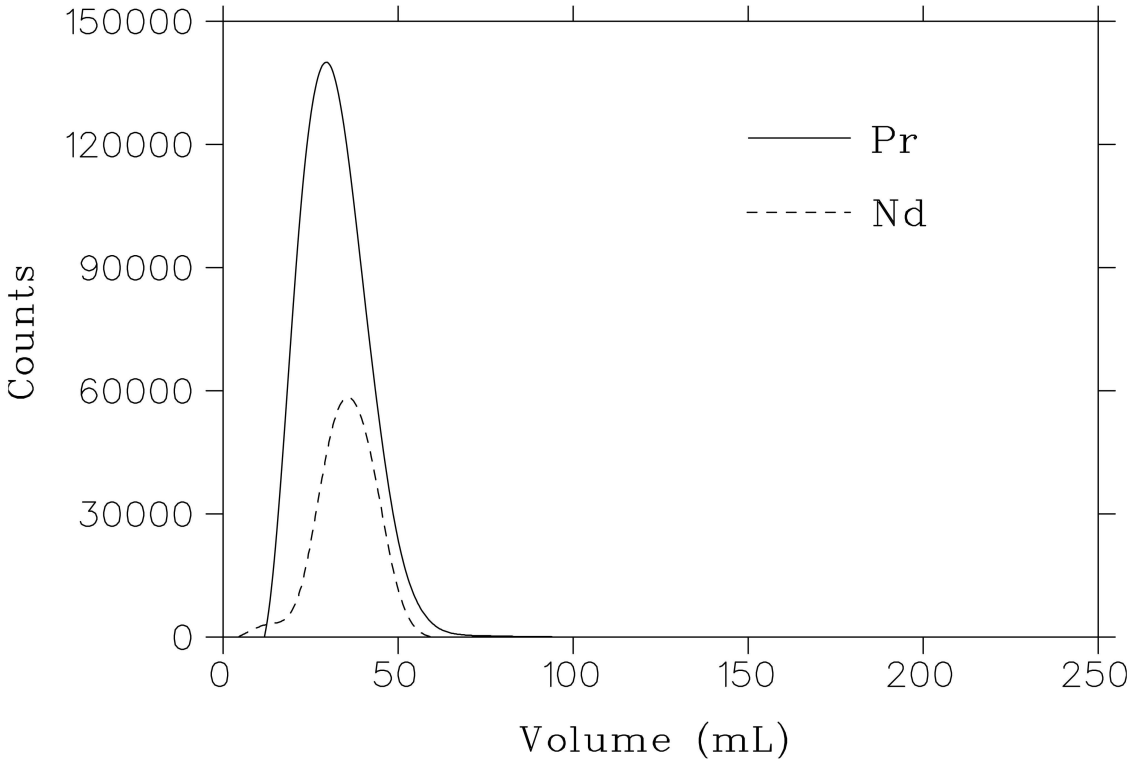

Figure 7.5: Elution curves of Pr and Nd from the AG MP-50 dual resin column during the separation. One can see that the Nd peak has shifted to the right as a result of the gradient elution.

7.5.3 Experiment 2: Separation of Nd from Pr

Columns

For the second experiment the column was changed to a longer polyurethane tube (5 mm i.d. and 200 mm long) fitted with 70 μm frits at both ends. The column was filled with slurry of AG MP-50 resin until the settled resin fully occupied the tube. Plungers made of Teflon rod [5 mm diameter, 30 mm long, with a hole (1 mm bore) drilled through the length, fitted with an O-ring near the bottom and a luer-fitting at the top] was used to seal the tube at both ends. The plungers were pushed firmly into the tube to ensure a good seal. The purpose of this experiment was to check if any separation occurred if the highest concentration of α-HIB (0.4 M)was used for elution using a normal peristaltic pump. The resin was equilibrated with 50 mL of 0.1 M HNO_3.

Load Solution

Quantities of 7.5 mg Pr_6O_{11} and 2.5 mg Nd_2O_3 were dissolved in 5 mL of 1 M HNO_3. The solution was evaporated to dryness and reconstituted in 50 mL of 0.1 M HNO_3. The pre-equilibrated column (50 mL of 0.1 M HNO_3) was loaded with this solution at 2 mL/min and washed with 50 mL of 0.1M HNO_3. A 1 mL stock sample was retained as a control.

Load and wash samples were taken at half stages of loading and washing respectively to test for breakthrough during these steps. Inductively coupled plasma (ICP) analysis of the wash and load samples showed no breakthrough of Nd or Pr from the column.

Elution

The column was eluted at $\sim$ 2.5 mL/min with 0.4 M of α-HIB at pH 4.3. Samples were collected every minute (2.5 mL samples). A total of 50 samples were collected. The flow rate slowed from 2.5 to 2.1 mL/min as column compression occurred.

Analysis

Samples were analyzed by ICP using direct measurement of the emission lines, 414.311 nm and 401.225 nm, for Pr and Nd respectively.

Results

In this experiment we tried to achieve separation of Pr and Nd by using a single, longer column and one concentration of α-HIB only. As can be seen in Fig. 7.6, no separation whatsoever was achieved during this specific run. It seems that the lower concentration of α-HIB causes the separation and the higher concentration, as the gradient nears its end, moves both bands through the column. The next step was to test the new column with a gradient elution.

7.5.4 Experiment 3: Separation of Nd from Pr

Columns

For the third experiment the column was again the longer polyurethane tube (5 mm i.d. and 200 mm long) fitted with 70 μm frits at both ends. The column was filled with slurry of AG MP-50 resin until the settled resin fully occupied the tube. Plungers made of Teflon rod [5 mm diameter, 30 mm long, with a hole (1 mm bore) drilled through the length, fitted with an O-ring near the bottom and a luer-fitting at the top] was used to seal the tube at both ends. The plungers were pushed firmly into the tube to ensure a good seal. In this experiment, the gradient elution method was applied to see if separation could be achieved with the longer column. The resin was equilibrated with 50 mL 0.1 M HNO_3.

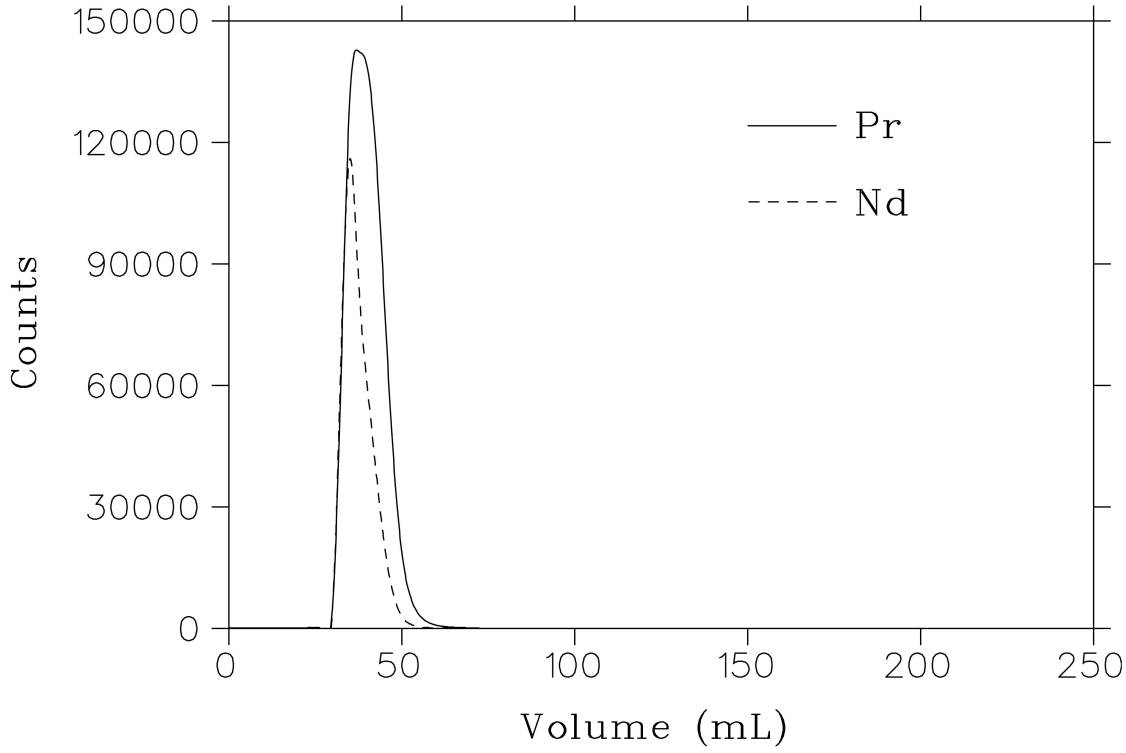

Figure 7.6: Elution curves of Pr and Nd from the AG MP-50 polyurethane tube column during the separation. One can see that the Nd peak has not shifted at all and starts exactly where the Pr curve starts.

Load Solution

Quantities of 7.5 mg Pr_6O_{11} and 2.5 mg Nd_2O_3 were dissolved in 5 mL 1 M of HNO_3. The solution was evaporated to dryness and reconstituted in 50 mL of 0.1 M HNO_3. The pre-equilibrated column (50 mL of 0.1 M HNO_3) was loaded with this solution at 2 mL/min and washed with 50 mL of 0.1 M HNO_3. A 1 mL stock sample was retained as a control. Load and wash samples were taken at half stages of loading and washing, respectively, to test for breakthrough during these steps. Inductively coupled plasma (ICP) analysis of the wash and load samples showed no breakthrough of Nd or Pr from the column.

Elution

The method for the elution was taken from the Dionex technical note on the separation of lanthanide metals [82]. A gradient pump was used with solutions: A = Water and B = 0.4 M α-HIB at pH 4.3. The column was first washed with A : B = 86% : 14% for 10 minutes at 3.0 mL/min. A linear gradient of A : B = 30% : 70% was then applied to the column for 60 minutes at 3.0 mL/min. Samples were collected every 1.5 minutes (4.5 mL samples). A total of 36 samples were collected.

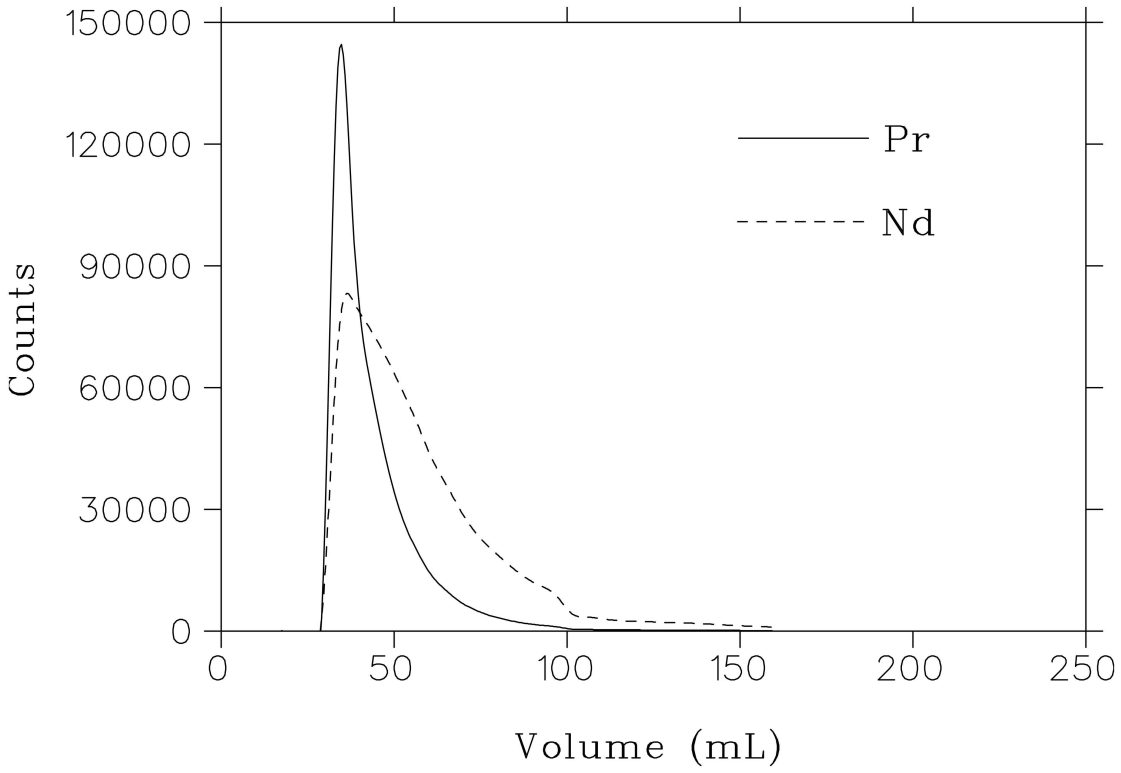

Figure 7.7: Elution curves of Pr and Nd from the AG MP-50 polyurethane tube column during the separation. One can see that the Nd peak has shifted to the right as a result of the gradient elution and separation of the two elements is starting to occur.

Analysis

Samples were analyzed by ICP using direct measurement of the emission lines, 414.311 nm and 401.225 nm, for Pr and Nd respectively.

Results

Figure 7.7 shows a marked improvement in separation with a part of the Nd elution curve already falling outside the Pr elution curve. This is a very promising result, since all the separations in the literature involving ion exchange has used very small samples. This is one of the few times separation of larger quantities of the two closest lanthanides have been attempted. Further suggested refinements are discussed in the next chapter.

Chapter 8

Conclusion

8.1 Radionuclide Production

This study set out to investigate the production of ^{139}Pr and ^{139}Ce in proton-induced reactions on different target materials. Along the way, it pulled together the chemistry of the different elements involved as well as the physics of proton-induced reactions on the relevant target materials. With a proton energy of 66 MeV, a significant number of reaction channels are open, thus reaction products of several elemental species will be formed. As a result, it is necessary to also know the properties and chemistry of all the impurities that are formed in these complex reactions to ensure that the radionuclide of interest is isolated as a chemically and radionuclidically pure product.

8.2 Nuclear Data Measurement

The nuclear data measurements on the Pr, La and Ce target materials have filled a gap in the worldwide knowledge of nuclear data and the work on Pr targets has been taken up in the EXFOR nuclear database under the entry number D0357. The data from the bombardment of La_2O_3 and CeO will be submitted to the Nuclear Data Section (NDS) of the IAEA for inclusion in the EXFOR database in due course. The work has proven that natural Pr can be effectively used as target material for both the productions of ^{139}Pr and ^{139}Ce. The nuclear data measurement and analysis has shown that ^{139}Pr of extremely high purity can be achieved if the separation of the isotope is performed within optimum time slots after bombardment of the target.

For the production of ^{139}Ce, it was shown that even though the contribution from the La_2O_3 target to the overall production during bombardment of the tandem configuration is relatively small, it can still prove useful on smaller cyclotrons where the high energy protons needed for the reaction on Pr is not available. Practical quantities of ^{139}Ce can

be produced with lower energy protons and La_2O_3 has also proven to be a friendly target material that behaves well under bombardment conditions and during chemistry.

The present investigation utilized the techniques of measuring excitation functions and integrating them to find the predicted thick target yields in the case of Pr target material. The reverse scenario was used in the case of La_2O_3, where the thick target yields were measured first and the excitation functions were derived from that through differentiation of the resultant yield curves. Some interesting statistical techniques had to be employed to deal with experimental discrepancies and proved to be useful tools is these studies.

The first and second objectives as stated at the top of page 3 was therefore fulfilled.

8.3 Separations

The separation of ^{139}Ce has been tested and optimized to a point where a yield of nominally 85% can be achieved relatively easily from either Pr or La_2O_3 target material. It is hoped that further refinement should push this value up. (A recovery of 95% or better is seen as the goal for further development of the method). It is foreseen that ^{139}Ce can become a very important calibration source for SPECT imaging if it is made available in commercially viable quantities. Future plans for this nuclide is to produce test sources and determine the effectiveness of these sources in conjunction with the equipment suppliers and the local nuclear medicine community.

From a nuclear data point of view, similar yields of radiochemically pure ^{139}Pr can be obtained from the proton bombardment of natural Pr and CeO_2 targets. This study has once again showed that the separation of the three-valent lanthanides is notoriously difficult and that the Nd / Pr separation, in particular, is possibly the most difficult. This said, the results of the separations are promising and it does seem that with further refinement, an effective separation of the two elements can be achieved. One may perhaps conclude that the CeO_2 + p route is the superior one if the main aim is to produce ^{139}Pr only, because the chemical separation is simpler. On the other hand, the Pr + p route gives the possibility to produce useful quantities of ^{139}Pr and ^{140}Nd simultaneously. Although the main focus of this part of the investigation was the radionuclide ^{139}Pr, it is perhaps appropriate to speculate that ^{140}Nd may in future be of far greater importance to the medical community. As such, further work on the separation of Nd from Pr should perhaps focus more on ^{140}Nd production. This is important for two other reasons, namely (1) there is no viable alternative production method for ^{140}Nd (in contrast to ^{139}Pr) and (2) the time constraints of the separation procedure are less stringent for the longer-lived ^{140}Nd.

The rapid separation of the lanthanides is very important, not only for industry, but more importantly for the separation of radionuclides. The lanthanides and the actinides have similar properties and are major contaminants in the nuclear industry where they are a byproduct of the nuclear reactor operations. These methods can thefore also find wide use in waste treatment.

Further work to separate the Nd and Pr will endeavour to optimize the length of columns, the type of column and investigations into various eluants used for the separation. As already alluded to above, an efficient recovery of ^{140}Nd may turn out to be more important than a rapid recovery of ^{139}Pr.

The third objective of this study, to find and optimize the chemical separation of the radionuclides of interest, was fulfilled during this part of the work.

Appendix A

Important Quantities

It is interesting that the radioactivity decay laws as well as the concept of the production cross section can be obtained by relating simple quantities. Although this approach may lack mathematical rigor, it provides physical insight and can at times be a very useful "first approach" in solving problems. The first step is to determine which quantities are directly or inversely proportional to each other and to write down their relationship, up to the point where the inclusion of a proportionality constant will complete the equation. The second step is to provide appropriate boundary conditions. More often than not, the proportionality constant turns out to have physical significance.

A.1 Radioactive Decay

Let $N(t)$ denote the number of radioactive nuclei of a given species at a time t. If the radioactivity is in the form of an isolated source, $N(t)$ will be a monotonically decreasing function of t because it is decaying, thus its derivative will always be negative. The question to be asked is how many nuclei will decay in a small increment of time Δt? Let this quantity be denoted by $\Delta N(t)$.

Clearly, $\Delta N(t)$ will be directly proportional to Δt because more nuclei will decay in a larger time interval than in a smaller one. Also, the number of nuclei which will decay in a given time interval will depend on the number of nuclei available in the first place, thus $\Delta N(t)$ is directly proportional to $N(t)$. Thus

$$\Delta N(t) \propto N(t)\Delta t. \tag{A.1}$$

It is appropriate to introduce the proportionality constant in such a way that it is a positive quantity. Since the gradient of the function $N(t)$ is negative, one should write

$$\Delta N(t) = -\lambda N(t)\Delta t \tag{A.2}$$

Separation of variables and taking the limit where $\Delta t \rightarrow 0$ leads to

$$\frac{1}{N(t)} dN = -\lambda dt. \tag{A.3}$$

Next, both sides are integrated:

$$\begin{aligned} \int \frac{1}{N(t)} dN &= -\lambda \int dt + \text{constant}, \\ \therefore \ln N(t) &= -\lambda t + \text{constant}, \\ \therefore N(t) &= K e^{-\lambda t}, \end{aligned} \tag{A.4}$$

where K is a constant. The boundary condition to be applied is that at $t = 0$, $N(0) = N_0$, where N_0 is a quantity which can, in principle, be determined experimentally. Thus

$$N(t) = N_0 e^{-\lambda t}. \tag{A.5}$$

A.1.1 Activity

Activity is defined as the rate of radioactive decay:

$$A(t) = -\frac{dN(t)}{dt}. \tag{A.6}$$

Substituting $N(t)$ from equation A.5 yields

$$A(t) = -N_0 \frac{d}{dt}(e^{-\lambda t}) = \lambda N(t). \tag{A.7}$$

The proportionality contant λ is called the decay constant.

A.1.2 Half-life

The half-life, $T_{1/2}$, of a radionuclide is related to the decay constant. The half-life is defined by

$$N(T_{1/2}) = \frac{N_0}{2}. \tag{A.8}$$

Substituting into equation A.5 and some algebra yields:

$$T_{1/2} = \frac{\ln 2}{\lambda}. \tag{A.9}$$

A.2 Production Rates and Cross Sections

Consider a beam of accelerated charged particles of energy E traversing a thin target. The target can be considered "thin" when the energy loss ΔE is small compared to E, thus

$\Delta E \ll E$. Let the target thickness be denoted by Δx and the number of charged particles traversing the target per second by I_s. Let N_s be the number of target nuclei per unit area, which is obviously directly proportional to the target thickness. A diagramme depicting this is shown in Fig. A.1.

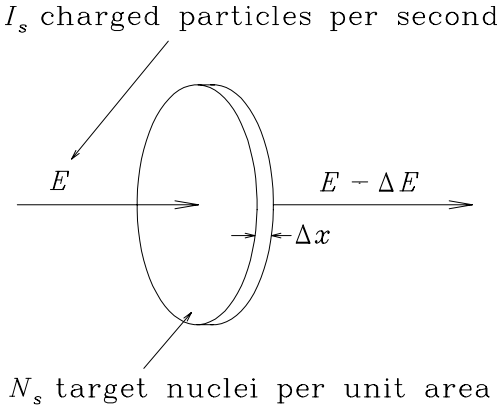

Figure A.1: Beam penetration through a thin target.

Let the number of residual nuclei of type p produced per second (*i.e.* the production rate) be denoted by R_p. Clearly, R_p is directly proportional to both I_s and N_s. Thus

$$R_p \propto N_s I_s. \tag{A.10}$$

Nothing else will, to first order, affect the production rate in the *thin target approximation* (*e.g.* the loss of charged particles from the beam due to non-elastic nuclear interactions will be insignificant), therefore only a proportionality constant is still required:

$$R_p = \sigma N_s I_s. \tag{A.11}$$

It turns out that σ can be associated with the probability for the formation of the residual nucleus of type p via a nuclear reaction. It is called the *cross section* for that particular nuclear process and is, in general, a function of the bombarding energy.

If the target described above is a typical foil in a stacked-foil experiment, it is usually appropriate to associate it with an energy midway between the incident and exit energies, thus the extracted cross section will be $\sigma(E - \Delta E/2)$.

The number of target nuclei per unit area is related to the target thickness by

$$N_0 = \frac{\rho \Delta x N_a}{A}, \tag{A.12}$$

where ρ and A are the density and atomic mass (in a.m.u.) of the target material, respectively, and N_a is Avogadro's number. Production rates curves of several Nd radionuclides produced in the proton irradiation of ^{141}Pr are shown in Fig. A.2. Note that, in general, $R = R(E)$. If two energy values are specified, an energy window is implied: $R(E_1, E_2) = R(E_1) - R(E_2)$.

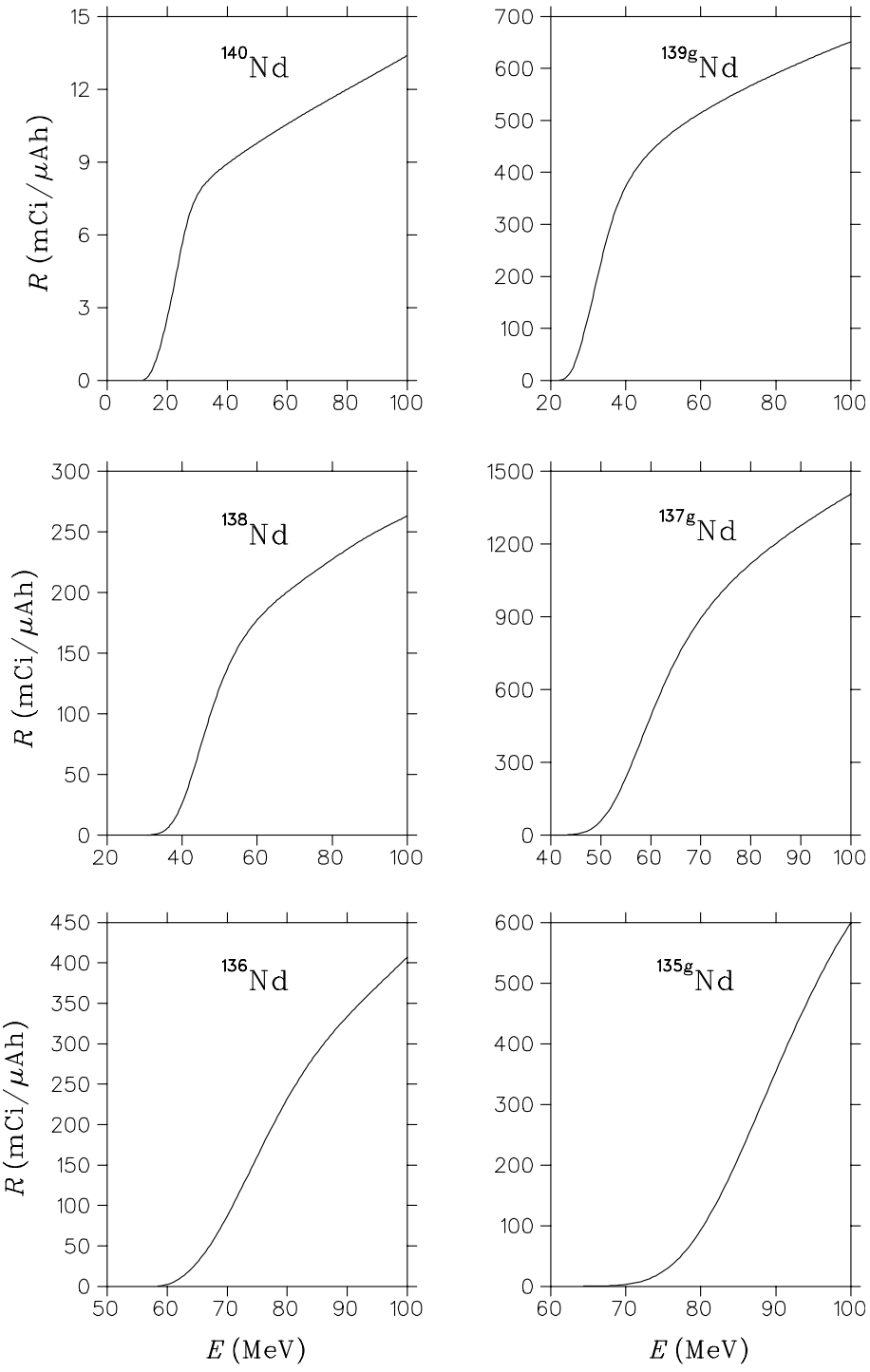

Figure A.2: Production rates of several Nd radionuclides produced in the proton bombardment of ^{141}Pr, plotted as a function of the proton energy.

Appendix B

Determination of Production Cross Sections from Activation Data

A comprehensive derivation of the equations used in this work to calculate the production cross sections of individual radionuclides from off-line γ-ray spectra measurements, are presented in a thesis by Buthelezi [83]. The following paragraphs present a summary of the main equations.

Beam intensity fluctuations can significantly affect measured results in cases where the radionuclides of interest have half-lives shorter than or similar to the bombardment time. It is often impossible to guarantee a constant beam intensity during the full duration of an experimental bombardment. A good approach is, therefore, to log the current integrator readings at sufficiently small times intervals. It has become standard practice at iThemba LABS to log the accumulated charge every 10 seconds.

Various times and other quantities are defined as follows:

$t = 0$:	Beginning of bombardment (BOB),
ΔT :	Time increment of current integrator scaler (10 s),
n :	Total number of 10 s increments during the bombardment period,
$t = T = n\Delta T$:	End of bombardment (EOB).

The end of each time interval is given by

$$h_i = i\Delta T \quad \text{for all} \quad 1 \leq i \leq n. \tag{B.1}$$

The expression for the cross section (in units of mb) is given by

$$\sigma = \frac{A_p}{\tau \epsilon_b \epsilon_e N_0 (1 \times 10^{-27}) \sum_{i=1}^{n} \Delta I_i \exp(-\lambda(T_m - h_i))}, \tag{B.2}$$

where A_p is the photo-peak area, τ is the live counting time in seconds, ϵ_b is the γ-line branching ratio, ϵ_e is the detector efficiency, N_0 is the total number of target nuclei per cm^2, ΔI_i is the total number of incident beam particles on the target in the i^{th} time increment, and T_m is the mean value of the counting interval.

Let T_c^{beg} and T_c^{end} denote the start and end times of the counting period. The mean value, where the actual activity equals the average activity over the entire counting period, is given by

$$T_m = -\frac{1}{\lambda} \ln \left[\frac{\exp(-\lambda(T_c^{end} - T_c^{beg}}{-\lambda(T_c^{end} - T_c^{beg})} \right]. \tag{B.3}$$

Equation B.2 can be simplified to the more usual "activation formula" if the beam current remains constant during the entire bombardment:

$$\sigma = \frac{A_p T}{\tau \epsilon_b \epsilon_e N_0 I_t (1 \times 10^{-27}) \exp[-\lambda(T_m - T)][1 - \exp(-\lambda T)]}, \tag{B.4}$$

where I_t is the total number of charged particles which traversed the target during the bombardment. This number is given by

$$I_t = \frac{Q \times 10^{-9}}{q_e m}, \tag{B.5}$$

where Q is the total integrated charge of the beam on target in units of nano-Coulomb (nC), $q_e = 1.602177 \times 10^{-19}$ C is the electron charge and m is the charge state of the accelerated particles. Obviously, for protons $m = 1$.

Appendix C

Growth and Decay Curves

Let $A_m(t)$ and $A_d(t)$ denote the mother and daughter activities, respectively, of a pair of appropriate radionuclides, such as ^{139m}Nd and ^{139}Pr. Let $t = 0$ be chosen such that $A_m(0) > 0$ and $A_d(0) = 0$, *i.e.* a time where one has isolated a certain quantity of the mother radionuclide but the feeding to the daughter radionuclide is still insignificant. The growth and decay curve is defined as

$$H(t) = \frac{A_d(t)}{A_m(0)}. \tag{C.1}$$

The time $t = 0$ may, for example, denote the time of the end of a chemical separation of the mother radionuclide from an irradiated target, or at least a fraction thereof, depending on the relative half-lives of the mother and daughter radionuclides. If a two-stage chemical separation procedure is to be followed in order to recover the daughter radionuclide, the second separation would typically be performed at or near the time where $H(t)$ reaches a maximum.

Let T_{end} denote a conveniently chosen "end time" for following the growth and decay of the daughter activity. Let N_{inc} be the number of small time increments of duration Δt. Then

$$\Delta t = \frac{T_{end}}{N_{inc}}. \tag{C.2}$$

Let i be an index such that $1 \leq i \leq N_{inc} + 1$ maps the time interval $0 \leq t \leq T_{max}$. Then

$$t_i = (i-1)\Delta t \quad \text{for all} \quad 1 \leq i \leq N_{inc} + 1 \tag{C.3}$$

defines a series of equispaced times covering the entire time period of interest.

Let $N_m(t)$ and $N_d(t)$ denote the number of mother and daughter nuclei present at time t, and let $\Delta N_d(i\Delta t)$ be the number of daughter nuclei formed in the time increment Δt

ending at $t = t_{i+1}$, for all $1 \leq i \leq N_{inc}$. Then

$$\begin{aligned}
\Delta N_d(i\Delta t) &= \epsilon_b[N_m(i\Delta t) - N_m([i+1]\Delta t)] \quad \text{for all} \quad 1 \leq i \leq N_{inc}, \\
&= \epsilon_b[N_m(0)e^{-\lambda_m i\Delta t} - N_m(0)e^{-\lambda_m(i+1)\Delta t}], \\
&= \epsilon_b N_m(0)e^{-\lambda_m i\Delta t}(1 - e^{-\lambda_m \Delta t}),
\end{aligned} \tag{C.4}$$

where λ_m is the decay constant of the mother radionuclide and ϵ_b is the branching ratio applicable to the formation of the daughter radionuclide. Note that Δt should be sufficiently small so that decay of the daughter radionuclide during this interval is negligible. Thus, by summing over all preceding intervals and incorporating daughter decay from all these intervals, one gets

$$\begin{aligned}
N_d(i\Delta t) &= \sum_{j=1}^{i} \Delta N_d(j\Delta t)e^{-\lambda_d(i-j)\Delta t}, \\
&= \epsilon_b N_m(0)(1 - e^{-\lambda_m \Delta t}) \sum_{j=1}^{i} e^{-\lambda_m j\Delta t}e^{-\lambda_d(i-j)\Delta t}, \\
&= \epsilon_b N_m(0)(1 - e^{-\lambda_m \Delta t}) \sum_{j=1}^{i} e^{-\lambda_m j\Delta t - \lambda_d(i-j)\Delta t}.
\end{aligned} \tag{C.5}$$

By multiplying both sides of the equal sign with $\lambda_m\lambda_d$ and rearranging variables, one can write

$$\lambda_m[\lambda_d N_d(i\Delta t)] = \lambda_d[\lambda_m N_m(0)]\epsilon_b(1 - e^{-\lambda_m \Delta t}) \sum_{j=1}^{i} e^{-\lambda_m j\Delta t - \lambda_d(i-j)\Delta t}, \tag{C.6}$$

from which follows that

$$\frac{A_d(i\Delta t)}{A_m(0)} = \frac{\lambda_d}{\lambda_m}\epsilon_b(1 - e^{-\lambda_m \Delta t}) \sum_{j=1}^{i} e^{-\lambda_m j\Delta t - \lambda_d(i-j)\Delta t}. \tag{C.7}$$

Equation C.7 can easily be computed numerically. Care must be taken to ensure that the time interval Δt is small enough for daughter decay of new growth during this interval to be insignificant. One can improve this approximation by allowing the new growth to decay from the centre of each time interval instead of from its end. Thus

$$H(i\Delta t) = \frac{A_d(i\Delta t)}{A_m(0)} = \frac{\lambda_d}{\lambda_m}\epsilon_b(1 - e^{-\lambda_m \Delta t}) \sum_{j=1}^{i} e^{-\lambda_m j\Delta t - \lambda_d(i-j+1/2)\Delta t}. \tag{C.8}$$

In practice, it is unimportant whether equation C.7 or equation C.8 is employed. With a value of $\Delta t = 1$ s, for example, both equations give the same results, for all practical purposes, for all the radionuclides relevant to the present study. Several relevant cases are shown in Fig. C.1.

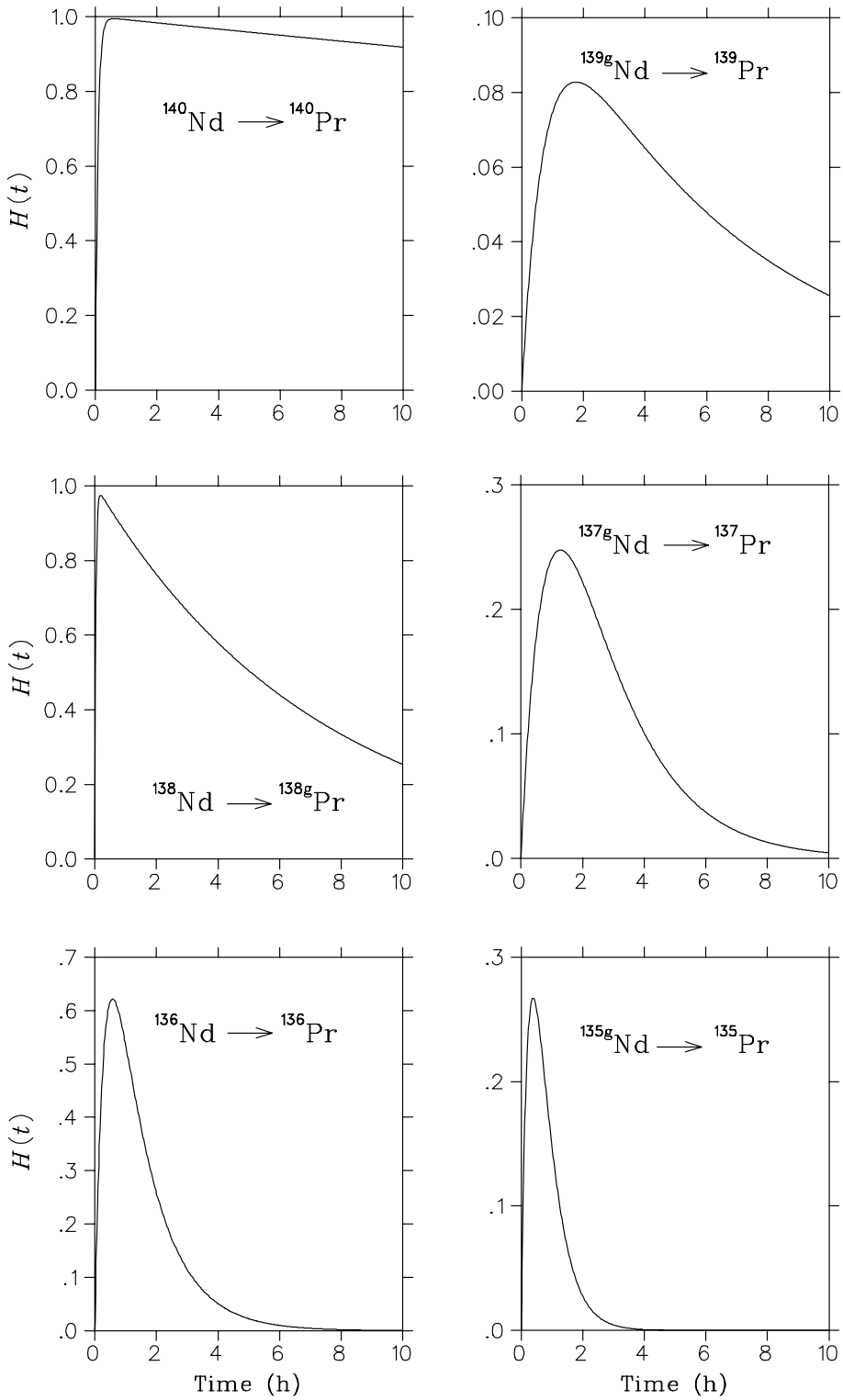

Figure C.1: Growth and decay curves for several Pr radionuclides formed from the decay of their respective Nd precursors. (See Fig. 4.4 for the important case ^{139m}Nd → ^{139}Pr.) Note that at time $t = 0$, only the parent radionuclide is present.

Appendix D

Final Activities of Pr Radionuclides Formed Via Nd Precursor Decay

The following paragraphs describe a model for the two-stage chemical separation procedure required to produce ^{139}Pr from a ^{141}Pr target. It can also be applied to all the other Pr radionuclides produced in order to calculate the radionuclidic purity of the final product.

Let R be the production rate (see Appendix A) of a mother Nd radionuclide in a target with an energy window $E_{in} \rightarrow E_{out}$. In general, $R = R(E_{in}, E_{out}) = R(E_{in}) - R(E_{out})$. In the following paragraphs, units of mCi/μAh are assumed for the production rate.

Let H be the fraction of $m \rightarrow d$ decay, as given by the growth and decay curve (see Appendix C). In general, $H = H(t)$.

Let I_0 be the beam current in units of μA.

Various times are defined as follows:

1. $t = 0$: Beginning of bombardment (BOB),
2. $t = T$: End of bombardment (EOB),
3. $t = t_1^{beg}$: Effective start of the first chemical separation,
4. $t = t_1^{end}$: Effective end of the first chemical separation,
5. $t = t_2^{beg}$: Effective start of the second chemical separation,
6. $t = t_2^{end}$: Effective end of the second chemical separation,
7. $t = t_{ref}$: Reference time,

where $0 < T < t_1^{beg} < t_1^{end} < t_2^{beg} < t_2^{end} < t_{ref}$.

Thus, there are several important periods of time (as introduced in Table 4.3):

1. T : Bombardment time,
2. $t_1^w = t_1^{beg} - T$: Waiting time 1,
3. $t_1^{chem} = t_1^{end} - t_1^{beg}$: Chemical separation 1,
4. $t_2^w = t_2^{beg} - t_1^{end}$: Waiting time 2,
5. $t_2^{chem} = t_2^{end} - t_2^{beg}$: Chemical separation 2,
6. $t_3^w = t_{ref} - t_2^{end}$: Waiting time 3.

Two more times are required by the model:

1. $t = t_1^{(j)}$: Effective end of the first chemical separation of a fraction (j) of the mother solution, where j is an index, $1 \leq j \leq J$ and $t_1^{beg} \leq t_1^{(j)} \leq t_1^{end}$;
2. $t = t_2^{(j)}$: Effective end of the second chemical separation of a fraction (k) of the relevant second solution, where k is an index, $1 \leq k \leq K$ and $t_2^{beg} \leq t_2^{(k)} \leq t_2^{end}$.

J and K are just sufficiently large integer numbers. This aspect of the model needs some careful explanation: First, the mother solution contains the entire target (now dissolved) as well as all the various radionuclides produced. Separating the Nd out from the mother solution does not happen instantaneously but takes place over a period of time. We modelled this separation by assuming that all the Nd from an incremental volume of the mother solution is effectively separated out at a specific time within this period of separation and that the entire process proceeds linearly. Thus, different completion times are associated with different fractions of the mother solution (moving, for example, through an ion-exchange column at a constant flow speed). Also, note that the "effective separation time" may be quite different from the total time of the chemical separation procedure. The first step in the chemistry may, for example, be the dissolution of the target. No separation takes place during this step, thus it falls outside the time interval t_1^{chem} above. Similar arguments apply to the second chemical separation.

In the following paragraphs, the relevant equations pertaining to each of the essential periods will be derived:

1. The bombardment period

Divide the bombardment period into N small time increments of length Δt. Let i be in index such that $0 \leq i\Delta t \leq T$ is mapped by $0 \leq i \leq N$.

The mother (m) activity at the end of bombardment is given by the sum of the individual contributions during each time increment:

$$A_m(T) = \sum_{i=1}^{N} \Delta A_m e^{-\lambda(T-i\Delta t)}, \tag{D.1}$$

where

$$\Delta A_m = RI_0 \Delta t. \tag{D.2}$$

I_0 is the beam current, which in this model is assumed to be constant.

$$\therefore A_m(T) = RI_0 \sum_{j=1}^{N} e^{-\lambda(T-j\Delta t)} \Delta t \tag{D.3}$$

In the limit where $\Delta \to 0$, the summation can be replaced by an integration:

$$\begin{aligned}
\therefore A_m(T) &= RI_0 \int_0^T e^{-\lambda_m(T-t)} dt \\
&= RI_0 e^{-\lambda_m T} \int_0^T e^{-\lambda_m t} dt \\
&= \frac{RI_0 e^{-\lambda_m T}}{\lambda_m} \; e^{-\lambda_m t}\Big|_0^T \\
&= \frac{RI_0 e^{-\lambda_m T}}{\lambda_m} \left[e^{\lambda_m T} - 1 \right] \\
&= \frac{RI_0}{\lambda_m} \left[1 - e^{-\lambda_m T} \right]
\end{aligned} \tag{D.4}$$

2. Waiting time 1

The m activity after EOB is given by

$$A_m(t) = \frac{RI_0}{\lambda_m} \left[1 - e^{-\lambda_m T} \right] e^{-\lambda_m (t-T)}, \tag{D.5}$$

where $t \geq T$.

3. Chemical separation 1

At the beginning of chemical separation 1, the activity of the mother radionuclide fractions is given by (using equation D.5)

$$\Delta A_m(t_1^{beg}) = \frac{A_m(t_1^{beg})}{J} = \frac{RI_0}{\lambda_m J} \left[1 - e^{-\lambda_m T} \right] e^{-\lambda_m (t_1^{beg} - T)}. \tag{D.6}$$

At this stage, all fractions have the same activity. At the effective end of the first chemical separation of fraction (j), its m activity is given by

$$\Delta A_m^{(j)} = \frac{RI_0}{\lambda_m J} \left[1 - e^{-\lambda_m T} \right] e^{-\lambda_m (t_1^{(j)} - T)}. \tag{D.7}$$

The associated daughter (d) activity of fraction (j) at the end of chemical separation 1 is given by

$$\Delta A_{1d}^{(j)} = \Delta A_m^{(j)} H(t_1^{end} - t_1^{(j)}). \tag{D.8}$$

The total d activity at the end of chemical separation 1 is obtained by summing:

$$\begin{aligned} A_{1d}(t_1^{end}) &= \sum_{j=1}^{J} \Delta A_{1d}^{(j)} \\ &= \frac{RI_0}{\lambda_m J}\left[1 - e^{-\lambda_m T}\right] \sum_{j=1}^{J} H(t_1^{end} - t_1^{(j)})\ e^{-\lambda_m (t_1^{(j)} - T)}. \end{aligned} \tag{D.9}$$

Note that for ^{139m}Nd$\rightarrow^{139}$Pr, the daughter activity given by equation D.9 only constitutes a very small fraction of the final daughter activity. The bulk of the final daughter activity comes from decay of the mother activity during waiting period 2.

4. Waiting time 2 and Chemical separation 2

It is possible to relate the daughter Pr activities, formed during waiting time 2 and up to the end of the second chemical separation, to the mother Nd activities in the final solution obtained at the end of the first chemical separation. Similar to the first chemical separation, one can divide the solution into K fractions of equal size:

$$\Delta A_m(t_1^{end}) = \frac{A_m(t_1^{end})}{K} = \frac{RI_0}{\lambda_m K}\ \left[1 - e^{-\lambda_m T}\right]\ e^{-\lambda_m (t_1^{end} - T)}. \tag{D.10}$$

The daughter (d) activity of fraction (k) at the effective end of chemical separation 2 is given by

$$\Delta A_{2d}^{(k)} = \Delta A_m(t_1^{end}) H(t_2^{(k)} - t_1^{end}). \tag{D.11}$$

The total d activity at the end of chemical separation 2 is obtained by summing:

$$\begin{aligned} A_{2d}(t_2^{end}) &= \sum_{k=1}^{K} \Delta A_{2d}^{(k)} \\ &= \frac{RI_0}{\lambda_m K}\left[1 - e^{-\lambda_m T}\right] e^{-\lambda_m (t_1^{end} - T)} \sum_{k=1}^{K} H(t_2^{(k)} - t_1^{end})\ e^{-\lambda_d (t_2^{end} - t_2^{(k)})}. \end{aligned} \tag{D.12}$$

Waiting time 3

The total daughter activity at the end of waiting time 3 is given by equations D.9 and D.12, with inclusion of the decay up to $t = t_{ref}$:

$$A_d = \left[A_{1d}(t_1^{end}) e^{-\lambda_d (t_{ref} - t_1^{end})} + A_{2d}(t_2^{end}) e^{-\lambda_d (t_{ref} - t_2^{end})}\right] \tag{D.13}$$

Bibliography

[1] M. Neves, A. Kling, A. Oliveira, "Radionuclides used for therapy and suggestion for new candidates", J. Radioanal. and Nucl. Chem. 266 (2005) 377.

[2] M. Burns, "New growth for diagnostic radiopharmaceuticals". In *Market Research in the Healthcare Field with Expertise in Medical Imaging and Radioisotopes*, Bio-Tech Systems Report, Las Vegas, Nevada, US, October 2006. Available from URL: http://www.biotechsystems.com/.

[3] L. Troncone, V. Rufini, P. Montemaggi, F. M. Danza, A. Lasorella, R. Mastrangelo, "The diagnostic and therapeutic utility of radioiodinated metaiodobenzylguanidine (MIBG).", European J. of Nuclear Medicine and Molecular Imaging 16 (1990) 325.

[4] S. M. Qaim, "New trends in nuclear data research and medical applications". In *Proc. Int. Conf. on Nuclear Data for Science and Technology*, (Eds. R. C. Haight, M. B. Chadwick, T. Kawano, P. Talou), held in Santa Fe, New Mexico, 26 Sept – 1 Oct 2004. American Institute of Physics Conf. Proc. vol. 769, 2005, p. 1600.

[5] D. W. Becker, "Herstellung, Radiochemie und Nuklearmedizinische Anwendung der Radioisotope des Praseodyms", PhD Thesis: Riprecht-Karls University, Heidelberg, Germany, 1999, unpublished.

[6] S. K. Zeisler, D. W. Becker, "A new method for PET imaging of tumours: human serum albumin labeled with the long-lived Nd-140/Pr-140 in vivo radionculide generator", Clinical Positron Imaging 2 (1999) 324.

[7] F. Rösch, J. Brockmann, N. A. Lebedev, S. M. Qaim, "Production and radiochemical separation of the Auger electron emitter ^{140}Nd", Acta Oncologica 39 (2000) 727.

[8] C. R. Hammond, "The Elements". In *CRC Handbook of Chemistry and Physics, 77th Edition*, (Ed. D. R. Lide), CRC Press, New York, 1997, p. **4**-7.

[9] S. K. Zeisler, D. W. Becker, "A pellet method for the measurement of excitation functions: Cross-sections for ^{140}Ce(p,2n)^{139}Pr and ^{140}Ce(p,3n)^{138m}Pr", Nucl. Instr. and Meth. B 160 (2000) 216.

[10] K. Hilgers, Yu. N. Shubin, H. H. Coenen, S. M. Qaim, "Experimental measurements and nuclear model calculations on the excitation functions of ^{nat}Ce(^{3}He,xn) and ^{141}Pr(p,xn) reactions with special reference to production of the therapeutic radionuclide ^{140}Nd", Radiochim. Acta 93 (2005) 553.

[11] H. Matsuyama, A. Azis, M. Fujita, M. Teramoto, "Analysis of extraction rate and selectivity of Pr/Nd separation by solvent extraction in the presence of diethylenetriaminepentaacetic acid in aqueous phase", J. of Chemical Engineering of Japan 28 (1995) 830, and references therein.

[12] J. M. Schwantes, R. S. Rundberg, W. A. Taylor, D. J. Vieira, "Rapid, high-purity, lanthanide separations using HPLC", J. of Alloys and Compounds 418 (2006) 189.

[13] A. I. Dityuk, A. Yu. Konobeyev, V. P. Lunev, Yu. N. Shubin, "New Advanced Version of the Computer Code ALICE-IPPE". International Nuclear Data Committee Report INDC(CCP)-410, 1998.

[14] C. Vermeulen, G. F. Steyn, F. M. Nortier, T. N. van der Walt, F. Szelecsényi, Z. Kovács, S. M. Qaim, Excitation functions and production rates of radionuclides produced in the proton bombardment of ^{nat}Pr and ^{nat}La. In *Proc. Int. Conf. on Nuclear Data for Science and Technology*, (Eds. R. C. Haight, M. B. Chadwick, T. Kawano, P. Talou), held in Santa Fe, New Mexico, 26 Sept – 1 Oct 2004. American Institute of Physics Conf. Proc. vol. 769, 2005, p. 1650.

[15] G. F. Steyn, C. Vermeulen, F. M. Nortier, F. Szelecsényi, Z. Kovács, S. M. Qaim, "Production of no-carrier-added ^{139}Pr via precursor decay in the proton bombardment of ^{nat}Pr", Nucl. Instrum. and Meth. B 252 (2006) 149.

[16] H. du Raan, P. D. du Toit, A. van Aswegen, M. G. Lötter, C. P. Herbst, T. N. van der Walt, A. C. Otto, "Implementation of a Tc-99m and Ce-139 scanning line source for attenuation correction in SPECT using a dual opposing detector scintillation camera", Med. Phys. 27 (2000) 1523.

[17] C. Vermeulen, G. F. Steyn, F. M. Nortier, F. Szelecsényi, Z. Kovács, S. M. Qaim, "Production of ^{139}Ce by proton-induced reactions on ^{141}Pr and ^{nat}La", Nucl. Instrum. and Meth. B 252 (2007), doi:10.1016/j.nimb.12.145.

[18] T. N. van der Walt, C. Vermeulen, "The isolation of ^{139}Ce after production by a proton-induced nuclear reaction on praseodymium". In *Proc. 4th Conference and Workshop on Cyclotrons and Applications*, held in Cairo, Egypt, 17–21 February 2001. Atomic Energy Authority, Egypt (2001) 173.

[19] R. B. Firestone, L. P. Eckström, "WWW Table of Radioactive Isotopes", Version 2.1, January 2004. Available from URL: http://ie.lbl.gov/toi.

[20] K. Gul, A. Hermanne, M. G. Mustafa, F. M. Nortier, P. Obložinský, S. M. Qaim, B. Scholten, Y. Shubin, S. Takács, F. T. Tárkányi and Z. Zhuang, "Charged particle cross-section database for medical radioisotope production: diagnostic radioisotopes and monitor reactions", IAEA-TECDOC-1211, IAEA, Vienna, May 2001. Available from URL: http://www-nds.iaea.org/medical/. (last updated 2005).

[21] J. F. Janni, "Proton range-energy tables, 1 keV–10 GeV", At. Data Nucl. Data Tables 27 (1982) 150.

[22] H. H. Anderson, J. F. Ziegler, "Hydrogen stopping powers and ranges in all elements". In *The stopping and Ranges of Ions in Matter*, Vol. 3 (Ed. J. F. Ziegler), Pergamon, New York, 1977, p. 1.

[23] M. J. Berger, J. S. Coursey, M. A. Zucker, J. Chang, "Stopping-power and range tables for electrons, protons and helium Ions", Last update, August 2004. Available from URL: http://physics.nist.gov/Star.

[24] S. M. Qaim, "Nuclear data relevant to cyclotron produced short-lived medical radioisotopes", Radiochim. Acta 30 (1982) 147.

[25] F. Rösch, S. M. Qaim, G. Stöcklin, "Nuclear data relevant to the production of the positron emitting radioisotpe ^{86}Y via the ^{86}Sr(p,n)- and ^{nat}Rb(^{3}He,xn)-processes", Radiochim. Acta 61 (1993) 1.

[26] Z. Kormány, "A new method and apparatus for measuring the mean energy of cyclotron beams.", Nucl. Instr. and Meth. A 337 (1994) 258.

[27] Z. Kormány, Private communication (2006).

[28] N. M. Downie, R. W. Heath, "Basic Statistical Methods", Third edition, Harper, Singapore, 1970.

[29] J. T. Newsom, "More on Chi-square", In *Jason Newsom's Stats Notes*, College of Urban and Public Affairs, Portland State University, USA. Available online from URL: http://www.upa.pdx.edu/IOA/newsom/pa551/.

[30] F. Szelecsényi, G. F. Steyn, Z. Kovács, C. Vermeulen, N. P. van der Meulen, S. G. Dolley, T. N. van der Walt, K. Suzuki, K. Mukai, "Investigation of the ^{66}Zn(p,2pn)^{64}Cu and ^{68}Zn(p,x)^{64}Cu nuclear processes up to 100 MeV: Production of ^{64}Cu.", Nucl. Instr, Meth. B 240 (2005) 625.

[31] R. Fresca Fantoni, E. Gadioli, P. Guazzoni, P. Vergani, L. Zetta, P. L. Dellera, F. Tomasi, V. Campagna, G. Ciavola, C. Marchetta, "RERAME: A facility for investigating heavy ion reactions with activation techniques", Appl. Radiat. Isot. 45 (1994) 325.

[32] E. Gadioli, P. E. Hodgson, *Pre-equilibrium Nuclear Reactions*, Clarendon, Oxford, 1992.

[33] K. Okamoto (Ed.), "Proceedings of the IAEA Consultants' Meeting on Data Requirements for Medical Radioisotope Production", International Nuclear Data Committee (INDC) Report INDC(NDS)-195/GZ, IAEA Nuclear Data Section, Vienna, 1988, p. 115.

[34] M. Blann, "Recent progress and current status of preequilibrium reaction theories and computer code ALICE", Lawrence Livermore National Laboratory Reports, UCRL-97948, 1988 and UCRL-JC-109052, 1991.

[35] A. V. Ignatyuk, J. L. Weil, S. Raman, S. Kahane, "Density of discrete levels in ^{116}Sn", Phys. Rev. C 47 (1993) 1504.

[36] J. J. Griffin, "Statistical model of intermediate structure", Phys. Rev. Lett. 17 (1966) 478.

[37] M. Blann, "Hybrid model for pre-equilibrium decay in nuclear reactions", Phys. Rev. Lett. 27 (1971) 337.

[38] M. Blann, "Importance of nuclear density distribution on pre-equilibrium decay", Phys. Rev. Lett. 28 (1972) 757.

[39] A. Iwamoto, K. Harada, "Mechanism of cluster emission in nucleon-induced preequilibrium reactions", Phys. Rev. C 26 (1982) 1821.

[40] K. Sato, A. Iwamoto, H. Harada, "Pre-equilibrium emission of light composite particles in the framework of the exciton model", Phys. Rev. C 28 (1983) 1527.

[41] P. Oblozinský, I. Ribanský, "Emission rate of preformed α particles in preequilibrium decay", Phys. Lett. B 74 (1978) 6.

[42] A. I. Blokhin, A. V. Ignatyuk, A. B. Pashchenko, Yu. V. Sokolov, Yu. N. Shubin, "Analysis of threshold reaction excitation functions in frame of unified superfluid model", Comm. Acad. of Science of USSR 49 (1985) 962.

[43] J. J. Hogan, "Study of the ^{141}Pr(p,xn) reaction from 10–85 MeV", J. Inorg. Nucl. Chem. 33 (1971) 3627.

[44] TABLECURVE 2D, "Automated Curve Fitting and Equation Discovery", Jandel Scientific, San Rafael, California, 1996.

[45] J. Wing, J. R. Huizenga, "(p,n) Cross sections ov V^{51}, Cr^{52}, Cu^{63}, Cu^{65}, Ag^{107}, Ag^{109}, Cd^{111}, Cd^{114} and La^{139} from 5 to 10.5 MeV", Phys. Rev. 128 (1962) 280.

[46] A. Hohn, F. M. Nortier, B. Scholten, T. N. van der Walt, H. H. Coenen, S. M. Qaim, "Excitation functions of ^{125}Te(p,xn)-reactions from their respective thresholds up to 100 MeV with special reference to the production of ^{124}I", Appl. Radiat. Isot. 55 (2001) 149.

[47] Cerium, "A guide to its role in chemical technology", Molycorp Inc., Mountain Pass, California, 1995.

[48] H. Aspinal, "Chemistry of the f-block elements", Gordon and Breach Science Publishers, Amsterdam, 2001.

[49] H. N. McMurray, "Hydrothermal modification of electrocatalytic and corrosion properties in nanosize particles of ruthenium dioxide hydrate", J. Mater. Chem. 4 (1994) 1283.

[50] G. A. Molander, "Application of lanthanide reagents in organic synthesis", Chem. Rev. 92 (1992) 29.

[51] R. C. Vickery, "Chemistry of the Lanthanons", Academic Press, (1953).

[52] K. A. Gschneidner Jr., L. Eyring, G. R. Choppin and G. H. Lander, Handbook on the Physics and Chemistry of Rare Earths, Vol. 18, North-Holland, (1994)

[53] S. T. Aruna, S. Gosh, K. C. Patil "Combustion synthesis and properties of $Ce_{1-x}Pr_xO_{2-\delta}$ red ceramic pigments", Int. J. Inorg. Mater. 3 (2001) 387.

[54] Lanthanides, "A lanthanide lanthology", Part 1 A-L Molycorp Inc., Mountain Pass, California, 1997.

[55] T. Moeller, "Complexes of the Lanthanides". In *Inorganic Chemistry Series*, Vol. 7 (Ed. K. W. Bagnall), Butterworths , London, 1972, p. 275.

[56] L. R. Morss, "Thermochemical ptoperties of Yttrium, Lanthanum and the lanthanide elements and ions", Chem. Rev. 76 (1976) 827.

[57] S. Bernal, G. Blanco, J. J. Calvino, J. A. Perez Omil, J. M. Pintado, "Some major aspects of the chemical behaviour od rare earth oxides: An overview", J. Alloy. Compd. 408 (2006) 496.

[58] S. R. Trout, "Rare earth magnet industry in the usa: Current status and future trends" (Proc. Rare Earth Magnet Workshop), Rinton Press, Paramus, NJ (2002).

[59] D. C. Stewart, D. Kato, "Analysis of rare earth mixtures by a recording spectrophotometer", Anal. Chem. 30 (1958) 164.

[60] Lanthanides, "A lanthanide lanthology", Part 2 M-Z Molycorp Inc., Mountain Pass, California, 1997.

[61] R. A. Eppler, "Formation of Pr-doped zircon colors in prescence of halides", Ind. Eng. Chem. Prod. Res. Dev., 10 (1971) 352.

[62] P. Shirron, D. Wegel, M. DiPirro, S. Sheldon, "An adiabatic demagnetization refrigerator capable of continuous cooling at 10 mK and below", Nucl. Instrum. Meth. A, 559 (2006) 651.

[63] F. Helferrich, Ion Exchange, McGraw Hill, New York (1962).

[64] M. Chabani, A. Armane, A. Bensmaili, "Kinetic modelling of the adsorption of nitrates by ion exchange resin", Chem. Eng. J., 125 (2006) 111.

[65] N. Z. Misak, "Adsorption isotherms in ion exchange reactions. Further treatments and remarks on the application of the Langmuir isotherm", Colloid. Surface. A, 97 (1995) 129.

[66] S. Glasstone, "Textbook of Physical Chemistry", D. Van Nostrand Co, New York (1946) 298 and 534.

[67] R. P. W. Scott, "Principles and practice of chromatography", http://www.library4science.com/, (2003) 19.

[68] R. Harjula, J. Lehto, L. Brodkin, E. Tusa, "CsTreat highly efficient ion exchange media for the treatment of cesium-bearing waste waters, Low Level Waste (Proc. Int. Conf. Providence, RI, 1997), Electric Power Research Institute, Palo Alto, CA (1997).

[69] Bio Rad Instruction Manual, "AG 1, AG MP-1, and AG 2 Strong anion exchange resin", 2007

[70] Bio Rad Instruction Manual, "AG 50W, and AG MP50 Catnion exchange resin", 2007

[71] R. P. W. Scott, "Liquid chromatography", http://www.library4science.com/, (2003) 4.

[72] G. D. Mayer, T. N. van der Walt, R. G. Bömer, P. Andersen, "Separation of ^{139}Ce from lanthanum cyclotron targets using anion exchange chromatography with a bromic acid / nitric acid system", Radiochim. Acta 34 (1983) 207.

[73] D. MacDonald, “Carrier-free separation of praseodymium-144 from cerium-144 by anion exchange”, Anal. Chem. 33 (1961) 1807.

[74] T. N. Van der Walt, C. Vermeulen, “The isolation of ^{139}Ce after production by a proton-induced nuclear reaction on praseodymium”, Proceddings of the 4^th Conference and Workshop on Cyclotrons and Applications, (2001), Cairo, Egypt.

[75] F.T.Fitch, D.S.Russel, “The separation of the rare earths by ion-exchange procedures”, Can. J. Chemistry, 29 (1951) 363.

[76] T. Kaneko, ”Separation of Rare Earth Metals by Solvent Extraction.”, Bunri Gijyutsu 21 (1991) 327.

[77] H. Matsuyama, A. Azis, M. Fujita, M. Teramoto, ”Analysis of Exctraction Rate and Selectivity od Pr/Nd Separation by Solvent Extraction in the Presence of Diethylenetriaminepentaacetic Acid in Aqueous Phase.”, J. Chem. Eng. Jpn. 28 (1995) 830.

[78] T. Uda, K. T. Jacob, M. Hirasawa, ”Technique for Enhanced Rare Earth Separation.”, Science 289 (2000) 2326.

[79] K. Kondo, E. Kamio, ”Separation of rare earth metals with a polymeric microcapsule membrane.”, Desalination 144 (2002) 249.

[80] H. Hubicka, D. Kolodynska, ”Separation of Y(dcta)$^-$ complexes from Nd(dcta)$^-$ and Sm(dcta)$^-$ complexes on polyacrylate anion-exchangers.”, J. Serb. Chem. Soc., 68 (2003) 183.

[81] J. M. Schwantes, R. S. Rundberg, W. A. Taylor, D. J. Viera, “Rapid, high-purity, lanthanide separations using HPLC”, J.. Alloy. Compd., 418 (2006) 189.

[82] Dionex, “Ion chromatography of the lanthanide metals”, Dionex Technical Note, 1991.

[83] E. Z. Buthelezi, ”Near-target and other heavy residues in the interaction of ^{12}C and ^{16}O with ^{103}Rh”, PhD Thesis: University of Stellenbosch, Stellenbosch, South Africa, 2004, unpublished.